

UNIVERSITÀ DEGLI STUDI DI NAPOLI “FEDERICO II”
FACOLTÀ D'INGEGNERIA
DOTTORATO DI RICERCA IN INGEGNERIA
DEI MATERIALI E DELLA PRODUZIONE (XXIV CICLO)



Dipartimento di Ingegneria dei Materiali e della Produzione

SYNTHESIS, CHARACTERIZATION AND
APPLICATIONS OF METAL ORGANIC FRAMEWORKS
IN THE ENERGY INDUSTRY FIELD

Tutor:	Dottorando:
Ch.mo Prof. D. Caputo	Ing. Maria Imperatore
Coordinatore: Ch.mo Prof. G. Mensitieri	

INDEX

Chapter I

Metal Organic Frameworks (MOFs)

1.Introduction	7
2.Structure of MOFs	8
3.Dependency of the stability of PW complexes on the electronic structure	10
4.One dimensional paddle wheel structures	13
4.1 One dimensional complexes	
4.1.1 Equatorial bridged dimetal complexes	
4.1.2 Dimers of axially bridged dimetal complexes	
4.2 One-dimensional polymers	
4.2.1 Axial connection of paddle-wheel complexes	
4.2.2 Equatorial linkage of paddle-wheels	
5 Two-dimensional paddle-wheel structures	21
5.1 Two-dimensional macromolecules	
5.1.1 Double-bridged dimetal units – molecular loops.	
5.1.2 Triangular complexes.	
5.1.3 Square-shaped complexes.	
5.2 Two-dimensional paddle-wheel polymers	
5.2.1 Equatorial linkage of paddle-wheels	
5.2.2 Axial linkage of paddle-wheels.	
5.2.3 2-D polymers from double strained chains.	
6 Three-dimensional cage compounds and polymers	36
6.1. Metal–organic polyhedra (MOP)	
6.1.1. MOPs with two and three paddle-wheel SBUs.	
6.1.2. Tetrahedral MOPs.	
6.1.3. Octanuclear cages.	
6.1.4. MOPs composed of five Cu ₂ units.	
6.1.5. Octahedral MOPs.	
6.1.6. Cuboctahedral MOPs.	
6.1.7. Rhombicuboctahedral MOPs.	
6.1.8 Rhombihexahedral cages.	

6.1.9 Relation between the linker and the type of polyhedra.	
6.2 Three-dimensional metal–organic frameworks (MOFs) with ‘paddle-wheel’ secondary building units.	
6.2.1 Stability of 3D PW-MOFs towards acids, bases and water.	
6.2.2. 3-D MOFs by stacking of 2-D MOFs.	
6.2.3. Direct formation of 3-D MOFs.	
7. Summary	52

Chapter II

Metal Organic Frameworks: a class of versatile materials for different applications

1. Introduction	54
2.MOF-Based Separations	55
2.1 MOFs for Removal of Toxic and Environmentally Hazardous Gases	
2.2 MOFs for Membrane-Based Separations	
3.MOF Guest Catalysts	59
4.MOFs as Drug Delivery Systems	63
5.Electronic and Optical Applications	65
5.1. Electronic Applications of MOFs	
5.2 Optical Applications of MOFs	
6. Hydrogen storage in Metal Organic Frameworks	67
6.1 Excess versus total uptake	
6.2.Design principles for an optimal H ₂ adsorbent	
6.3 Methods for increasing the H ₂ adsorption enthalpy	
6.3.1 Exposed metal sites	
6.3.2 Catenation/interpenetration	
6.4 Spillover	
6.5 Metal Organic Frameworks exhibiting a high H ₂ uptake	
7. Methane Storage	84
8. Metal Organic Frameworks for Carbon Dioxide capture	86

Chapter III:

Purpose of this Defense

1. Introduction	90
2. Hydrogen: The resource of the future	90
2.1 The U.S. Department of Energy's "Grand Challenge"	
2.2 Hydrogen for automotive applications	
3. MOF in the field of CO ₂ capture	96
4. Solar cooling	99
4.1 Because the solar cooling	
4.2 Technologies for solar cooling	
5. Purpose of the defense	103

Chapter IV

Experimental Activity

1 Experimental details regarding Cu-BTC MOF	105
1.1 Synthesis	
1.2 Characterization of synthesis products	
2 Experimental details regarding Cu-TRZ MOF	108
2.1 Synthesis	
2.2 Characterization of synthesis products	
3 Experimental details regarding MIL-101 MOF	110
3.1 Synthesis	
3.2 Characterization of synthesis products	

V Chapter

Results and Discussions

1. Materials characterization.	113
1.1 Cu-BTC	
1.2 Cu-TRZ	
1.3 MIL-101	
2. Adsorption measurement	127

2.1 Carbon dioxide adsorption on Cu-BTC	
2.2 Water Vapor Adsorption on Cu-TRZ	
2.3 Hydrogen adsorption on Cu-BTC and MIL-101	
2.3.1 Hydrogen Adsorption in Static Volumetric Conditions	
2.3.2 Hydrogen Adsorption in Dynamic Conditions	

Chapter VI

Summary and final evaluations

1. Introduction	154
2. Carbon Dioxide adsorption	155
3. Water Vapor Adsorption	156
4. Hydrogen storage	157
5. Conclusions and perspectives	157

References	160
------------	-----

Chapter I

Metal Organic Frameworks (MOFs)

1. Introduction

For many years, microporous inorganic solids have played a strategically important role in various industrial fields (oil chemistry, catalysis, selective separations) due to their porosity, high thermal stability and specific surface areas. Over the last 20, the scientific research on porous materials led to remarkable improvements, which can be summarized into two fundamental stages:

- (1) development of inorganic compounds with porosities that are an order of magnitude higher than their microporous counterparts (e.g., mesostructured silicas and silicoaluminates);
- (2) development of microporous compounds with a hybrid inorganic-organic chemical structure with higher specific surface areas, as in the case of metal organic frameworks (MOFs).

In particular, the latter class of materials constitutes an important and innovative attainment in the field of materials technology: in fact, the performances of metal organic materials in several industrial applications were often higher than those of traditional microporous materials [1], and, moreover, their chemical and physical properties suggest the possibility to further extend such application fields.

In the literature, the first mention of MOFs dates to 1985 [2], when investigations of these materials were still considered a simple academic exercise. In contrast, the recent proliferation of scientific papers on this subject demonstrates that the study of metal organic structures represents one of the most lively research areas in materials science and technology.

MOFs are porous materials in which metal ions or small metallic nano-clusters are linked into one-, two- or three-dimensional structures by multi-functional organic linkers.

There is no significant difference between MOFs and classical inorganic porous solids in terms of the geometry of the crystals because, in both cases, 3D structures can be described by the use of secondary building units (SBUs), as already established for the structural analysis of zeolites.

In MOFs, SBUs are geometrically simple polyhedrons that represent groups of inorganic clusters or coordination spheres held together by multidentate organic compounds, such as carboxylates and/or pyridines [3].

2. Structure of MOFs

The research on metal–organic frameworks, also known as metal–organic porous coordination polymers, has received enormous attention in the last twenty years. The beauty of the structures and the synthetic intricacy make these materials highly attractive in the scientific community of inorganic and materials chemistry.

Moreover, their potential as functional materials is the reason why so many researchers in both industry and academia are studying the chemical and physical properties of this class of materials.

To date, MOFs have been used in catalysis [4], for gas storage and/or separation [5], as host materials for molecular compounds and/or nanoparticles [6], and were grown as thin films on surfaces [7]. Notably, in 2009, one entire issue of the Chemical Society Reviews was devoted to the synthesis and applications of porous coordination polymers, showing how rapidly an entirely new branch of solid state materials chemistry has evolved [8].

Three-dimensional metal–organic networks usually adopt ‘superstructures’ known from inorganic porous solids, such as zeolites, but MOFs are considered to be superior to these materials since the metal inside SBUs and the shape and length of the organic linker molecules can be freely varied, which not only allows different pore sizes, but also functionalization of the organic part.

Considering all structural types of MOFs reported to date, networks having a SBU with a so-called ‘paddle-wheel’ (PW) structure are among the most ubiquitous and best studied. This term is derived from the long-known dinuclear PW complexes of the type $[M_2(\mu-O_2C-R)_4]$ (with or without a metal-metal bond), where each metal has an octahedral coordination sphere and four bidentate ligands adopt the equatorial sites of the octahedral.

Almost all MOFs are synthesized by ‘traditional’ solvothermal synthesis, i.e. the treatment of simple metal salts (nitrates, halides etc.)

with the corresponding organic linkers at high temperatures and pressure for several days and at controlled pH. Hence, it is difficult to predict how the dimetal unit or a certain superstructure, respectively, can selectively form under these conditions.

Indeed, the demand for a rational control over the structure of MOFs is high, since the abovementioned synthesis protocols often consist of trial-and-error experiments.

Thus, the question whether MOFs can be synthesized ‘bottom-up’ from molecular PW complexes represents an attractive challenge in the synthesis field.

3. Dependency of the stability of PW complexes on the electronic structure

From 1965 to 2003, the number of compounds including M_2^{n+} units increased from 27 to more than 4000 [9].

The formation of multiple bonds requires the presence of d-orbitals (i.e. transition metals) in order to form bonding (σ , π , δ) and antibonding (σ^* , π^* , δ^*) orbitals.

The most usual oxidation states for the M_2^{n+} cores in paddle-wheel complexes are $n = 4, 5$, and 6 . As the values of n become greater than 6 , repulsion of the metal atoms seems to be evident. Oxidation numbers below $2+$ are not common. Rh_2^{4+} cores, belonging to the main representatives in metal-metal bond chemistry, are stabilized through the formation of single bonds between 2.35 and 2.45 Å of length.

According to the molecular orbital (MO) theory, eight of the 14 electrons are allocated in the bonding orbitals, whereas the six remaining electrons are distributed in the antibonding orbitals to give a $\sigma^2\pi^4\delta^2\delta^*\pi^*$ configuration.

Mo is the metal with the most multiply-bonded M_2^{n+} units. The Mo_2^{4+} unit has a $\sigma^2\pi^4\delta^2$ electron configuration and is stabilized by a quadruple bond. The average range of bond lengths is 2.06–2.12 Å.

Dirhenium (III) carboxylates are Re_2^{6+} -containing units which are stabilized through the formation of quadruple bonds resulting from the electronic configuration $\sigma^2\pi^4\delta^2$.

The majority of diruthenium compounds adopts the PW structure in which the most stable is Ru_2^{5+} . The stability of the Ru_2^{5+} tetracarboxylates compared to their Ru_2^{4+} analogues is due to half-filled antibonding orbitals δ^* and π^* which are very close in energy. The resulting electronic structure $\sigma^2\pi^4\delta^2(\delta^*\pi^*)^3$ leads to a bond order of 2.5. The average bond length of $[Ru_2(O_2CR)_4]^+$ complexes is 2.3 Å. Carboxylate-bearing Ru_2^{6+} cores seem to be not stable since there is no oxidation process in the cyclic voltammograms. The use of electron-rich bridging ligands and suitable axial linkers may stabilize the higher oxidation state Ru_2^{6+} . Chromium forms many PW compounds bearing Cr_2^{4+} units with multiple bonds. The Cr–Cr distances are influenced by axial ligation and vary in the range 1.83–2.7 Å. This variety of bond distances cannot be explained by the idea of Hartree–Fock calculations [10].

The size of the metal atoms plays an important role in the formation of the paddle-wheel unit since bridging ligands (RCO_2^- and stereoelectronically similar ones) favor shorter M–M distances.

Nevertheless, long M–M interactions in copper ($\sim 2.7 \text{ \AA}$) [11, 12] or zinc ($\sim 2.9 \text{ \AA}$) [13] PW complexes are common.

Table 1.1 shows the following trend for transition metals forming a dimetal core in PW arrangements: the higher the group number the smaller the bond order.

M	<i>n</i>	Electronic structure	Bond order	$d_{\text{M-M}} [\text{\AA}]$
Cr	4	$\sigma^2\pi^4\delta^2$	4 ($d < 2 \text{ \AA}$)	1.83–2.70
Mo	4	$\sigma^2\pi^4\delta^2$	4	~ 2.1
W	4	$\sigma^2\pi^4\delta^2$	4	~ 2.2
Tc	6	$\sigma^2\pi^4\delta^2$	4	~ 2.2
	5	$\sigma^2\pi^4\delta^2\delta^*$	3.5	~ 2.1
Re	6	$\sigma^2\pi^4\delta^2$	4	~ 2.2
Ru	5	$\sigma^2\pi^4\delta^2(\delta^*\pi^*)^3$	2.5	~ 2.3
Os	6	$\sigma^2\pi^4\delta^2(\delta^*\pi^*)^2$	3	~ 2.3
Rh	4	$\sigma^2\pi^4\delta^2\delta^{*2}\pi^{*4}$	1	~ 2.4
Pt	6	$\sigma^2\pi^4\delta^2\delta^{*2}\pi^{*4}$	1	~ 2.4

Table 1.1 List of dimetal units M_2^{n+} forming tetracarboxylates, their electronic structures, bond orders and average M–M distances[39].

4. One dimensional paddle wheel structures

4.1 One dimensional complexes

4.1.1 Equatorial bridged dimetal complexes

The connection of metal-metal multiply bonded paddle-wheel fragments to larger macromolecules has extensively been investigated by the group of F. A. Cotton. In 2001, Cotton et al. synthesized a series of novel dimolybdenum compounds based on the PW structure $[\text{Mo}_2(\text{OAc})_4]$, which served as starting materials for the synthesis of dimeric, dicarboxylate-bridged $[\text{Mo}_2]_2$ complexes [14].

The principle for the controlled assembly of complex networks is based on the substitution of at least one of four bidentate ligands in the equatorial plane of the Mo_2 centre. The most primitive reaction is the connection of two Mo_2 units by one linker.

In dependence of the geometry of the linker, e.g. terephthalate vs. orthophthalate, linear or bent molecules can be obtained.

4.1.2 Dimers of axially bridged dimetal complexes

Axial coordination sites of PW complexes (along the M–M bond) are usually either free or occupied by weakly bound solvent ligands. Thus, two PW units can also be connected by bifunctional linkers, according to Fig. 1.1.

The PW: linker ratio is important : when a ratio of 2:1 is used, dimeric complexes are obtained, whereas a 1:1 ratio leads to 1-D wires.

Already in 1992, Cotton's group prepared the tetranuclear compound $[\{\text{Ru}_2(\text{chp})_4\}_2(\text{pyz})][\text{BF}_4]_2$ (chp = anion of 6-chloro-2-hydroxypyridine, pyz = pyrazine) by substitution of an axial chloride ligand of $[\text{Ru}_2(\text{chp})_4\text{Cl}]$ with pyrazine [15]. In 1995, Cotton et al. isolated the osmium congener [16].

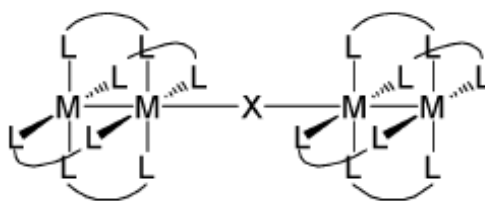


Fig. 1 General structure of dimers of M_2 paddle-wheel compounds containing axially bridging linkers X [14].

4.2 One-dimensional polymers

Extended linear metal-containing polymers have been investigated because of the potential electrical and optical properties present in their metals [17].

In order to generate 1-D chains, ligands with two functionalities or two 'active' spots are necessary. Linkers always connect two clusters and spread the polymerization in a linear way as shown in Fig. 1.2a.

The connections can have a character of strong covalent bonds as well as weak interactions. The connections can have a character of strong covalent bonds as well as weak interactions. From the morphology of the typical metal complex $[\text{M}_2(\text{O}_2\text{C-R})_4]$, it is clear that the unoccupied axial side provides a feasible place for the coordination of a linker.

The coordination of electron donating atoms to the free site along the M–M axis represents the first possibility of chain formation.

The second approach is the connection of two M–M units with equatorial linkers, typically dicarboxylates (Fig. 1.2b).

The polymeric chains are then formed along the equatorial coordination sites of the PWs.

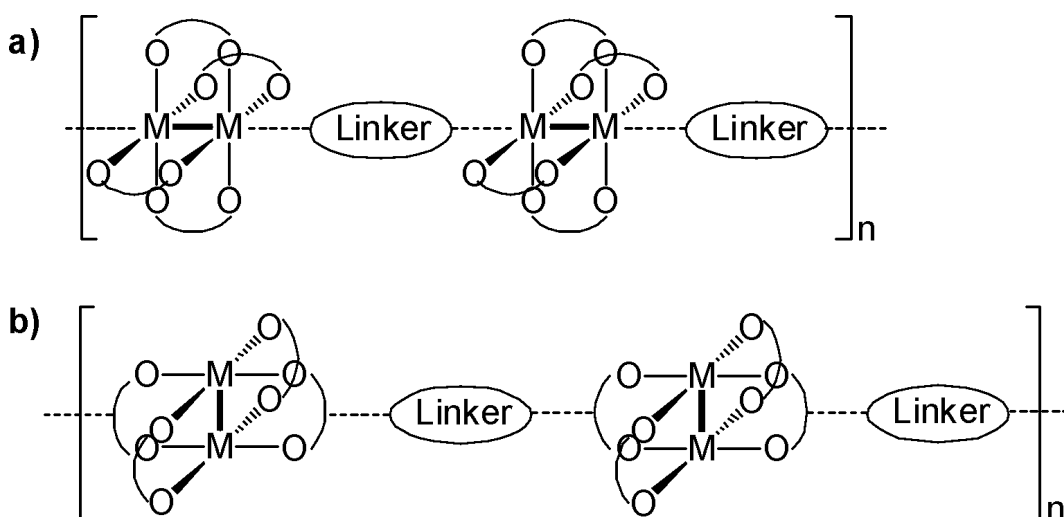


Fig. 1.2 Two general concepts of the formation of one-dimensional polymer chains [17].

Among the most often used axial linkers are molecules containing nitrogen atoms, such as 1,4-diazabicyclo[2.2.2]octane (dabco), pyrazine, 4,4'-bipyridine and their derivatives. Substituted pyrazine works as electron transfer between connected metal centers. Pyridyl derivatives embody several interesting advantages:

a) the double bond in the ligand brings conformational hardness;

b) the delocalised p-system can be applied as potential electron-interacting component;

c) the molecule can be easily extended by placing the spacer between coordination sites.

Ligands with two carboxylic groups belong to the most frequently used equatorial linkers for metal–organic polymers.

A wide spectrum of various carboxylates has been used to synthesize polymeric structures forming novel materials which demonstrate unique properties.

These organic molecules can be easily decorated with different functional groups or extended by insertion of spacers. The coordination chemistry of carboxylates to dimetal cores has been described by many authors and proven to be an excellent tool in the assembly process.

4.2.1 Axial connection of paddle-wheel complexes

The archetypical way to obtain one-dimensional polymers with PW units is the connection of dimetal carboxylates via the free axial coordination sites of the paddle-wheel with Lewis bases bearing two s-donor atoms (Fig. 1.2a).

In 1974, Soos et al. were the first to report on the crystal structure of a 1-D polymer, where binuclear copper acetate units $[\text{Cu}_2(\text{OAc})_4]$ are linked by the pyrazine ligand $\text{C}_4\text{H}_4\text{N}_2$ [18, 19]. The compound $[\text{Cu}_2(\text{OAc})_4(\text{C}_4\text{H}_4\text{N}_2)]_n$ was synthesized from a saturated aqueous

solution of $[\text{Cu}_2(\text{OAc})_4]$ and a solution of pyrazine. The two solutions were allowed to diffuse together in order to produce crystals of the linear chain.

In 1980, Cotton et al. determined the structure of the 1-D chain $[\text{Cr}_2(\text{OAc})_4(\text{pyz})]_\infty$ [20].

By mixing equimolar THF (TetraHydroFurane) solutions of $[\text{Cr}_2(\text{OAc})_4]$ and pyrazine, crystals of the linear chain were isolated. Subsequently, by this method, a lot of materials were synthesized.

In 1990, the groups of Kerby and Eichhorn synthesized the first 1-D zig-zag chains containing $[\text{Mo}_2(\text{OAc})_4]$ axially linked by the bidentate 1,2-bis(dimethylphosphino)ethane (dmpe) or tetramethylethylenediamine (tmeda) ligands by heating the PW complex in the solution of dmpe or tmeda, respectively [21].

In 1992, Perlepes and Christou reported the synthesis of polymeric zigzag chains consisting of alternating $[\text{Cu}_2(\text{OAc})_4]$ and $[\text{Cu}_2(\text{OAc})_2(2,2'\text{-bipy})_2]^{2+}$ linked by syn, anti bridging acetates [22]. The reaction of $[\text{Cu}_2(\text{OAc})_4(\text{H}_2\text{O})_2]$ with 2,2'-bipy in MeCN results in the precipitation of the polymeric compound.

In 1997, Christou et al. synthesised a polymeric 1-D zigzag chain consisting of alternating $[\text{Mo}_2(\text{O}_2\text{C}-\text{CHF}_2)_4(\text{bipy})_2]$ and $[\text{Mo}_2(\text{O}_2\text{C}-\text{CHF}_2)_4]$ units [23]. Treating a solution of equimolar amounts of $[\text{Mo}_2(\text{O}_2\text{C}-\text{CHF}_2)_4]$ and $[\text{Mo}_2(\text{O}_2\text{C}-\text{CHF}_2)_2(2,2'\text{-bipy})_2][\text{BF}_4]_2$ with two equiv. $[\text{NBun}_4][\text{O}_2\text{C}-\text{CHF}_2]$ results in the synthesis of polymeric zig-zag chains. The reaction product is depending on the molar ratio of the starting materials.

The synthesis of a one-dimensional coordination polymer formulated as $[\text{Bi}_2(\text{O}_2\text{C-CF}_3)_4] \cdot \text{C}_6\text{Me}_6$ is reported by Frank et al. in 1998 [24]. A solution of $[\text{Bi}(\text{O}_2\text{C-CF}_3)_3]$ and hexamethylbenzene is heated in a sealed glass tube to 100 °C in order to produce crystals after several weeks. The chain is generated due to the weak interaction between the metal complexes and the delocalised π -electrons of the hexamethylbenzene ring.

In 2001, Kühn et al. prepared organometallic oligomers of different length consisting either of dimolybdenum or dirhodium tetracarboxylates connected via 1,1'-bis(4-pyridylethynyl)ferrocene (bpef, Fig. 1.3) [25].

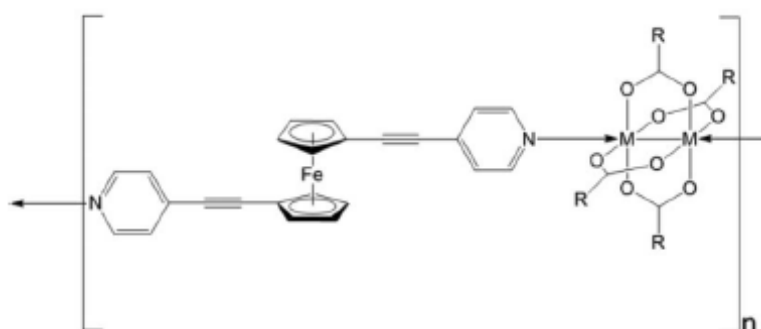


Fig.1.3 1-D oligomer consisting of alternating dirhodiumtetracarboxylate and bidentate linker 1,1'-bis(4-pyridylethynyl)ferrocene (bpef) [25].

By mixing the precursor compounds $[\text{Mo}_2(\text{OAc})_4]$, $[\text{Rh}_2(\text{OAc})_4]$ or $[\text{Rh}_2(\text{O}_2\text{C-CF}_3)_4]$ and bpef in solution at room temperature, organometallic oligomers of formula $[(\text{Rh}_2(\text{OAc})_4)^{n+1}(\text{bpef})_n]$ ($n=3$), $[(\text{Rh}_2(\text{O}_2\text{C-CF}_3)_4)_n(\text{bpef})^{n+1}]$ ($n=9-14$) and $[(\text{Mo}_2(\text{O}_2\text{CCF}_3)_4)(\text{bpef})_n]$ are generated. The number of repeating units and the terminal groups are determined by elemental analysis.

The same research group also synthesized two 1-D zig-zag chains with periodically repeating mono- and dinuclear metal complexes connected through bipyridine bridges [26].

In 2006, Hosseini et al. studied the influence of differently bent coordinating linkers on the morphology of 1- and 2-D networks [27]. The polymer chains were prepared by reacting $\text{Cu}(\text{OAc})_2 \cdot 2\text{H}_2\text{O}$ with each of the three ligands 1,2-,1,3-,1,4-phenylenediamine bearing two coordinating pyridine units at room temperature in a 1:1 molar ratio.

In the same year, Dietzel et al. synthesised infinite linear chains formed by zinc carboxylate PW units and dabco ligands by a solvothermal reaction of $\text{Zn}(\text{NO}_3)_2$, dabco and diphenic acid (H_2dpa) [28]. The chains are interconnected by the dpa unit via $\pi \cdots \pi$ stacking to form a layered 2-D coordination polymer of the formula $[\text{Zn}_2(\text{dpa})_2(\text{dabco})]_n$.

In 2007, Moncol et al. showed the linkage of SBUs to 1- and 2-D aggregates via N, N diethylnicotinamide (dena) [29]. The polymeric 1-D chain contains dicopper tetracarboxylate and the axial linker dena. The reaction of $[\text{Cu}(\text{O}_2\text{C}-\text{CH}_2\text{Cl})_2]$ with N,N-diethylnicotinamide in a 2:1 molar ratio yields the polymeric product. The zigzag chains weakly interact through $\text{N}-\text{H} \cdots \text{O}$, $\text{C}-\text{H} \cdots \text{O}$, and $\pi-\pi$ bridges, and stack into 2-D layers.

In 2008, Youngme et al. synthesized a polymeric chain consisting of zig-zag chains of mononuclear $[\text{Cu}(\text{O}_2\text{C}-\text{Et})_2(\text{H}_2\text{O})(\text{phen})]$ repeating units which are connecting $[\text{Cu}_2(\text{O}_2\text{C}-\text{Et})_4]$ PW units [30].

In 2009, Loeb and co-workers connected dicopper tetracarboxylates by [2]pseudorotaxane [31]. The [2]pseudorotaxane coordinates to the axial side of the dicopper core through a nitrogen atom of the bipyridine group in order to form the one-dimensional MORF (metal–organic rotaxane framework).

In 2010, Moncol et al. prepared a 1-D chain consisting of dinuclear PW units $[\text{Cu}_2(2\text{-O}_2\text{Nbz})_4(\text{nia})_2]$ ($2\text{-O}_2\text{Nbz}$ = 2-nitrobenzoate and nia = nicotinamide), which are linked with $\text{NH}\cdots\text{O}$ and $\text{CH}\cdots\text{O}$ hydrogen bonds [32].

4.2.2 Equatorial linkage of paddle-wheels

In 2008, Huang et al. solvothermally prepared three novel lanthanide PW 1-D chains of the type $[\text{Ln}(\text{bdc})_{1.5}(\text{def})]_\infty$ ($\text{Ln}=\text{La}, \text{Ce}, \text{Nd}$; bdc =1,4-benzenedicarboxylate; def =N,N-diethylformamide) [33]. The PW complexes of dilanthanide units are formed by two dimonodentate and two bridging bidentate bdc groups. In the same group, a series of 1- and 3-D polymeric structures containing lanthanides Ln ($\text{Ln} = \text{Nd}^{3+}, \text{Eu}^{3+}, \text{Tb}^{3+}, \text{Dy}^{3+}, \text{and Yb}^{3+}$) was synthesized [34]. The connection of in situ formed paddlewheel units using N-functionalised macrocyclic polyamine carboxylic acids such as 1,4,8,11-tetraazacyclotetradecane-1,4,8,11-tetraacetic acid (H_4teta) is leading to 1-D chains formulated as $[\text{Ln}(\text{H}_2\text{teta})]\text{NO}_3 \cdot 2\text{H}_2\text{O}$. The solvothermal reaction of $\text{Ln}(\text{NO}_3)_3 \cdot 6\text{H}_2\text{O}$ and H_4teta in deionised water leads to the formation of single crystals after slow cooling. Flexible macrocyclic rings act as

pillar linkers and extend the structure further into multidimensional 2-D and 3-D MOFs.

In 2009, Shi et al. described the formation of double-chained 1-D polymers of general formula $[M(\text{dpa})\text{CH}_3\text{OH}]_n$ from copper nitrate or nickel acetate and diphenic acid (dpaH) in methanol solution (Fig. 1.4) [35]. Through C-H $\cdots \pi$ interactions within the chains a 2-D polymeric architecture can be formed.

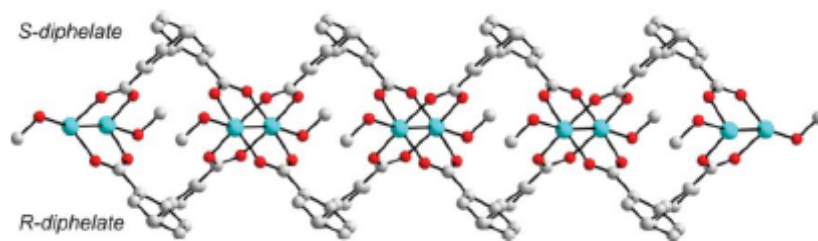


Fig.1.4 A segment of the double-chained 1-D polymer formulated as $[M(\text{dpa})\text{CH}_3\text{OH}]_n$ ($M = \text{Cu}, \text{Ni}$). (Cu: turquoise, O: red, C: grey) [35].

5. Two-dimensional paddle-wheel structures

The formation of two-dimensional macromolecules based on the bridging of paddle-wheel units with dicarboxylate (or other) linkers requires two easily replaceable cis-oriented equatorial ligands per metal. In dependence of the structure of the linker, macromolecules with different polygon shapes can be obtained.

5.1 Two-dimensional macromolecules

5.1.1 Double-bridged dimetal units – molecular loops.

In 1997, McCann's group prepared the first dimolybdenum loop by treating $[\text{Mo}_2(\text{CH}_3\text{CN})_8][\text{BF}_4]_4$ with succinic acid [36]. This electroinactive complex catalyses the ring-opening metathesis polymerisation of norbornene at room temperature.

5.1.2 Triangular complexes.

In 1999 [37], Cotton et al. had synthesized a triangular array assembling a 1-D tube in the solid state (Fig. 1.5).

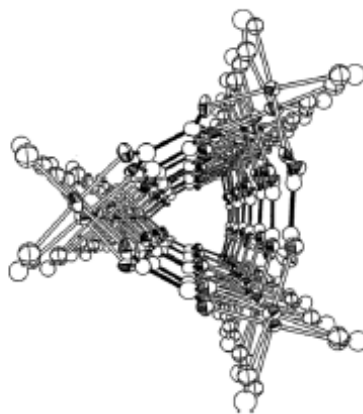


Fig.1.5 The solid-state stacking of triangles (containing dirhodium paddle-wheel SBUs) generates a 1-D tube [37].

In 2001, Cotton et al. [38] prepared the first neutral molecular triangle containing dimolybdenum paddle-wheel units (see Fig. 1.6).

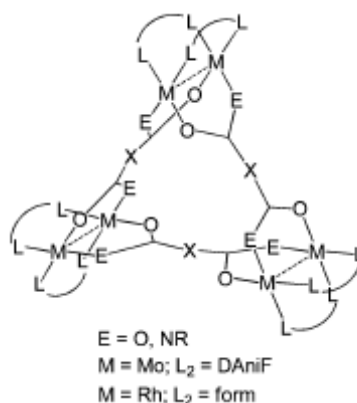


Fig.1.6 General structure of a molecular triangle containing dimetal units [38].

5.1.3 Square-shaped complexes.

Paddle-wheel dimetal complexes are applicable as SBUs for the construction of molecular squares (Fig. 1.7). In comparison to the structures described in the previous paragraphs, the formation of molecules with a square structure is only possible when the linker is linear and the torsion angle of the linker ligands coordinating to the M–M unit is 0° [39].

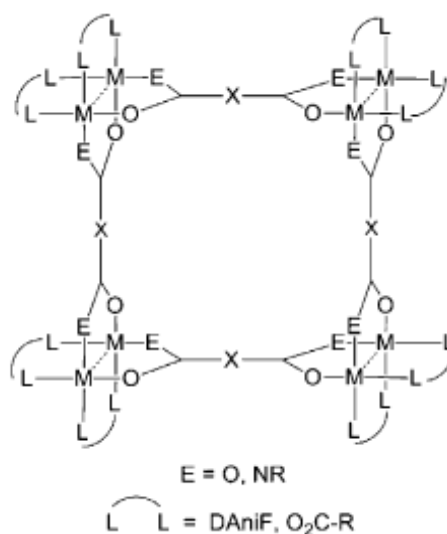


Fig.7 General structure of molecular squares [39].

In 1999, Cotton et al. prepared supramolecular squares with Mo corners linked via dicarboxylate bridges but a transformation from square to triangle in solution could not be excluded [40, 41]. Cotton et al. focused on the electrochemical behavior of synthesized molecular squares and so they noticed cyclic voltammograms indicating that these compounds undergo oxidation processes.

The first molecular box containing Rh₂ SBUs and carboxylates was prepared by Bonar–Law et al. in 1999 [42]. In order to reduce the possibility of uncontrolled polymerisation, [Rh₂(DAniF)₂(OAc)]₂, where DAniF=N,N'-di-p-anisylformamidinate, was used as connector. Via a carboxylate-exchange reaction, a cyclic tetramer could be obtained by connecting the cis-protected corner unit with benzene-1,4-dicarboxylic acid. Then, in 2000, Bonar–Law et al. synthesized macromolecular PW squares with substituted benzene-1,4-dicarboxylate linkers [43].

5.2 Two-dimensional paddle-wheel polymers

Two-dimensional paddle-wheel coordination polymers are mainly formed by the planar expansion of a PW complex in two equatorial directions. Using equatorial linkers bearing flexible angles between the carboxylate functionalities, basic networks can be obtained [44].

5.2.1 Equatorial linkage of paddle-wheels

Already in 1964, G. Wilkinson et al. described the synthesis of insoluble derivatives of $[\text{Mo}_2(\text{OAc})_4]$ with dicarboxylates, which the authors presumed to be of polymeric nature [45]. The connection of dimetal PW units by bifunctional equatorial linkers such as terephthalate, fumarate, 2,6-naphthalenedicarboxylate, trans-cyclohexanedicarboxylate, etc. leads to the formation of 2-D sheets of general structure as shown in Fig. 1.8.

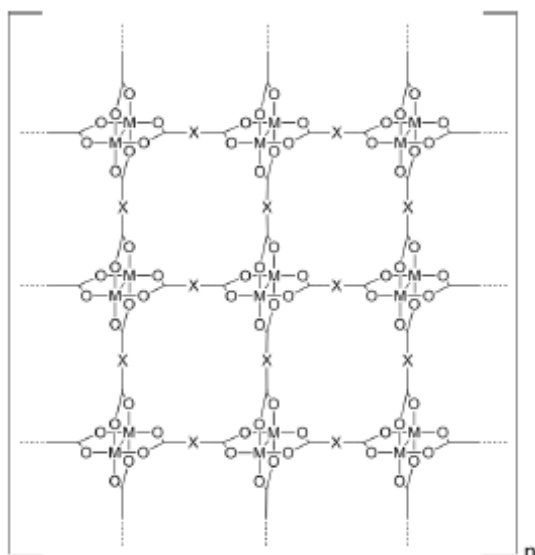


Fig.1.8 Infinite two-dimensional structure of metal(II) carboxylates $[\text{M}_2(\text{O}_2\text{C-X-CO}_2)_2]_n$ [45].

The teams of Yaghi and Mori were the first to designed 2-D polymers of the type $[\text{M}_2(\text{O}_2\text{C-X-CO}_2)_2]_n$ via equatorial linkage of in situ formed PW units [13, 46]. A series of coordination polymers (see Table 2) has been synthesised by the groups of Zaworotko [47], Fjellvåg [48], Tao [49], Hong [50], Li [51], Chen [52], Zhang [53], Lu [54], Han [55], Schröder [56], Wang [57], Maji [58], and Zhu [59].

In 1998, Yaghi et al. described the synthesis of a microporous metal–organic framework (MOF) $[\text{Zn}(\text{bdc})\cdot(\text{DMF})(\text{H}_2\text{O})]$ [13].

The 2-D layer is prepared by room temperature vapor diffusion of triethylamine and toluene into a DMF solution of $\text{Zn}(\text{NO})_2\cdot 6\text{H}_2\text{O}$ and 1,4-benzenedicarboxylate (bdc). Numerous 2-D MOFs have been isolated by Mori et al. in 2000 [60].

Noteworthy, $[\text{Cu}_2(\text{bdc})_2]_n$ is the first transition metal complex capable of adsorbing gases reversibly and is recognized as a principal complex in the construction of microporous coordination polymers. Usually, the reaction of copper formate with the corresponding dicarboxylic acid and formic acid in dry methanol yields the 2-D copper dicarboxylate $[\text{Cu}_2(\text{bdc})_2]_n$. In 2004, Mori et al. described the first 3-D nanoscale network consisting of a 2-D microporous complex $[\text{Mo}_2(\text{O}_2\text{C}-\text{C}_6\text{H}_4-\text{CO}_2)_2]_n$ linked by organic polymers (i.e. PEG) [61].

Author	M	X	L _{ax}
Yaghi	Zn	1,4-bdc	H ₂ O
Mori	Cu	C ₆ H ₄	
	Cu	C ₂ H ₂	
	Cu	C ₆ H ₁₀	
	Cu	C ₁₀ H ₆	
	Mo	C ₆ H ₄	
	Mo	C ₂ H ₂	
	Mo	C ₆ H ₁₀	
	Mo	C ₄ H ₄	
	Mo	C ₅ H ₃ N	
Zaworotko	Zn	1,3-bdc	pyridine
	Cu	1,3-bdc	pyridine
	Cu	1,3-bdc	4-picoline
	Cu	5-OEt-1,3-bdc	pyridine
	Cu	5-OPr-1,3-bdc	pyridine
	Cu	pdc	pyridine
	Cu	pdc	4-pic
	Cu	tdc	methanol
	Cu	tetrafluoro-1,3-benzene	quinoline
	Cu	tetrafluoro-1,3-benzene	ethanol
	Cu	tetrafluoro-1,3-benzene	2-picoline
Fjellvåg	Cu	ndc	pyridine
	Zn	ndc	3,4-dimethylpyridine
Tao	Zn	bpdc	DMSO
Hong	Cd	bdpa	dpe
	Cd	bdpa	Bpy
Li	Cu	adamantane	H ₂ O
Chen	Cu	bdc	DMF
Zhang	Cu	4,4'-oxydibenzene (oba)	DMF
Lu	Cu	CIP	H ₂ O
Han	Co	hfipbb	pyridine
Schröder	Zn	hfipbb	pyridine
Wang	Cu	CH ₃ O-ip	Bpa
Wang	Cu	CH ₃ O-ip	Bpp
Maji	Cu	1,4-ndc	MeOH
	Cu	1,4-ndc	bpy, bpe
Zhu	Cu	3,3'-dimethoxy-4,4'-biphenyl	DMF

Table 1.2 Overview of two-dimensional polymers of the general formula $[M_2(O_2C-X-CO_2)_2(L_{ax})_{1-2}]_n$ containing dimetal PW complexes [39].

In 2001, Zaworotko et al. synthesized undulating 2-D networks from the corresponding nitrates containing zinc and copper PW units which are linked by benzene-1,3-dicarboxylate having a 120° bent angle [47(a)]. In 2002, Fjellvåg synthesized copper and zinc PW coordination polymers having formula $[Cu(ndc)(pyridine)]$ and

[Zn(ndc)(3,4-dimethylpyridine)] by solvothermal treatment of the corresponding salts with 2,6-naphthalenedicarboxylic acid (ndc) and pyridine (Cu) or 3,4-dimethylpyridine (Zn), respectively [49]. PW complexes are connected to 2-D sheets through naphthalene rings which are structurally related to MOF-2 [13]. By means of weak interactions between the axial ligands, the extension of the 2-D network into three dimensions is possible. In 2002, Tao et al. synthesized a typical example of 2-D metal–organic framework comprising rigid 4,4'-biphenyldicarboxylates (bpdc) as equatorial linkers and zinc PW units [50]. The 2-D polymer, [Zn(bpdc)(DMSO)], is made by room temperature vapor diffusion of triethylamine into a DMSO solution containing $\text{Zn}(\text{NO}_3)_2 \cdot 6\text{H}_2\text{O}$ and H_2bpdc (Fig. 1.9).

In 2003, Zaworotko et al. reported on a series of copper based 2-D networks (see Table 1.2) from calixarene-like $[\text{Cu}_2(\text{dicarboxylate})_2]_4$ building blocks [47(b)]. Various angular dicarboxylate linkers such as benzene-1,3-dicarboxylate (1,3-bdc), benzene derivatives (5-OEt-bdc and 5-OPr-bdc), 1-methyl-pyrrole-2,4-dicarboxylate (pdc) and thiophene-2,5-dicarboxylate (tdc) are exploited to synthesize undulating 2-D sheets of the general formula $\{[\text{Cu}_2(\text{dicarboxylate})_2(\text{L}_{\text{ax}})_2]_4\}_n$.

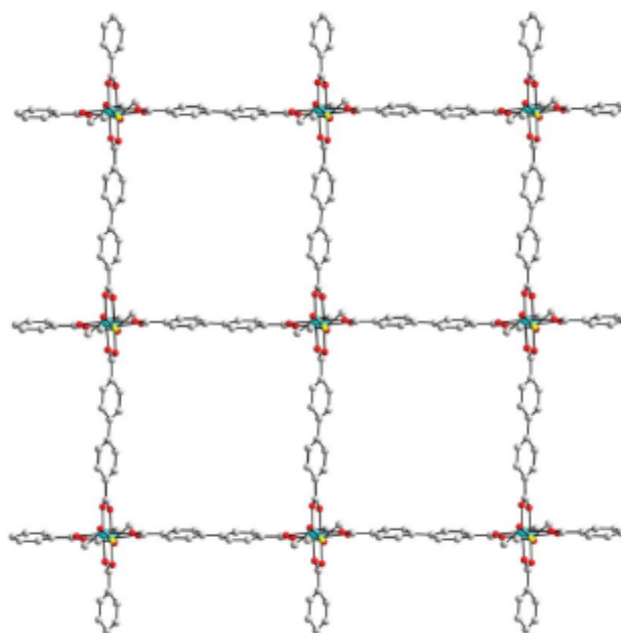


Fig.1.9 Typical example of a 2-D metal–organic framework. (Cu: turquoise, O: red, S: yellow, C: grey) [50].

For example, $\{[\text{Cu}_2(\text{pdc})_2(4\text{-pic})_2]_4 \cdot 4\text{H}_2\text{O}\}_n$ is obtained by slow diffusion of a methanol solution of H_2pdc and 4-picoline into a methanol solution of $\text{Cu}(\text{NO}_3)_2 \cdot 5\text{H}_2\text{O}$ containing nitrobenzene.

In 2007, Zaworotko's group focused on the construction of dynamic 2-D metal–organic polymers with variable pore structures using flexible tetrafluoro-1,3-benzene dicarboxylates (TFBDC) as equatorial linker and dicopper building units [47(c)]. Depending on the size and chemical nature of the crystallization template molecules (i.e. benzene derivatives), the intralayer and interlayer cavities of 2-D sheets are varied. Polymeric compounds are synthesized by layering method using copper(II) nitrate, H_2TFBDC (2,3,5,6-tetrafluoroterephthalic acid) and different axial linker (i.e. quinoline, 2-picoline or ethanol) and different template molecules (i.e. mainly benzene derivatives).

Fluorine-substituted benzene carboxylates embody different torsion angles due to $\pi\cdots\pi$ interactions of opposite ligands. The cavity can be flexibly opened and closed for guest molecules. As one of the first, Zaworotko realized the opportunity of synthesizing MOFs bearing the coexistence of two types of guest-dependant cavities in regards of functional materials such as sensors.

In 2006, Li et al. reported on a 2-D network structure generated by the equatorial connection of $[\text{Cu}_2(\text{ada})_4]$ PW cluster through adamantinediacetates (ada). The 2-D layers of the formula $[\text{Cu}_2(\text{ada})_2(\text{H}_2\text{O})_2]$ are prepared under hydrothermal conditions heating a solution of $\text{Cu}(\text{NO}_3)_2$ and H_2ada in distilled water for 5 days at 120 °C [51].

In 2007, Chen et al. synthesized a porous coordination polymer, $[\text{Cu}_2(\text{bdc})_2(\text{DMF})]_n$ (bdc = 1,3-benzendicarboxylate, DMF=N,N'-dimethylformamide), with gas sorption properties [53]. The bridging of Cu–Cu PW units by dicarboxylate linkers (bdc) leads to the formation of 2-D layers. The pillaring of the latter through van der Waals interactions results in generating 3-D supramolecules bearing 2-D channels. The treatment of $\text{Cu}(\text{NO}_3)_2 \cdot 6\text{H}_2\text{O}$ with 1,3-benzenedicarboxylate in presence of benzimidazole affords a dynamic coordination polymer.

In 2008, Zhang and coworkers synthesized a 2-D polymer, $[\text{Cu}_2(\text{oba})_2(\text{DMF})_2] \cdot 5.25\text{DMF}$, bearing dicopper PW units connected by equatorial 4,4'-oxydibenzenedicarboxylate (oba) linkers by a microwave-assisted method [53]. In 2009, Lu and co-workers reported

on a large 3-D framework consisting of 2-D square grids with the large dimensions of $25.5 \times 25.5 \text{ \AA}^2$ [54].

The assembly of PW clusters through bulky pyrene-based dicarboxylates (cip) leads to the formation of 2-D sheets. The latter are stacked via NH...H interactions into a 3-D structure with large pores suitable for gas adsorption. The solvothermal reaction of $\text{CuCl}_2 \cdot \text{H}_2\text{O}$ and H_2cip in DMF for 2 days at $160 \text{ }^\circ\text{C}$ results in the synthesis of $[\text{Cu}(\text{cip})(\text{H}_2\text{O})] \cdot 4 \text{ H}_2\text{O} \cdot 5 \text{ DMF}$.

In 2009, Han et al. synthesized 2-D and 3-D polymers of helical structures based on cobalt PW units [55].

The hydrothermal reaction of $\text{CoCl}_2 \cdot 6\text{H}_2\text{O}$ with H_2hfipbb [4,4'-(hexafluoroisopropylidene)bis(benzoic acid)] and pyridine in water results in the formation of the 2-D net $[\text{Co}(\text{hfipbb})(\text{py})]$. The parallel interpenetrating helical double layers can be extended to 3-D framework by substituting the monodentate pyridine ligands by the exo-bidentate ligand 1,3-bis(4-pyridyl)propane (bpp).

Schröer et al. connected zinc PW complexes with axial pyridine linkers and equatorial dicarboxylate linkers as 4,4'-(hexafluoroisopropylidene)bis(benzoic acid) [56]. The solvothermal reaction of $\text{Zn}(\text{NO}_3)_2 \cdot 6\text{H}_2\text{O}$, H_2hfipbb and py in DMF at $120 \text{ }^\circ\text{C}$ for 3 days results in the formation of a 2-D undulating net with large rhomb-like windows formulated as $[\text{Zn}_2(\text{hfipbb})_2(\text{py})_2] \cdot \text{DMF}$. Each PW cluster is linked to four neighbouring PW units by bridging hfipbb^{2-} dianions. Using a longer axial linker such as 1,4-bis(4-pyridyl)-2,3-diaza-1,3-butadiene (bpdab) instead of pyridine yields the

3-D polymeric network $[\text{Zn}_2(\text{hfipbb})_2(\text{bpdab})] \cdot 2 \text{ DMF}$. Hence, the length of the axial linker is playing a crucial role in the extension of 2-D nets to 3-D networks.

In 2010, Wang et al. synthesised 2- and 3-D polymers by a typical solvothermal method using copper acetate, 5-methoxyisophthalic acid ($\text{CH}_3\text{O}-\text{H}_2\text{ip}$) as equatorial linker, and 1,2-bi(4-pyridyl)ethane (bpa) or 1,3-di(4-pyridyl)propane (bpp), respectively, as axial linkers [59]. The final structure of the coordination polymer is depending on the length of the axial linker. Using bpa yields a 2-D layer, whereas using bpp (one more CH_2) results in the assembly of a 3-D network, consisting of 2-D sheets with dangling bpp lateral arms.

In 2010, Maji's research group synthesized 2- and 3-D polymers having formula $\{[\text{Cu}_2(1,4\text{-ndc})_2\text{S}_2]\}$ (1,4-ndc = 1,4-naphthalene dicarboxylate; S = MeOH or H_2O) [58(a)]. In this work, a solution of $\text{CuSO}_4 \cdot 5\text{H}_2\text{O}$ in MeOH (1 equiv.) is carefully layered over the ligand solution (1 equiv. 1,4-ndc and 2 equiv. KOH in H_2O) to yield $\{[\text{Cu}(1,4\text{-ndc})(\text{MeOH})] \cdot \text{MeOH}\}$ in crystalline form. The stacking of the 2-D square grids affords a 3-D structure with triangular channels occupied by solvent molecules. Moreover, Maji et al. reported on two microporous coordination polymers formulated as $[\text{Cu}_3\text{L}_{1.5}(1,4\text{-ndc})_3]$ (L = bipy or bpe) [58(b)].

In 2009, Choe et al. reported on a series of porphyrin paddle-wheel frameworks (PPF) synthesized by solvothermal method. The frameworks are built from 2-D sheets which are pillared by bipyridine. The 2-D layers are designed through equatorial linkage of M-M units (M = Co, Zn) by 5,10,15,20-tetrakis(4-carboxyl)-21H,

23H- porphyrin (TCPP) [62]. They also reported on two series of highly tunable heterometallic frameworks constructed from PW units (M = Zn and Co) and metalloporphyrin (M = Mn, Fe, Ni, V and Pt) [63]. The metal composition can be controlled by incorporating a wide range of metals. The resulting heterometallic frameworks exhibit either the NaCl structure, or a rare fsc topology (AA type). The same group reported on a series of frameworks (PPF-18-22) based on a 2-D porphyrin paddle-wheel grid [64]. The 3-D frameworks are obtained by the solvothermal reaction of TCPP, $\text{Zn}(\text{NO}_3)_2 \cdot 6\text{H}_2\text{O}$ and HNO_3 with N,N'-di-(4-pyridyl)-1,4,5,8-naphthalenetetracarboxydiimide (DPNI) or 3,6-di-4-pyridyl-1,2,4,5-tetrazine (DPT) as pillar ligands, respectively. Depending on the initial molar ratio of the reactants (TCPP/Zn/DPNI or DPT), the formation of bilayer and fsc topologies are observed.

5.2.2 Axial linkage of paddle-wheels.

In 2000, Robson et al. synthesized a 2-D sheet bearing hexagonal windows via axial linkage of Cu PWs by 2,4,6-tri(4-pyridyl)-1,3,5-triazine (tpt) [65]. The 2-D polymer is obtained by slow diffusion of a methanol solution of copper acetate into a solution of tpt in benzyl alcohol.

In 2006, Ohmura et al. synthesized a porphyrin based MOF supported by copper acetate which are axially linked by H_2TPyP (pyridylporphyrin). The porous structure is constructed by the self-assembly of a 2-D network consisting of a 22.2 Å grid [66]. The

treatment of copper acetate with H₂TPyP yields the first porphyrin-based MOF.

In 2008 Hu et al. reported the synthesis of a 2-D network, [Cu₂(OAc)₄(ma)(H₂O)]₂[Cu(hpe)₂] (ma = melamine, hpe = 1-(2-hydroxyphenyl)ethanone), consisting of a mononuclear copper unit and a dinuclear copper unit in which the apical positions are occupied by two different donor ligands (MA and water) [67]. The 2-D layers are formed through strong hydrogen bonds with different modes.

In 2010, Dunbar et al. synthesized a series of ruthenium- and rhodium-based two-dimensional fishnet-type networks containing PW complexes. The compound [Ru₂(O₂C-CF₃)₄] was axially linked by neutral derivatives of 7,7,8,8-tetracyanoquinodimethane (TCNQ) ligands [68].

5.2.3 2-D polymers from double strained chains.

2-D coordination polymers containing double strained 1-D chains of cisbridged PW units have been synthesised using flexible linkers such as succinate, cis-porphyrin, cyclohexanedicarboxylate, etc.

As an example, in 2007, Mao et al. synthesized a metal–organic 2-D coordination polymer of the formula [Cu₂(succinate)₂(H₂O)₂] (see Fig. 1.10) consisting of double-strained 1-D chains which are interconnected to each other by means of hydrogen bonding between water and carboxylate [69].

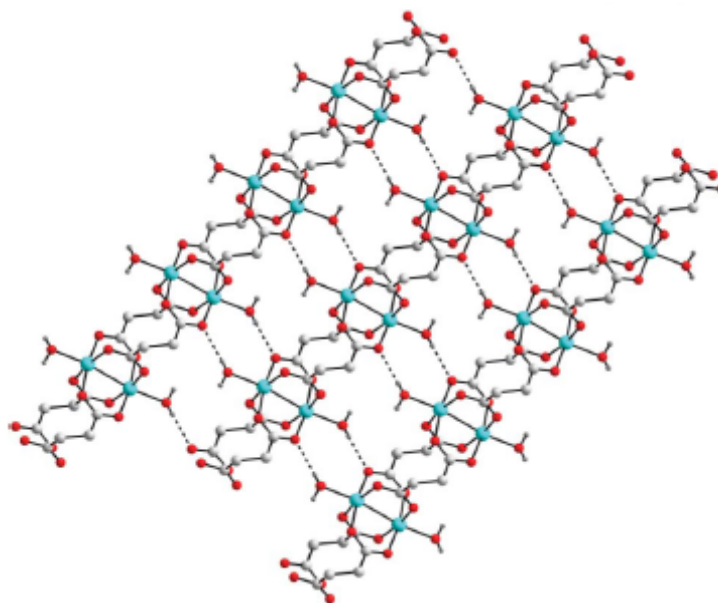


Fig.1.10 Flexible aliphatic dicarboxylates i.e. succinate form double-strained 1-D chains stacked together via hydrogen bonding in order to form a 2-D network (Cu: turquoise, O: red, C: grey) [69].

In 2008, Choe et al. prepared the mixed-linker porphyrin 2-D framework PPF-6 with CdI_2 structure by solvothermal reaction of $\text{Co}(\text{NO}_3)_2 \cdot 6\text{H}_2\text{O}$, zinc 5,10-di(4-carboxyphenyl)-15,20-diphenylporphyrin (cis-ZnDCPP) and 4,4'-bipyridine [70]. 1-D chains resulting in the connection of Co–Co units by four cis- ZnDCPP are further stacked into 2-D layers by the interaction of bpy ligands whose nitrogen atoms bind to the axial site of the copper PW and the central zinc atoms within the porphyrin ring. This study shows how the number of carboxylic groups of the ligand affect the overall topology of framework.

6. Three-dimensional cage compounds and polymers

6.1. Metal–organic polyhedra (MOP)

The synthesis of three-dimensional cage compounds from paddlewheel complexes requires the exchangeability of all equatorial ligands. Of course, this reaction always competes with the formation of polymeric network structures. However, in certain cases, the linker modification allows the isolation of metal–organic polyhedrons (MOP) with paddle-wheel corners [71].

6.1.1. MOPs with two and three paddle-wheel SBUs.

In 2010, Lah et al. developed a general strategy for edge-directed self assembly of tetragonal metal–organic polyhedral [72]. A solvothermal reaction of 3,3'-[1,3-benzenediyl-di(ethynyl)]dibenzoic acid ($=\text{H}_2\text{L}$) with $\text{Cu}(\text{NO}_3)_2 \cdot 3 \text{H}_2\text{O}$ led to the formation of a dicopper paddle-wheel cage.

Recently, Zhou et al. reported molecular cages Mo_4L_4 consisting of two dimolybdenum units surrounded by four dicarboxylate moieties ($\text{L} = 3,3'$ -(pyridine-2,6-diyl)dibenzoate(3,3'-PDDB²⁻), 3,3'-[1,3-phenylenebis(ethyne-2,1-diyl)] dibenzoate (3,3'-PBEDDB²⁻), or 3,3'-(2-amino-5-isopropyl-1,3-phenylene)bis-(ethyne-2,1-diyl) dibenzoate (2-NH₂-5-i-Pr-3,3'-PBEDDB²⁻)), bearing a bridging angle of 0° [73]. These lantern-type structural arrangements are synthesized by a solvothermal reaction of $\text{Mo}_2(\text{CF}_3\text{COO})_4$ and the corresponding bridging ligand L in a 1 : 2 ratio.

A solvothermal reaction of 1,4-bis(3-carboxylphenylethynyl)-benzene (H_2L) with $Cu(NO_3)_2 \cdot H_2O$ affords the metal–organic macrocycle (MOM) $[(Cu_2)_3L_6(DMF)_2(H_2O)_4]$ (Fig. 1.11) [74].

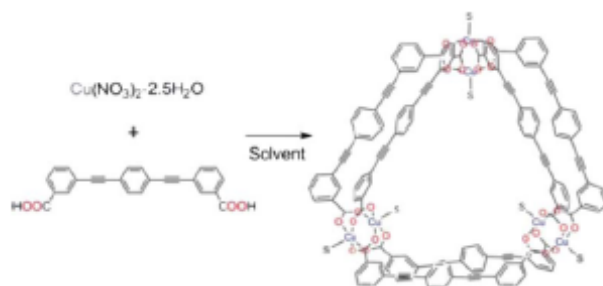


Fig.1.11 Schematic diagram showing the synthesis of a double-walled triangular MOM based on copper paddle-wheel SBUs using a long and “pseudo-rigid” dicarboxylic acid and a Cu(II) ion [74].

The MOM has a double-walled triangular geometry with three Cu SBUs which are connected by the long and ‘pseudo rigid’ ligands in a cis-manner [74].

In 2010, Zhou et al. reported of hexanuclear molecular rings having general formula Mo_6L_6 ($L = 3,3'$ -(ethyne-1,2- diyl)dibenzoate ($3,3'$ -EDDB $^{2-}$), $4,4'$ -(1,2-phenylene)bis(ethyne-2,1-diyl(dibenzoate) ($4,4'$ -PBEDDB $^{2-}$) and $4,4'$ -(4,5-dimethoxy-1,2-phenylene)bis(ethyne-2,1-diyl(dibenzoate) ($4,5$ -(MeO) $_2$ - $4,4'$ -PBEDDB $^{2-}$)) [73]. Six linkers bearing a bridging angle of 60° assemble three Mo_2 units in a trigonal prismatic way. The solvothermal reaction of $[Mo_2(O_2C-CF_3)_4]$ and the corresponding dicarboxylate linker L in a 1 : 2 ratio leads to the formation of equilateral triangles. In each synthesis, one drop of HBF_4 (40% in water) is added to the reaction solution.

6.1.2 Tetrahedral MOPs.

In 1999, Cotton et al. synthesized a large tetrahedral molecule containing four triply-bridging $C_6H_3(CO_2)_3$ (trimesic acid trianion) groups and six $Mo_2-(DAniF)_2$ ($DAniF = N,N'$ -di-*p*-anisylformamidinate) units. The midpoints of the four planar linkers form a tetrahedron and the centroids of the dimetal units generate an octahedron [75]. The synthesis of the rhodium analogue is also possible. Both of the neutral tetrahedral cages are able to clathrate solvent molecules, CH_2Cl_2 in the case of Mo and CH_3CN for Rh [76].

6.1.3 Octanuclear cages.

In 2004, Cotton et al. reported the isolation of a spheroidal carceplex, consisting of four singly-bonded Rh_2^{4+} units enclosed by two bowl-shaped calix[4]arenes [77]. The treatment of $[cis-Rh_2(DAniF)_2(CH_3CN_{eq})_4(CH_3CN_{ax})_2][BF_4]_2$ with salts of calix[4]arene(CO_2H)₄ in 2 : 1 ratio allowed the formation of the octanuclear complex. It should be noted that long reaction time (at least 7 d) and reaction temperature at 35– 40°C are very important for the success of the reaction. The cage can trap an ether molecule or a NEt_4^+ cation.

6.1.4 MOPs composed of five Cu_2 units.

A nanometre-sized metallocage containing five Cu paddle-wheel units has been prepared according to a layering method by Sun et al. in

2006 [78]. A solution of benzene-1,3,5-triacetic acid (H_3bta) and $KHCO_3$ in water is slowly added to a solution of $Cu(ClO_4)_2 \cdot 6H_2O$ in water. After standing at ambient temperature for several days, water insoluble crystals were obtained. The flexible tripodal H_3bta ligand acted as a secondary building unit to generate a novel discrete cage-like structure $[Cu_{11}(bta)_6(Hbta)_2(H_2O)_{10}] \cdot 29 H_2O$. It is noteworthy that only the *cis,cis,cis*-conformation of the ligand was observed. The structure of the metallocage can be described as a near cuboctahedron composed of square (paddle wheels) and triangular (tripodal bta ligand) secondary building units.

6.1.5 Octahedral MOPs.

An example of truncated octahedral cages is MOP-28 prepared by Yaghi's group of in 2005. The porous metal-organic truncated octahedron is composed of six $[Cu_2(CO_2)_4]$ paddle-wheel building blocks and twelve 2,2':5',2''-terthiophene-5,5''-dicarboxylate (TTDC) linking units [79].

The synthesis of an octahedral cage has been reported in 2009 by Lah et al., who prepared a self-assembled MOP consisting of a truncated octahedron made up of six Cu_2 PW SBUs at the truncated corners of the octahedron and eight ligand molecules occupying the faces of the octahedron. The overall charge is zero [80, 81].

Recently, the solvothermal synthesis of octahedral cages having the general formula $Mo_{12}L_{12}$ was reported by Zhou's group [73]. The treatment of $[Mo_2(O_2C-CF_3)_4]$ with 9H-3,6-carbazoledicarboxylic acid

[H₂(9H-3,6-CDC)] or 4,4'-(9Hcarbazole-3,6-diyl)dibenzoic acid [H₂(4,4'-CDDDB)] in a 1 : 2 ratio for 2 days at 85 °C or 6 days at 100 °C afforded the formation of the cages. In both syntheses, one drop of HBF₄ (40% in water) was added to the reaction solution. On the one hand the bridging angle controls the geometric shape of the cage, on the other hand the size of the octahedral array is determined by ligand size.

6.1.6. Cuboctahedral MOPs.

In 2001, Yaghi and O’Keeffe constructed a large metal–organic polyhedron termed MOP-1 containing twelve Cu₂ paddle-wheel building blocks bridged by 1,3-benzenedicarboxylate (m-bdc) ligands. The angle between the two functional groups of the linker is 120° and therefore suitable for the design of truncated cuboctahedron structures. The ball-and-stick model of MOP-1 is shown in Fig. 1.12 [82].

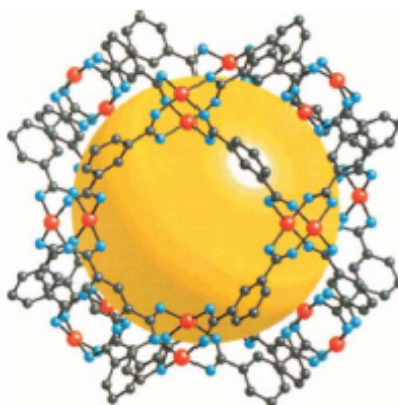


Fig.1.12 Crystal structure of MOP-1 with a diameter of 15 Å. The assembly of twelve Cu paddle-wheel SBUs and 24 m-BDC ligands affords the formation of a truncated cuboctahedron. 50 water, 6 ethanol and 6 DMF molecules acting as guests are omitted [82].

In 2010, Zhou et al. synthesized a porous coordination nanocage, CuTEI, which can be used for gas separation purposes [83, 84]. The solvothermal reaction of $\text{Cu}(\text{NO}_3)_2 \cdot 2.5 \text{H}_2\text{O}$ with deprotonated 5-((triisopropylsilyl)ethynyl)isophthalic acid (TEI) leads to the formation of a functionalized nanoball containing 12 Cu paddle-wheel clusters and 24 TEI ligands. The bulky triisopropylsilyl (TIPS) groups are covering the outside of the nanoball.

6.1.7. Rhombicuboctahedral MOPs.

The reaction of $\text{Cu}(\text{OAc})_2 \cdot \text{H}_2\text{O}$ and 5-dodecoxybenzene-1,3-dicarboxylic acid in DMF led to the formation of MOP-18, a nanosized metal–organic polyhedron, with the crystal formula formulated as $[\text{Cu}_{24}(\text{5-OC}_{12}\text{H}_{25}\text{-m-bdc})_{24}(\text{DMF})_{12}(\text{C}_8\text{H}_{17}\text{OH})_4(\text{H}_2\text{O})_8 \cdot (\text{DMF})_{20}(\text{C}_8\text{H}_{17}\text{OH})_4(\text{H}_2\text{O})_8]$ [85]. 12 Cu_2 PW units are connected by 24 functionalized linkers to create a rhombicuboctahedron. By means of dicarboxylate links providing the required 120° angle the design of the rhombicuboctahedron is predetermined.

6.1.8 Rhombihexahedral cages.

The idea to use metal–organic polyhedra as building units for the synthesis of infinite coordination polymers is quite attractive [86], since many 3-D MOFs exhibit substructures which are analogous to platonic bodies or to inorganic materials, such as zeolites [87].

Thus, by connecting MOPs with the right linker, similar structures could be obtained. Zaworotko et al. showed that a paddle-wheel MOP can undergo a modular self-assembly to a 3-D network [88]. By combining 12 Cu₂ SBUs with 24 bdc ligands, they prepared discrete the nanoscale small rhombihexahedra [(S)₂Cu₂(bdc)₂]₁₂ and [(L)(S)Cu₂(bdc)₂]₁₂, (L = pyridine, S = methanol). The chemical properties of these rhombihexahedral nanoballs are porosity, presence of accessible sites, chemical resistance, solubility and neutrality.

6.1.9 Relation between the linker and the type of polyhedra.

Table 1.3 gives an overview of the relationship between the symmetry and shape (angle) of the linker and the polyhedral MOP structure. The following trend is clearly related to compounds of general formula M_nL_n: by choosing linkers such as m-bdc, with a bridging angle of around 120°, cuboctahedral, anticuboctahedral, rhombicuboctahedral and rhombihexahedral structures (n = 24) are accessible. The application of linkers with a bridging angle of 90° leads to octahedral assemblies (n = 12). Using dicarboxylic acids with a linking angle of 60°, the design of triangular cages is possible (n = 6). Tetragonal cages (n = 4) can be synthesized by means of U-shaped linkers with a bridging angle of 0°.

Author	Linker (L)	Symmetry of L, approx. linking angle	Type of polyhedra M_nL_n
Lah	3,3'-(1,3-benzenediyl-di(ethynyl))dibenzoate	C_{2v} , 0°	Tetragonal cage, Cu_4L_4
Zhou	3,3'-PDDB ²⁻	C_{2v} , 0°	Lantern-type cage, Mo_4L_4
Lah	1,4-bis(3-carboxyl-phenylethynyl)benzene	C_{2v} , 60°	Triangular cage, Cu_3L_3
Zhou	3,3'-EDDB ²⁻	C_{2v} , 60°	Triangles, Mo_3L_3
Cotton	Trimesic acid	D_{3h} , 120°	Tetrahedron, M_4L_4
Chisholm	3,4-thienyl-dicarboxylate	C_{2v} , 70°	Tetrahedron, M_4L_4
Cotton	Calix[4]arene(CO ₂ H) ₄	C_{4v} , 0°	Spheroidal carcuplex, cage, Rh_3L_2
Sun	H ₃ bta	D_{3h} , 120°	Nearly cuboctahedral, $Cu_{11}L_8$
Yaghi	TTDC	C_{2v} , 90°	Octahedral cage, $Cu_{12}L_{12}$
Lah	tris(benzoate)	C_{3v} , 120°	Octahedral cage, $Cu_{12}L_8$
Zhou	H ₂ (9H-3,6-CDC)	C_{2v} , 90°	Octahedral cage, $Mo_{12}L_{12}$
Yaghi	<i>m</i> -bdc	C_{2v} , 120°	Cuboctahedral, $Cu_{24}L_{24}$
Yaghi	<i>R-m</i> -bdc, 2,7-ndc and 2,7-bpdc	C_{2v} , 120°	Cuboctahedral, $Cu_{24}L_{24}$
Zhou	<i>R-m</i> -bdc	C_{2v} , 120°	Cuboctahedral, anticuboctahedral, $Mo_{24}L_{24}$
Zhou	TEI	C_{2v} , 120°	Cuboctahedral, $Cu_{24}L_{24}$
Zhou	<i>R-m</i> -bdc	C_{2v} , 120°	Cuboctahedral, anticuboctahedral, $Mo_{24}L_{24}$
Yaghi	<i>R-m</i> -bdc	C_{2v} , 120°	Rhombicuboctahedral, $Cu_{24}L_{24}$
Zaworotko	<i>R-m</i> -bdc	C_{2v} , 120°	Rhombihexahedral, $Cu_{24}L_{24}$

Table 1.3 Relationship between the linker geometry and the product structure [39].

6.2 Three-dimensional metal–organic frameworks (MOFs) with ‘paddle-wheel’ secondary building units.

Metal–organic frameworks are three-dimensional, porous coordination polymers with a long-range order. The crystal structure, and, consequently, the pore size and the physical-chemical properties largely depend on two factors: the secondary building unit and the organic linker. To date, a plethora of different SBUs (among them, the paddle-wheel SBUs) and various linkers have been used for the synthesis of MOFs [89]. Due to the vast number of different 3D-MOFs, in this work we will only focus on the most recent and most literature-known representatives. To date, ordered porous metal–organic coordination polymers containing paddlewheel SBUs are solvothermally synthesized by two different routes:

- 1) The stacking of 2-D polymer layers with amine-, pyridine- or nitrile-based linkers. Usually, the reactions are one-

pot mixtures of a metal salt (hydrate), a carboxylic linker and a linear linker. The paddle-wheel unit is formed in situ, building up a 2-D layer, whereupon the linear linker connects two layers, acting as a pillar (Fig.1.13).

2) By direct solvothermal reaction of metal salts and di- or trifunctional linkers. Here, the shape of the carboxylic acid controls the formation of 3-D networks instead of 2-D layers.

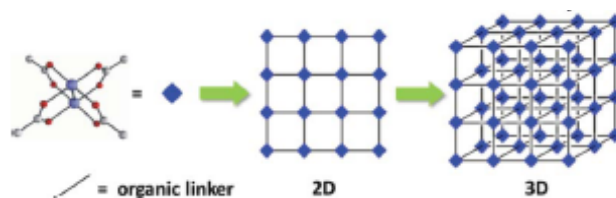


Fig.1.13 Step-by-step formation of a 3-D porous network [89].

6.2.1 Stability of 3D PW-MOFs towards acids, bases and water.

MOFs have become ubiquitous in the literature for their potential in a plethora of applications. Hence, for a practical use, the knowledge of their stability towards air, acids, bases and water is very important. On the one hand, the axial coordination sites of almost every MOF are occupied by strong guest molecules such as DMF, DMSO, alcohols or water (e.g., see Yaghi's MOF family and Williams' HKUST-1) Another important factor affecting the structural stability is entropy. The decrease of entropy in the case of replacement of one bidentate dicarboxylate by two monodentate ligands such as water is not energetically favored. Hence, MOFs can be considered as water and

base stable networks. On the other hand, there is no stability towards acids since a protonation of the dicarboxylates leads to the cleavage of M–O bonds. For instance, the reaction of $[\text{Mo}_2(\text{OAc})_4]$ with $\text{HBF}_4 \cdot \text{OEt}_2$ in acetonitrile results in the formation of the cationic complex $[\text{Mo}_2(\text{CH}_3\text{CN})_{10}][\text{BF}_4]_4$ where the Mo_2^{4+} core is entirely surrounded by acetonitrile [90].

Notably, the smallest PW complex $[\text{Mo}_2(\text{OAc})_4]$ is also sensitive to O_2 , whereas PW complexes and MOFs of later transition metals, such as HKUST-1 (which contains copper), are air-stable. This is obviously related to the Lewis acidity of the respective metal.

6.2.2 3-D MOFs by stacking of 2-D MOFs.

In 2000, Mori et al. synthesized 3-D polymers from Cu_2 , Mo_2 , Ru_2 , and Rh_2 dicarboxylates, namely fumarate, naphthalenedicarboxylate, and cyclohexanedicarboxylate [46].

In 2002, the same group synthesized different 3-D networks from solutions of 2-D layers after addition of the axial linker triethylenediamine [91, 92]. The 2-D layers were made of Cu_2 cores equatorially linked by fumarate, terephthalate, or 4,4'-biphenyl dicarboxylate, demonstrating the influence of the different length of dicarboxylate on the adsorption properties. Later on, the same investigators brought a comprehensive survey on the properties and possible applications of networks containing transition metals [92, 93, 94]. They used Rh_2 , Ru_2 , and Mo_2 PW units connected by metalloporphyrin benzoate with Cu, Ni, or Pd as the metal centre of

the metalloporphyrin. Subsequently, several groups have overtaken this synthesis principle and studied the gas storage and magnetic properties of the so-obtained MOFs. Moreover, they investigated the opportunity to functionalize the linkers [95-102].

Based on the work of Mori et al., Kim et al. presented MOFs with dynamic properties based on different adsorbed guest molecules [103]. The 3-D network consisting of Zn_2 2-D networks, connected with dabco ‘pillars’, shrinks and expands based on the release or adsorption of the aforementioned guest molecules. In particular, the gas sorption behaviour of a series of zinc-PW-based MOFs containing tetramethyl-terephthalate, 1,4-naphthalenedicarboxylate, tetrafluoro-terephthalate, or 2,6- naphthalene dicarboxylates and various axial linkers was studied [104].

Analogously, Lah et al. synthesized a Zn-PW-MOF using 1,4-Bis(3-carboxylphenylethynyl)benzene linkers, obtaining an interwoven network [105].

In 2007, Férey’s and Fedin’s groups used chiral Zn_2 camphorate and linear N-donor ligands (dabco, bipyridyl and pyridyl ethylene) to synthesize a series of 3-D isorecticular, porous, homochiral frameworks [106].

Analogously, Kaskel et al. synthesized a cobalt-MOF, composed of 2-D polymeric $[Co_2(bdc)_2]_n$ units connected by dabco [107], while Chen’s research group developed porous metal–organic frameworks which operate as molecular recognition platforms. The identification of molecules in functionalized pores is governed by weak interactions

between the network and the guest molecule. The microporous network is synthesized in a simple self-assembly process of paddle-wheel units, organic dicarboxylic acid, and pillar bidentate linkers. Cu_2 , Co_2 , and Zn_2 nodes were bridged equatorially by 1,4-cyclohexanedicarboxylate [108], 2,6-naphthalenedicarboxylate [109,110], 4,4'-azobenzene-dicarboxylate [111], fumarate [112], methylglutarate [113], 4-carboxy-cinnamic acid [114], and 1,4-benzene-dicarboxylate [115] using axial bipy- or pyridyl ethylene linkers.

Furthermore Kitagawa et al. synthesized 2- and 3-D polymers consisting of a Cu_2 core and tetrafluorobenzene-1,4-dicarboxylic acid (tfbdc) and diazabicyclooctane as equatorial and axial ligands, respectively [116]. In analogy to Mori's synthesis protocol, first, the 2-D network was obtained by stirring copper formate and tfbdc in a MeOH–EtOH solution at 25°C. Thereafter, the 2-D network was treated with dabco, yielding a 3-D MOF.

The same research group synthesized a similar, photoactive 3-D porous network [117]. They used anthracene carboxylates and diazabicyclooctane as suitable photoactive ligands to connect Zn_2 clusters. They observed photoinduced charge transfer interactions between anthracene π walls and different adsorbed guests such as N,N-dimethylaniline, N-methylaniline, and N,N-dimethyl-ptoluidine.

Also Hupp and co-workers synthesized a series of MOFs containing Zn_2 units with different equatorial ligands (namely, fumarate, benzoate, naphthalate and biphenyldicarboxylate) and bipyridine and 1,4,5,8-naphthalenetetracarboxydiimide pillars [118]. Further, they

used salen-based pillars. Hence, Hupp et al. were able to anchor catalytically active metal complexes, such as Jacobsen's Mn(salen) epoxidation catalyst, on the MOF [119]. They found that the framework containing manganese species enhances the catalyst stability and size selectivity and permits catalyst separation and reuse.

6.2.3 Direct formation of 3-D MOFs.

The probably most known example for a MOF composed of paddle-wheel units is the HKUST-1 framework by Williams et al. (Fig. 1.14) [12]. The Cu-based HKUST-1 was synthesized from the reaction of $\text{Cu}(\text{NO}_3)_2 \cdot 3\text{H}_2\text{O}$ with trimesic acid in a 1:1 water–ethanol solution at 180°C for 12 h in an autoclave. The product (60% yield) is however accompanied by metallic copper as well as by cuprous oxide. Thermal gravimetric analysis indicates that the framework is stable up to 240 C.

Subsequently, the magnetic properties, as well as the gas adsorption of this network, have extensively been studied [120].

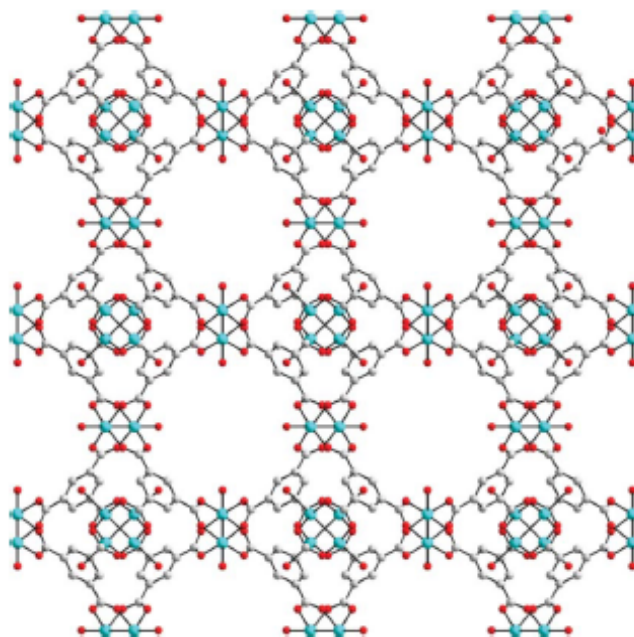


Fig.1.14 $[\text{Cu}_3(\text{tma})_2(\text{H}_2\text{O})_3]_n$ framework view along the (100) lattice plane (Cu: turquoise, O: red, C: grey) [12].

Even Mo-MOFs were synthesized. Kaskel's group synthesized a microporous metal-organic framework named TUDMOF-1 which is based on quadruple bonded Mo_2 units connected by 1,3,5-benzene tricarboxylates [121]. A reversible structural transformation of the network upon inclusion or removal of guest molecules was observed. Surprisingly, the framework is air sensitive, and the desolvated compound is reported to be pyrophoric (TGA indicates decomposition above 375°C).

In 2010, the same research group studied the effect of the reaction temperature and the presence of acid on the synthesis of MOFs [122]. The combination of a tetradentate ligand (benzidinetetrabenzoate) and the corresponding zinc, copper, or cobalt salt yielded 3-D nets with

PW units. However, it is not clear how the specific factors influenced the product morphology.

The typical synthesis of MOFs is carried out preparing an aqueous solution with metal salts and the linker, i.e. the carboxylic acid, and this solution is put in a autoclaves and subjected to high pressure at elevated temperatures. By this method, solvothermal method, almost all classical representatives of Yaghi's MOF family were synthesized.

In 2000, Yaghi and O'Keeffe introduced a porous metal-organic network composed of equatorial 1,3,5,7-adamantane tetracarboxylic acid (H_4atc) and a Cu_2 core, labelled as MOF-11 with general formula $[Cu_2(atc) \cdot 6H_2O]$ [123]. This compound contains open metal sites which do not aggregate due to structural rigidity. Hence, MOF-11 represents a promising candidate for catalytic applications. The Cu-Cu and Cu-O distances within the anhydrous framework are shortened after removal of water ligands (no decomposition below 260 C), demonstrating the influence of axial ligands on the length of M-M and M-O bonds. In general, the presence of axial ligands causes an elongation of the M-M bond [124]. The same research group also synthesized MOFs with open metal sites (i.e. without axial ligands) from a dimeric terbium cluster and terephthalic acid as building units [125]. The terbium complex nevertheless does not exhibit a clear paddle wheel morphology.

Later, the same authors synthesized MOF-14, which is composed of Cu_2 metal cores and 4,4',4''-benzene-1,3,5-triyl-tribenzoic acids, exhibiting an interwoven structure. MOF-14 is stable in air and insoluble in water [126].

In 2001, Yaghi and O’Keeffe introduced a series of metal organic frameworks (MOF-31 to MOF-39), based on various metal clusters and organic ligands of different morphology [127]. One of the networks, MOF-36, consists of paddle wheel Zn_2 units bridged by four methanetetraobenzoates and water ligands at the axial position of zinc.

In the same year, Yaghi and O’Keeffe used bromine-substituted 1,4-benzenedicarboxylic acid and Cu_2 clusters to synthesise MOF-101 [128].

A year later, Yaghi’s team synthesized eleven frameworks (MOF-102 to MOF-112) made of PW SBUs (Cu, Zn and Fe) and various dicarboxylates with different angles and organic spacers between two carboxylate linkers [44].

In 2004 Zhang and Xiong’s group synthesized a 3-D network containing both PW dimeric and monomeric copper units [129]. According to the authors, the presence of both copper valences enabled the linker, 2-pyridylacrylic acid (which contains pyridyl and also carboxylate functionalities) to simultaneously coordinate the axial and the equatorial positions of the metal core.

In 2007 Zhou et al. synthesized MOFs based on Cu_2 and triazine-2,4,6-triyltribenzoic acid and investigated their H_2 uptake [130]. Notably, the authors faced a very common problem in MOF synthesis, namely the network catenation, i.e. the interpenetration of two networks.

In 2008 Kitagawa’s research group synthesized a 3-D MOF from $Cu(NO_3)_2$ and bis(4-carboxy-benzyl)amine) ligand [131]. This

multifunctional ligand bears two carboxylate groups and one aliphatic amine group simultaneously coordinating the equatorial and the axial sides of the Cu₂ cores, respectively.

In 2009 Fröba et al. focused on the utilization and improvement of MOFs in the field of hydrogen storage [132]. They connected Cu₂ units by the organosilicon linker 5,5'-(dimethylsilanediyl)-diisophthalate. Four carboxyl functionalities of this linker connect four PW dimetal centers, resulting in a 3-D network with four different pore sizes. Simulation showed preferred adsorption sites on an atomic scale. Fröba affirmed that the incorporation of elements with a higher polarizability than carbon positively influence the hydrogen binding energy.

7. Summary

In the last two decades, many research groups have focused on the synthesis of metal–organic polygons, polyhedra and polymers with paddle-wheel secondary building units, given the fact that the coordination environment of the dimetal units of a PW SBU theoretically allows the ‘construction’ of frameworks. It can be tell that there are just few examples for a real predictable design of a macromolecular or infinite framework structure. So far, in nearly all cases, the PW SBU is formed in situ, and the framework shape is obtained by the organic linker. Yet, although this method led to a plethora of new MOF structures with different metals, there are – to the best of our knowledge –no reports on the prediction of a certain

metal–organic framework structure starting from the pure dimetal unit and a particular organic linker so far.

As a single exception, 2-D polymer networks can straightforwardly be synthesized, since the equatorial linkage of PW units intrinsically leads to 2-D layers. The subsequent stacking of 2-D layers to 3-D MOFs is meanwhile well documented in the literature and became a standard synthesis procedure. In spite of the wide accessibility of molecular PW-‘edges’, -‘corners’ and polyhedrons, there are few approaches for their linkage to larger structures.

Chapter II

Metal Organic Frameworks: a class of versatile materials for different applications.

1. Introduction

Their great specific area makes MOFs good candidates for “classical” applications of MOFs as microporous materials: they make use of their high surface areas, which increase van der Waals interactions needed for uptake of weakly interacting gases, and exploit the tunability of MOF pore dimensions to control relative rates of adsorption and transport through the pores.

However, MOFs have properties that extend their potential range of use far beyond traditional microporous materials. These include: luminosity resulting from conjugated organic linkers; structural flexibility in response to molecular adsorption or changing environmental conditions; charge transfer (ligand-to-metal or metal-to-ligand); high thermal stability relative to many organic polymers; electronic and conducting properties; pH-sensitive stability. As a result, there are now demonstrations of MOFs made for chemical detection (using both optical and mechanical transduction mechanisms), radiation detection, production of ion-conducting membranes, and drug delivery, as well as catalysis (functioning either as the catalyst itself or as supports for catalyst nanoparticles), and both gas- and liquid-phase chemical separations.

2. MOF-Based Separations

One of the most common uses of porous materials is the separation of mixtures of gases or liquids. With applications including purification of O₂ and N₂, removal of volatile organic compounds, and separation of CO₂ from CH₄ in natural gas, these materials play a vital role in many different industries.

Separation relies on two mechanisms: a thermodynamics-driven one, by which one component is selectively adsorbed over others in the mixture, and a kinetics-driven one, by which separation relies on the path the components take through the pores of the material. MOFs, with their high surface area and synthetically tailorable porous structure, are well positioned to make a significant impact in this field.

MOFs have been studied at length for applications in separation, and a recent extensive review catalogues the applications, design principles, and progress in this field [133].

Here we will list some of the most recent advances (Table 2.3) and discuss the use of MOFs in removing toxic and environmentally hazardous gases and the integration of MOFs into membranes, both relatively new areas of study.

MOF	Analytes
Zn-BDC-1,4-diazabicyclo[2.2.2]octane	p-, o-, m-xylene, ethylbenzene
MIL-53(Al)	CH ₄ , CO ₂
Cd-4-amino-3,5-bis(4-pyridyl-3-phenyl)-1,2,4-triazole	Benzene, toluene, p-, o-, m-xylene
MOF-5 (membrane)	H ₂ , O ₂ , CO ₂ , CH ₄ , N ₂
Mg-MOF-74	CO ₂ , CH ₄
HKUST-1	CO ₂ , CH ₄ , N ₂
MIL-53(Cr)	CO ₂ , CH ₄
MIL-96(Al)	C ₂ -diolefins, mono-olefins, and paraffins
Cd-2-amino-1,4-benzenedicarboxylic acid-4,4'-bipyridine	Rhodamine 6G, Brilliant Blue R-250
MIL-101(Cr)	p-, o-, m-xylene, ethylbenzene
MOF-5 MOF-177	CO ₂ , CH ₄ , N ₂ O, N ₂
MOF-5 MOF-monoclinic	p-, o-, m-xylene, ethylbenzene
MIL-53(Al, Cr, Fe) MIL-47(V) MIL-100(Cr) MIL-101(Cr)	H ₂ S
MOF-5 MOF-505 MOF-177 UMCM-150 HKUST-1	benzothiophene/isooctane dibenzothiophene/isooctane dimethyldibenzothiophene/isooctane
MOF-5 IRMOF-3 MOF-74 HKUST-1 MOF-177 IRMOF-62	SO ₂ , NH ₃ , Cl ₂ , tetrahydrothiophene, benzene, dichloromethane, and ethylene oxide
MOF-5/GO composite	NH ₃
ZIF-7 (membrane)	H ₂ , CO ₂
Cu ₃ (BTC) ₂ (membrane)	H ₂ /CO ₂ , H ₂ /NH ₄ , H ₂ /N ₂
Cu-4,4'-(hexafluoroisopropylidene)-bis(benzoic acid)	H ₂ , CH ₄ , N ₂ , CO ₂
ZIF-8 (membrane)	H ₂ , CO ₂ , O ₂ , N ₂ , and CH ₄
MOF-5 (membrane)	H ₂ , CH ₄ , N ₂ , CO ₂
MOF-5 (membrane)	H ₂ , CH ₄ , N ₂ , CO ₂ , SF ₆

Tab. 2.3 Recent reports of MOF-based separations .

2.1 MOFs for Removal of Toxic and Environmentally Hazardous Gases

Exploration of the use of MOFs in removing toxic or environmentally hazardous gases has been confined primarily to CO₂ capture and separation from flue gas [133, 134], with some results concerning the removal of tetrahydrothiophene from fuel reported as well [133].

Most recently, Weireld and coworkers studied the uptake of hydrogen sulfide (H₂S) in MIL-47(V), MIL-53(Al, Cr, Fe), MIL-100(Cr) and MIL-101(Cr). H₂S is a challenging adsorbate due to strong interactions with other porous materials, resulting in adsorbent

decomposition or difficult regeneration. MIL-47(V) and MIL-53(Al, Cr), however, display little degradation and reversible uptake. The MIL-53 materials also exhibit stepwise adsorption, which makes them attractive for pressure swing adsorption separations to purify natural gas [135].

Moreover, Matzger and coworkers investigated the uptake of benzothiophene derivatives from isooctane solutions by MOF-177, MOF-5, UMCM-150, HKUST-1, and MOF-505, and found high levels of adsorption compared to zeolite Na-Y. Pore size played a key role in adsorption levels, with the best interactions found when the pore closely matched the size of the adsorbate [136]. This group continued this work to study the removal of dibenzothiophene and 4,6-dimethyldibenzothiophene from actual diesel fuel, obtaining high levels of adsorption, high selectivity, and feasible regeneration of adsorbent materials [137].

Furthermore, Yaghi and coworkers performed a large-scale study of the adsorption of various harmful gases, including sulfur dioxide, ammonia, chlorine, tetrahydrothiophene, benzene, dichloromethane, and ethylene oxide, by MOF-5, IRMOF-3, MOF-74, MOF-177, HKUST-1, and IRMOF-62. The results indicated that MOF materials are promising adsorbents for harmful chemicals, although more research into their stability and large-scale production will be needed for them to be integrated into industrial processes.

2.2 MOFs for Membrane-Based Separations

Membrane-based technologies are widely applied on an industrial scale to the separation of gases [138]. Membranes rely on a permeability differential between two gases, based on pore size and shape and chemical functionality. As these are more tunable properties in MOFs than in zeolites or other porous materials, such coordination polymers represent a promising new class of materials for the production of separation membranes. Moreover, being both porous and ordered, they can obviate the tradeoff between selectivity and throughput that is often found in traditional polymeric membranes [139].

MOFs can either be integrated into a polymer matrix or grown directly as thin films [140]. As an example, Won et al. reported the first case of impregnating a polymer with a MOF, using a Cu-4,4'-bipyridine in amorphous glassy polysulfone, achieving very high selectivity for H₂/CH₄ mixtures (almost 200 with 5% weight loading) [141].

More recently, Perez et al. added MOF-5 nanocrystals to a Matrimid membrane. While the selectivity for various gas mixtures remained at similar values to the pristine polymer membrane, the permeability of the composite membrane was 120% higher [142].

Also Liu et al. synthesized continuous MOF-5 membranes via standard heating solvothermal synthesis in the presence of α -alumina disks. Experiments to measure the permeation of SF₆, CO₂, N₂, CH₄ and H₂ indicated that these gases exhibit Knudsen diffusion behavior and size-selective permeability [143]. Yoo and Jeong obtained similar

results for MOF-5 continuous membranes grown via microwave rapid seeding followed by solvothermal secondary growth [144].

Also Guo et al. grew films of CuBTC on a 400-mesh copper net, and then tested this composite material for the separation of H₂ from binary mixtures with CO₂, CH₄, and N₂. The MOF membrane provided excellent permeation for H₂ (about $1 \times 10^{-1} \text{ mol} \cdot \text{m}^{-2} \cdot \text{s}^{-1}$) and separation factors of 6–7, which exceed those expected from Knudsen diffusion. The membrane maintained these separation factors for 25 hours and were reused with little loss of function [145].

3. MOF Guest Catalysts

One of the most prolific areas of MOF research is the field of catalysis. MOFs have several advantageous features in this regard. In particular, the inorganic-organic hybrid nature of their structure, coupled with their nanoporosity, provides multiple opportunities to create one or more catalytic sites within pores. Most MOF catalysts rely on the framework metal, but the organic linker can clearly participate as well. Both the linker's chemical functionality and shape (i.e. enantioselectivity) may be catalytically active. Alternatively, the linker may be used as a scaffold to which discrete catalytic complexes can be bound. This synthetic flexibility enables considerable control over pore size and pore environment, allowing selectivity to be tuned more effectively. MOF pores can also serve as hosts for guest molecules or as templates and supports for metal or metal oxide nanoclusters. All of these properties can be modified via chemical

synthesis, which sets MOFs apart from other nanoporous materials such as zeolites and activated carbons.

The topic of MOFs as catalysts was recently reviewed [146, 147], so only some of the most recent MOF guest-based catalysts will be described here (Table 2.4).

As a first example, Fischer and coworkers carried out an early work in the field of MOF guest catalysis by depositing Pd and Cu nanoparticles in MOF-5 via chemical vapor deposition (CVD). The Pd-MOF-5 composite catalyzed cyclooctene hydrogenation, while its Cu variant catalyzed methanol production from synthesis gas [148].

MOF Metal	MOF Linker (Name)	Center of Catalysis	Reaction
Cu	4,4'-bipyridine	Metal	Epoxide alcoholysis
Yb	Succinic acid	Metal	Sulfide oxidation Aldehyde acetalization Hydrosulfurization of thiophene
Zn	BDC (IRMOF-1)	Metal	Cycloaddition of CO ₂ and epoxides
Ni	4,4'-bipyridine BTC	Metal	Hydrogen release from NH ₃ BH ₃
Zn	Tris[2-(4-carboxyphenoxy)ethyl]amine	Metal	Knoevenagel condensation cyanosilylation
Cu	(S)-3-hydroxy-2-(pyridin-4-ylmethylamino)propanoic acid	Metal	Biginelli reaction Asymmetric 1,2-addition of α,β -unsaturated ketones and aldehydes
Yb	Anthraquinone-2,6-disulfonate	Metal	Sulfide oxidation Hydrosulfurization of thiophene
Sc	Squaric acid	Metal	Cyanosilylation and acetalization of carbonyls
Cu	1,2,4,5-benzenetetracarboxylic acid 2,2'-bipyridine	Metal	Oxidation of olefins
Sc Y	1,5-naphthalenedisulfonate 2,6-naphthalenedisulfonate 1,5-naphthalenedisulfonate	Metal	Epoxidation of linalool Oxidation of sulfides
Fe	2,5-di-hydroxy-1,4-benzenedicarboxylic acid	Metal	Phenol hydroxylation
Zn	BDC (IRMOF-1)	Metal	Friedel-Crafts alkylation
Ca	4,4'-(hexafluoroisopopylidene)-bis(benzoic acid)	Metal	Styrene hydrogenation Aldehyde, ketone, alkene hydrosilylation
Cu	4,4'-bipyridine	Metal	Allylic oxidation
Zn Al	BDC (IRMOF-1, MOF-69C) 2-aminoterephthalic acid (IRMOF-3) naphthalene 2,6-dicarboxylic acid (IRMOF-8, MOF-69B) biphenyl-4,4'-dicarboxylic acid (IRMOF-10, MOF-69A) Terephthalic acid (MIL-53(Al))	Metal	Friedel-Crafts alkylation
Cu Ag	4,4'-bipyridine α,ω -alkanedisulfonate	Metal	Ketalization
Zn	BDC 2-aminoterephthalic acid	Linker, Metal	Cycloaddition of CO ₂ and epoxides
Zn	2-aminoterephthalic acid 4,4',4''-benzene-1,3,5-triyltribenzoic acid (UMCM-1-NH ₂)	Linker (Fe catalyst build on linker)	Mukaiyama-aldol reaction
Zn Al	2-aminoterephthalic acid (IRMOF-3) 2-aminoterephthalic acid (MIL-53(Al)-NH ₂)	Linker (-NH ₂ functionality)	Knoevenagel condensation
Zn	1,2,4,5-tetrakis(4-carboxyphenyl)benzene (5,15-dipyridyl-10,20-bis(pentafluorophenyl))porphyrin	Linker (Zn-porphyrin)	Acyl-transfer
Zn	2-aminoterephthalic acid 4,4',4''-benzene-1,3,5-triyltribenzoic acid (UMCM-1-NH ₂)	Linker (Fe, In, Cu catalysts build on linker)	Regioselective epoxide ring opening
Cu	2,2'-bipyridine-4,4'-dicarboxylate	Linker (PdCl ₂ catalyst built on linker)	Suzuki-Miyaura coupling
Zn	BDC 2-aminoterephthalic acid	Linker (Pd particles immobilized on the linker)	CO oxidation
Zn	2-aminoterephthalic acid (IRMOF-3)	Linker (Au salicylideneimine catalyst built on linker)	Hydrogenation
Zn	2-methylimidazole (ZIF-8)	Au nanoparticle guest	CO oxidation
Cu	BTC (HKUST-1)	Keggin polyoxometalate guests	Acid hydrolysis
Tb	Triazine-1,3,5-tribenzoate	Ni nanoparticle guest	Hydrogenolysis hydrogenation
Zn Al Cu	Terephthalic acid (IRMOF-1) Terephthalic acid (MIL-53) 1,3,5-benzenetricarboxylate (HKUST-1) Pyrazine-2,3-dicarboxylate Pyrazine (CPL-1) Pyrazine-2,3-dicarboxylate 4,4'-bipyridine (CPL-2)	Au nanoparticles deposited on the surface of the MOF	Benzyl alcohol oxidation
Zn	BDC (IRMOF-1)	Cu and Cu/ZnO nanoparticle guests	Methanol synthesis from CO/CO ₂ /H ₂
Zn	1,3,5-benzenetribenzoic acid (MOF-177)	Pt nanoparticle guest	Oxidation of alcohols
Zn	BDC (IRMOF-1)	Ru nanoparticle guests	Alcohol Oxidation
Cr	BDC (MIL-101)	Polyoxometalate guests	Alkene Oxidation
Cr	BDC (MIL-101)	Polyoxometalate guests	Knoevenagel condensation Esterification Dimethyl ether synthesis

Tab. 2.4 Reports of MOF based catalysts

During the intervening years, several investigators explored MOF-5 as a host for nanoparticle catalysts. Fischer and coworkers also tested Ru-loaded MOF-5 as a catalyst for benzene hydrogenation and benzyl alcohol oxidation, but found low levels of conversion [149]. The same research group also studied Cu and ZnO loading in MOF-5 and found that the Cu-MOF-5 composite catalyzed methanol synthesis, a surprising result since pure copper shows almost no catalytic activity in the absence of ZnO. When ZnO nanoparticles are also added, the MOF shows even higher activity, although this effect quickly degrades [150].

Finally, Ishida et al. deposited gold nanoclusters onto various MOFs, including MOF-5, MIL-53 (Al), CPL-1, CPL-2, and CuBTC, via solid grinding with Me₃Au(acac) (gold methyl acetylacetonate). These materials catalyze the oxidation of 1-phenylethanol, with the best yield (79%) obtained for MOF-5 [151].

In addition to MOF-5, other MOFs have been used as templates for nanoparticles, including MOF-177. In fact, Proch et al. loaded MOF-177 with Pt nanoparticles via gas phase infiltration of a Pt complex followed by reduction. This material efficiently catalyzes the oxidation of benzylic and allylic alcohols, though the catalyst could not be recycled due to stability issues [152].

Moreover, Jiang et al. deposited Au nanoparticles in ZIF-8 via grinding with a volatile organogold complex. These materials exhibit catalytic activity in the oxidation of CO, but only after activation at 300°C, and they showed reproducible activity on subsequent runs [153].

Furthermore, Park et al. loaded a mesoporous Tb-triazine-1,3,5-tribenzoate MOF with Ni nanoparticles. This material catalyzes the hydrogenation of styrene and the reduction of nitrobenzene to aniline with activity similar to Raney Ni [154].

In addition to noble metal nanoparticles, Keggin polyoxometalates (POMs) have also been explored as catalytic MOF guests. As an example, Maksimchuk et al. reported the adsorption of Ti- and Co-POMs into MIL-101 (Cr) [155].

More recently, Kapteijn and coworkers synthesized MIL-101(Cr) MOFs with varying levels of encapsulated $H_3PW_{12}O_{40}$ POMs. For comparison, they also added these POMs to the MOF via impregnation after synthesis. The encapsulated catalysts displayed very high activity and reusability in the Knoevenagel [156] condensation, esterification of n-butanol, and in the dehydration of methanol to dimethyl ether, while the impregnated catalyst demonstrated lower activity, an effect attributed to the better dispersion of the POM in the encapsulated material [157].

4. MOFs as Drug Delivery Systems

With their tunable host-guest properties and facile modification via chemical synthesis, MOFs represent a very attractive platform as drug delivery systems. An early work in this field was carried out by Horcajada and coworkers who investigated the loading of ibuprofen into MIL-100(Cr) and MIL-101(Cr) and found that both have high uptake (0.35 g/g and 1.38 g/g respectively) and 3–6 day release times

in simulated body fluid [158]. This proof-of-concept work branched out to several other studies in the last few years.

As an example, McKinlay et al. found that Co- and Ni-2,5-dihydroxyterephthalate MOFs are able to bind NO at open coordination sites in levels higher than currently employed zeolites. These materials can store 6–7 mmol/g of NO for several months, but on contact with PBS buffer they release the gas in about 10 minutes. Samples of loaded material placed in close proximity to porcine coronary arteries resulted in complete relaxation [159].

Covalent NO storage is also reported using amine-functionalized IRMOF-3 and UMCM-1-NH₃. Here, the NO reacts with the amine to form diazeniumdiolate groups. Decomposition of the framework in phosphate buffer results in release of NO gas, with values of 0.51 mmol/g for IRMOF-3 and 0.10 mmol/g for UMCM-1-NH₃.

Afterwards, Rosi and coworkers demonstrated the storage and the release of the antiarrhythmia drug Procainamide from an anionic pillared zinc-adeninate MOF in PBS buffer. When the drug-loaded MOF was introduced into deionized water, drug release was significantly reduced, suggesting that cation exchange is crucial to this process [160].

MOFs have also been used as platforms to build multifunctional nanoparticles. As an example, polymers functionalized with fluorescent contrast agents, targeting ligands, and therapeutic agents have been grafted onto a Gd-MOF nanoparticle core, which itself works as an MRI contrast agent [161].

A large portion of the recent work in the field of drug delivery by MOFs is focused on MIL compounds [162-164]. These studies underline the promise of MOFs in the drug delivery field and indicate that MOFs are ready for a more extensive biological testing.

1. Electronic and Optical Applications

With a diversity of topologies and linkers, MOFs represent a class of materials with unique optical and electronic properties. Possible applications in this particular area of research include electron and proton conducting materials, light emitting diode (LED) materials, nonlinear optical devices and sensors.

5.1. Electronic Applications of MOFs

Obtaining electronic or ionic conductivity in MOFs would expand the range of potential applications including electronic devices, electrical storage, and power generation. Proton conductivity in 1D and 2D coordination polymers has been explored previously, and this class of materials is of interest as components in proton exchange membrane and direct methanol fuel cells.

In 2009 Kitagawa and coworkers synthesized a Zn-oxalate-adipic acid MOF which contains NH_4^+ ions and water and carboxylate groups in its honeycomb-shaped pores. This material exhibits 8×10^{-3} S/cm proton conduction at 25 °C and 98% relative humidity, a level of conductivity comparable to the Nafion polymer. The activation energy

of this MOF is found to be 0.63 eV, substantially higher than other hydrated proton conductors, which suggests that its high conductivity is the result of conduction vehicles other than water, presumably the NH_4^+ and free carboxylate groups [165].

Electron conduction is observed in MOFs in a limited number of cases. Numerous coordination polymers have been examined for this property and in the last few years several reports of porous 3D MOFs with electronic conductivity appeared. As an example, Kitagawa and coworkers report a Cu-Cu-2,3-pyrazinedithiolate MOF with 6×10^{-4} S/cm conductivity at 300 K [166]. This conductivity is attributed to a donor-acceptor relationship between the Cu^I connector unit and the Cu^{III} -2,3-pyrazinedithiolate complex.

5.2 Optical Applications of MOFs

In the last few years researchers began exploring the use of MOFs in light-emitting devices. As an example, Gandara et al. synthesized a series of (lanthanide)-4,4'-(hexafluoroisopropylidene)bis(benzoic acid) MOFs, including Y, La, Ce, Pr, Nd, Sm, Eu, Gd, Tb, Dy, Ho, Er, and Yb as the selected lanthanides. The Eu and Tb variants are very efficient red and green emitters, respectively, indicating possible use in LED applications. The Gd-MOF emits broadly in the visible region, making it a candidate for white LEDs [167].

Moreover, Wang et al. reported on a Ag-4-cyanobenzoate MOF with broad emission in the visible region. When irradiated at 330 nm, the MOF emits strongly at 566 nm to give yellow light. However, when

irradiated at 350 nm, the emission broadens considerably to afford light that closely matches the Commission Internationale de l'Eclairage chromaticity coordinates for white light [168]. Infrared-emitting MOFs are also known. As an example, Rosi, Petoud and coworkers designed Yb-4,4'-[(2,5-Dimethoxy-1,4-phenylene)di-2,1-ethenediy1]bis-benzoate (PVDC) MOFs that have near-infrared (NIR) emission with excitation in the visible spectrum [169].

6. Hydrogen storage in Metal Organic Frameworks

6.1 Excess versus total uptake

Most articles dealing with hydrogen storage in metal–organic frameworks report the H₂ uptake capacity at a pressure of ca. 1 bar, where excess and total adsorption values are nearly identical. However, since pressures of up to 100 bar are deemed safe for automotive applications, measurements at higher pressures, where these two quantities can differ considerably, have become common. Excess adsorption refers to the amount of H₂ taken up beyond what would be contained, under identical conditions, within a free volume equivalent to the total pore volume of the sample. Thus, this quantity approximates the amount of H₂ adsorbed on the surfaces within the material.

Since the efficiency of packing and compressing gas molecules within the boundaries of the pores of a microporous solid is less than that achieved in a free volume, the excess adsorption will reach a

maximum at some pressure (typically 20–40 bar) and will then decrease. Despite such decrease, measurements at pressures above the maximum in excess adsorption are of value for assessing the compressibility of H₂ within the material and evaluating the total uptake.

The total uptake, sometimes referred to as the absolute uptake, corresponds to the amount of hydrogen contained within the boundaries formed by the faces of the metal–organic framework crystals. This quantity therefore includes both surface-adsorbed H₂ and the H₂ gas compressed within the framework pores.

To calculate the total uptake from the excess adsorption, it is necessary to know precisely the density of the framework skeleton or the empty volume of the adsorbent, as typically measured using helium gas. Importantly, knowledge of the total uptake enables determination of the volumetric storage density within the compound, which is one of the main considerations in selecting an adsorbent for hydrogen storage.

It is important to note, however, that this fundamental property of the material does not take into account the efficiency of packing the crystals together in a container, as must be considered in determining the overall density for a storage system.

When calculating the H₂ uptake, either excess or total, in units of wt%, it is important to recognize that it is equal to $(\text{mass H}_2)/(\text{mass sample} + \text{mass H}_2)$.

Unfortunately, some researchers neglect the second term in the denominator, leading to complications in comparing uptake capacities for different materials [170].

6.2.Design principles for an optimal H₂ adsorbent

There have been numerous computational studies that attempt to model H₂ adsorption data in metal organic frameworks [171-182].

In particular, Zn₄O(BDC)₃ (BDC=1,4-benzenedicarboxylate;) and its isoreticulated congeners have received much attention from theorists.

In most cases, computed isotherms and binding energy values agree reasonably well with the experimental results, although one should be careful to employ an accurate intermolecular H₂ potential energy function [183] and to ensure that the comparison data are for an authentic sample [184]. These studies indicate the presence of just van der Waals-type interactions between H₂ and most frameworks, consistent with the approximate correlation of H₂ uptake at 77 K with surface area and the very low storage capacities observed at 298 K. Indeed, with just two electrons, H₂ forms extremely weak van der Waals bonds, resulting in isosteric heats of adsorption that are typically in the range 4–7 kJ mol⁻¹. Partial charges, either positive or negative, on the metal–organic framework surface can provide a means of strengthening the binding of H₂ through dipole–induced dipole interactions [171, 185]. Only a few computational studies have dealt with frameworks exhibiting such heterogeneous surface

potentials. An added complication in performing calculations on frameworks bearing open transition metal coordination sites stems from the fact that these metals sometimes have open-shell electron configurations, for which assignment of the spin state can be difficult.

For instance, the relatively strong metal–H₂ interactions within Mn₃[(Mn₄Cl)₃(BTT)₈]₂ (H₃BTT=benzene-1,3,5-tris(1Htetrazole)), which exhibits an isosteric heat of adsorption of 10.1 kJ mol⁻¹ at zero coverage [186], have been variously attributed to a spin-state change upon binding [187] or to a classical Coulombic attraction [188].

Understanding metal–H₂ interactions of this type is instrumental to the design of improved storage materials, and the development of computational approaches that can reliably handle interactions with open-shell metal ions would result in an important step forward.

Clearly, increasing the H₂ binding energy within metal–organic frameworks is the most important challenge for creating hydrogen adsorbents that operate at 298 K. Recent work has addressed this issue and predicted optimal parameters for hydrogen storage in microporous materials.

First, Langmuir isotherms were employed to derive equations that allow the calculation of an optimal adsorption enthalpy, ΔH_{opt} , for a given adsorption temperature [189]. According to this model, which can be reduced to the empirical equation $\Delta H_{\text{opt}}/RT=6.1$, a microporous adsorbent operating between 1.5 and 100 bar at 298 K would ideally have an adsorption enthalpy of 13.6 kJ mol⁻¹ over the entire H₂ uptake curve. Similarly, the model allows one to calculate the optimal

operating temperature for an adsorbent with a given enthalpy of adsorption. For instance, it predicts that a typical metal–organic framework with an average adsorption enthalpy of 6 kJ mol^{-1} would work optimally at a temperature of 131 K.

The aforementioned model has recently been adjusted through introduction of an entropy–enthalpy correlation term [190]. Whereas ΔS_{ads} had previously been assumed to be constant and equal to $-8R$, the new model argues that Langmuir adsorption is in fact governed by a positive correlation between entropy and enthalpy.

Taking this empirical correlation into account suggests that a material operating between 1.5 and 30 bar at 298 K requires a ΔH_{opt} of 22–25 kJ mol^{-1} , which is significantly higher than that obtained with the previous model. Thus, for pressures ranging up to 100 bar, one would like to create new metal–organic frameworks featuring surfaces with a ΔH_{opt} of ca. 20 kJ mol^{-1} , representing an enhancement by a factor of 3 or 4 over simple physisorption.

As expected, in a microporous material where physisorption and weak van der Waals forces dominate the adsorption picture, the storage density is also greatly dependent on the size of the pore. Calculations on idealized homogeneous materials, such as graphitic carbons and carbon nanotubes, predict that microporous materials with 7 Å-wide pores will exhibit maximal H_2 uptake at room temperature. Actually, a 7 Å-wide slit-shaped pore maximizes the van der Waals potential by exactly allowing one layer of H_2 molecules to adsorb on opposing surfaces, with no space left in between. Notably, at 77 K, a layer sandwiched in between these two opposing surface monolayers

becomes favorable, and the ideal pore size for maximum volumetric H₂ uptake at 100 bar is predicted to be 10 Å, regardless of whether a slit shape or cylindrical pore shape is considered [191].

Finally, an ideal hydrogen storage material would be stable to any potential impurities that might commonly be present in H₂ gas (e.g., H₂S, carbon–sulfur compounds, CO, CO₂, N₂, H₂O, and hydrocarbons), and to accidental exposure to the atmosphere. Indeed, metal–organic frameworks exhibiting some of the best performance characteristics, such as Zn₄O(BDC)₃ and Mn₃[(Mn₄Cl)₃(BTT)₈]₂, are known to decompose in air [184, 186, 192, 193], which would need to be accounted for in the design of a storage system.

However, by producing frameworks featuring strong metal–ligand bonds, as occurs for example in metal–imidazoles [194–196], –triazoles [197–201], and –pyrazoles [202], materials exhibiting improved chemical stability can be obtained.

6.3 Methods for increasing the H₂ adsorption enthalpy

6.3.1 Exposed metal sites

Perhaps the most effective way of increasing the H₂ adsorption enthalpy in metal–organic frameworks is through the introduction of open metal coordination sites on their surfaces. It is well known that H₂ can bind to metals in molecular systems, where metal–H₂ bond dissociation energies can be as high as 80–90 kJ mol⁻¹ [203]. These values are clearly too large for storage purposes, and would result in both a tremendous release of heat upon loading with H₂ and a

requirement for significant heat input to liberate the bound H₂ when needed. To achieve the desired binding energy of ca. 20 kJ mol⁻¹, one most likely need to avoid the favorable orbital interactions that lead to such strong metal–H₂ bonds and move into the regime of simple charge-induced dipole interactions.

This situation is exemplified by the interaction between the Li⁺ cation and H₂ in the gas phase, which has been measured, albeit with a large potential error, to have a binding energy of 27 kJ mol⁻¹ [204]. Unfortunately, when Li⁺ is placed on a surface within a porous framework much of its charge is quenched, leading to significantly weaker H₂ binding. Indeed, the highest isosteric heat of H₂ adsorption yet observed for such a system is just 7.9 kJ mol⁻¹ in Li₂Zn₃[Fe(CN)₆]₂·2H₂O [205]. To counter this effect, a more highly-charged metal cation, such as Mg²⁺, M²⁺ (M=transition metal), or even Al³⁺, may be required. The challenge is then to develop synthetic methods for generating high concentrations of exposed metal ions on the surfaces within metal–organic frameworks. These methods, together with the properties of the resulting materials, have been recently reviewed in detail [206], and will therefore receive only brief attention here.

The primary method utilized thus far involves thermally-assisted evacuation of solvent molecules bound to metals serving as framework nodes, as for example reported for exposing Cu²⁺ coordination sites within Cu₃(BTC)₂ [192, 207] and Mn²⁺ coordination sites within Mn₃[(Mn₄Cl)₃(BTT)₈]₂ [186]. Here, one is generally fighting against framework collapse, making it sometimes beneficial to exchange the bound solvent molecules for more volatile species,

such as methanol. Alternatively, photolysis can sometimes be used to facilitate substitution of a terminal ligand for H₂, as demonstrated recently for Zn₄O[(BDC)Cr(CO)₃]₃ [208]; however, it is important to recognize the poor efficiency of photolyzing solids. For rare cases of anionic frameworks, exchange of the guest metal cation can affect hydrogen uptake [193, 205, 209].

6.3.2 Catenation/interpenetration

Very large pores within a metal–organic framework are ultimately detrimental to hydrogen storage, because H₂ molecules near the center of the pore are unlikely to experience any attraction from the surface of the pore walls. Accordingly, as will be discussed later, such low-density framework solids will tend to have low volumetric H₂ uptake capacities.

Indeed, it is clear that a large micropore volume composed of small voids is more desirable for an efficient storage material [210]. Such a material would adsorb H₂ more strongly, but would still exhibit a high surface area, which has been shown to correlate almost linearly with the overall H₂ uptake for homogeneous, physisorption-based systems [211]. One could conceivably reduce the number of large voids in a given structure via framework interpenetration. Synthetically, however, it is extremely difficult to control interpenetration, and only one example exists wherein catenated and non-catenated forms of the same framework were directly compared for H₂ storage. However, catenation can sometimes lend a material enhanced thermal stability,

reducing the degree of framework collapse during desolvation [212]. Along these lines, it has been argued recently that catenation is detrimental for the overall uptake [174].

Calculations suggest that the amount of H₂ adsorbed correlates with the heat of adsorption only at low loadings, and that surface area and total free volume become more important at intermediate and high loadings, respectively. It has been argued that the increase in binding energy associated with catenation will not offset the loss of free volume, which negatively affects the total H₂ uptake in a given material.

6.4 Spillover

Hydrogen spillover is a well-established phenomenon in surface science, involving the dissociation of H₂ into H• on a metal surface and subsequent migration of these atoms onto materials such as alumina [213-218]. This reaction is reversible, with hydrogen atoms spontaneously recombining to afford the molecular gas.

Spillover from a nearby metal site and migration of those hydrogen atoms into the pores of frameworks could enhance the hydrogen storage capacity, provided that no irreversible hydrogenation chemistry occurs and that the adsorbate–framework interaction and packing density of H• are greater than those relative to H₂ [219-220]. While researches on spillover have generated some of the most encouraging recent results for room-temperature hydrogen storage, many fundamental questions remain to be addressed.

Understanding the precise form in which hydrogen is stored in these systems may provide the key for improving desorption kinetics and then the recyclability of the sorbent. In fact, if the storage mechanism does involve spillover, then synthetic chemistry can perhaps supply materials in which well-defined metal nanocrystals are directly integrated within metal–organic frameworks. The possibilities of achieving a spillover effect with low-cost metals, such as nickel, and very small metal clusters or even individual metal centers also remain to be explored.

6.5 Metal Organic Frameworks exhibiting a high H₂ uptake

One of the first metal–organic frameworks investigated for hydrogen storage was the cubic carboxylate-based framework $Zn_4O(BDC)_3$ [221]. This compound has been widely studied since then, and turns out to be the best cryogenic storage material currently known. Early measurements performed at 77 K resulted in an excess gravimetric uptake of 1.3 wt% at 1 bar [222] and 5.1 wt% at 50 bar [223].

Interestingly, the gas storage properties obtained for $Zn_4O(BDC)_3$ were found to depend very much on the methods utilized in its preparation and activation, with Langmuir surface areas ranging between 1010 and 4400 m² g⁻¹ and H₂ uptake capacity varying accordingly [184,196, 221-230]. These variations can be attributed to incomplete evacuation of the pores and/or partial decomposition of the framework upon exposure to air[184].

With complete activation and protection of the sample from air and water vapor, $\text{Zn}_4\text{O}(\text{BDC})_3$ was observed to exhibit a record excess H_2 uptake of 7.1 wt% at 77 K and 40 bar [184]. At 100 bar, a total uptake of 10.0 wt% is attained, corresponding to a record volumetric storage density of 66 g L^{-1} . Remarkably, this value is near the density of 71 g L^{-1} observed for liquid hydrogen at 20.4 K and 1 bar [231]. In addition, it was demonstrated that hydrogen can be loaded into a cold sample of the compound within 2 min, and can be completely desorbed and re-adsorbed for at least 24 cycles without loss of capacity [184].

Inspired by the performance of compounds such as $\text{Zn}_4\text{O}(\text{BDC})_3$, researchers have thus far reported hydrogen storage data for over 150 other microporous metal–organic frameworks (see Table 2.5) [232, 233] However, most efforts to date have focused on attaining a high gravimetric uptake, which, importantly, can be at direct odds with achieving a high volumetric storage density. This is because materials with a very high surface area also tend to exhibit an increased micropore volume and, consequently, an inherently low bulk density.

Compound ^a	Surface area/m ² g ⁻¹		Pore vol./cm ³	Conditions		Hydrogen storage ^b		Q _{H₂} /kJ mol ⁻¹
	BET	Langmuir		P/bar	T/K	Excess/wt%	Vol./g L ⁻¹	
Li _{3.2} Mn _{1.4} (Mn ₂ Cl) ₃ (BTT) ₈ ·0.4LiCl	1904	2057	0.043	1.2	77	2.06		8.9
α-Mg ₂ (HCO ₂) ₆	150			1	77	0.6		
Mg ₂ (NDC) ₃		520		1	77	0.78		
TUDMOF-2	190			1.12	77	0.46		9.5
Al(OH)(BDC)	1100	1590	0.59	16	77	3.8	37	
Al ₁₂ O(OH) ₁₈ (H ₂ O) ₃ (Al ₂ (OH) ₄)(BTC) ₆				3	77	1.91 ^c		
Sc(BDC) ₃	721		0.332	1	77	1.5		
Cr(OH)(BDC)	1100	1500	0.56	16	77	3.1	1.04	6.3
Cr ₃ OF(BTC) ₂		2700	1	73.3	298	0.15	23.0	
Cr ₃ OF(mic) _{1.5}		42	0.12	90	77	3.28		6
Cr ₃ OF(BDC) ₃		5500	1.9	35	77	1	1.84	10
Mn(HCO ₂) ₂				80	77	6.1	26.1	
Mn(NDC)	297 ^d			1	77	0.9		
Mn ₂ (Mn ₂ Cl) ₃ (ptc-3z) ₈ ·2	191		0.068	1	77	0.57		
Mn ₂ (Mn ₂ Cl) ₃ (ptc-3z) ₈ ·2	1580	1700		25 (80)	77	3.7 (4.5)		10.1
Mn ₂ (Mn ₂ Cl) ₃ (BTT) ₈ ·2	2100			1.2	77	2.2	43	
Mn ₂ (Mn ₂ Cl) ₃ (BTT) ₈ ·2				90	77	5.1 (6.9)	(60)	
Mn ₂ (Mn ₂ Cl) ₃ (BTT) ₈ ·2				90	298	0.94	7.9	9.9
Mn ₂ (Mn ₂ Cl) ₃ (BTT) ₈ ·2	1911	2072		1.2	77	2.00		
Fe ₃ (OH)(pbpc) ₃	1200			1	77	1.6		
Fe ₃ O(urbc) ₃		635		20	77	3.05	33.1	
Fe ₃ (Mn ₂ Cl) ₃ (BTT) ₈ ·2	2033	2201		1	77	0.9		
Fe ₂ O ₃ (BTB) ₃	1121	1835	0.69	1.2	77	2.21		10.2
Co(BDP)		2670	0.93	1	77	2.1		
Co(HBTC)(4,4'-bipy)	887			30	77	3.1		
Co(NDC)(bpy)		115		1	77	2.05		
Co(ox)(bpy)			0.10	1	298	0.96		
Co ₂ (6-mna) ₂	420		0.17	1	77	0.72		
Co ₂ (BDC) ₂ (dabco)	1595	2120	0.77	1	77	0.10		
Co ₃ (2,4-pdc) ₂ (OH) ₂				10	298	0.66		
Co ₃ (BDC) ₃ (dabco)	630		0.26	44.2	77	4.11		
Co ₃ (bpd) ₃ (bpy)	360	538	0.2	100	293	0.32		
Co ₃ (bpd) ₃ (bpy)	922		0.38	1	77	1.60	51.2	6.9
Co ₃ (Mn ₂ Cl) ₃ (BTT) ₈ ·1.7CoCl ₂	2096	2268		1	77	1.94		10.5
Co ₃ (NDC) ₃ (dabco)	1502	2293	0.82	1	77	2.45	29.8	
H ₂ Co ₂ O(urb) ₃ ·3		1355	0.51	17.2	298	0.89	10.8	10.1
Ni ₂ (Ni ₂ (OH)(sp) ₂)	743			1	77	1.53		10.4
Ni(cyclam)(bpyde)		817	0.37 ^e	1	77	1.1		
Ni(dhrp) ₂		1083	0.41	70	77	1.8		
Ni(HBTC)(4,4'-bipy)				1	77	3.42		
Ni(ox)(bpy)	1590			1	298	0.3		
Ni ₂ (ate)				1	77	1.20		
				1	77	0.16		
				1	77	0.6		

Tab.2.5 Surface area, pore volume, hydrogen storage properties under specific conditions for metal–organic and metal–cyanide frameworks[7].

Compound ^a	Surface area/m ² g ⁻¹		Pore vol./cm ³	Conditions		Hydrogen storage ^b		Q _{st} /kJ mol ⁻¹
	BET	Langmuir		P/bar	T/K	Excess/wt%	Vol./g L ⁻¹	
Ni ₂ (bpy) ₃ (NO ₃) ₄			0.181		1	77	0.987	
Ni ₂ (bpy) ₃ (NO ₃) ₄			0.149		1	77	0.653	
Ni _{2.75} Mn _{0.25} (Mn ₄ Cl) ₃ (BTT) ₈ l ₂	2110	2282			1.2	77	2.29	9.1
Ni ₃ (OH)(pbpc) ₃	1553				1	77	1.99	
					20	77	4.15	43.9
Ni ₃ O(tatb) ₂		225			1	77	0.63	
Cu ₂ (BDT)	200				1	77	0.66	
Cu ₂ (bpy)(CF ₃ SO ₃) ₂					1	40	1.4	
HCCu ₂ (Cu ₄ Cl) ₃ (BTT) ₈ l ₂ ·3.5HCl	1710	1770			1.2	77	2.42	10
					90	77	3.7	
					80	298	0.46	
Cu ₂ (dcecp)(NO ₃)	268		0.113		1	77	1.34	6.1
					20	77	1.91	
Cu ₂ (fum)(bpe) _{0.5}					1	77	0.8	
Cu ₂ (2-pymo) ₂	350				1.2	77	0.86	13
Cu ₂ (F-pymo) ₂					1.2	77	0.56	10
Cu ₂ (trfipbb)(t ₂ hfpbb) _{0.5}					48	298	1	14.7
					1	77	0.23	
					1	77	2.4	20.4
Cu ₂ (C ₂ -mdip)	1577	1962	0.73		1	77	1.2	
Cu ₂ (C ₂ -teppda)		504			1	77	1.4	
Cu ₂ (D ₂ -teppda)		626			1	77	1.4	
Cu ₂ (tepedep)		733			1	77	0.8	
Cu ₂ (abtc)		2850	0.89		40-110	77	4.71	53
			1		50	77	2.84	
					1	77	5.22	
Cu ₂ (abtc)(DMF) ₂		1260	0.48		1	77	1.83	
Cu ₂ (aobic)	1407	1779	0.67		1	77	2.34	
					3.5	30	6.84	6.8
					45	300	0.25	18
					1	77	1.8	52.5
Cu ₂ (BDC) ₂ (dabco)	1461	1703	0.63		33.7	77	2.7	
	1300				100	293	0.42	
					70	77	1.68	5.31
Cu ₂ (bpmde) ₂ (bpy)		2910	1.05		0.92	77	4.87	15.4
					1	77	2.47	
Cu ₂ (bptc)	1670	1830	0.63		1	77	2.59	38.9
			0.68		1	77	4.02	37.3
Cu ₂ (qptc)			1.14		20	77	2.24	41.1
	2932				1	77	6.07	
Cu ₂ (sbtc)	1931	2442	0.91		20	77	2.55	19.1
					1	77	7.89	59.1
					3.5	30	5.23	39.2
Cu ₂ (tpic)	2247		0.89		45	77	2.52	43.6
					1	77	6.06	
Cu ₂ (bhtc) ₂	2300	3100	1		20	77	2.1	7.3
					1	77	2.1	

Tab.2.5 (continued)

Tab.2.5 (continued)

Compound ^a	Surface area/m ² g ⁻¹		Pore vol./cm ³	Conditions		Hydrogen storage ^b		Q _{st} /kJ mol ⁻¹
	BET	Langmuir		P/bar	T/K	Excess/wt%	Vol./g L ⁻¹	
Cu ₃ (BTC) ₂	1239		0.62	1	77	2.18	213 ^c	6.1
	1154	1958		50	77	3.6		4.5
	1507	2175	0.75	65	298	0.35		
			0.4	200	200	1		
				1	77	2.48		6.8
				1	77	1.44		6-7
				1	77	2.27		
				10	77	3.6	31.6	
				77	77	3.3	29	
	1944	2260		1.2	77	2.02		8.5
Cu ₃ (Cu _{2.9} Mn _{1.1} Cl) ₃ (BTT) ₈ z ₂ CuCl ₂	1695	1778		1	77	1.9		
Cu ₃ (tatb) ₂ (catenated)	3800			1	77	1.9		
Cu ₃ (tatb) ₂ (non-catenated)	2700		1.045	1	77	1.35		
Cu ₃ (Cu ₄ Cl) ₃ (pb-3tz) ₈ z ₂ 11CuCl ₂	1120	1200		30	77	2.8		
Cu ₄ (TTPM) ₂ ·0.7CuCl ₂	2506	2745		1	77	2.8		8.4
				20 (70)	77	4.1 (5.6)	(41)	
Cu ₄ (C ₇ -mdip) ₂ (C ₂ v-mdip)	1943	2425	0.94	1	77	3.05	23.2	9.5
Cu ₆ O(tz) ₃ (NO ₃)	3223			1	77	2.4		
Zn(abdc)(bpe) _{0.5}	100 ^d			1	77	0.62		
Zn(BDC)(bpy) _{0.5}	946			1	77	0.8		
Zn(MeIM) ₂	1630	1810	0.64	1	77	1.27		
				55	77	3.01		
				30	77	1.3		4.5
				60	77	3.3		
				298	298	0.13		
Zn(NDC)(bpe) _{0.5}	303		0.2	65	298	0.3	18	
Zn(PhIM) ₂	1676		0.58	1	77	1.35		
Zn(tbip)	256			1	77	0.75		
Zn ₂ (abc)(DMF) ₂	1460		0.53	1	77	2.07		6.7
				50	77	3.70		
Zn ₂ (BDC)(mbdc)(dabco)	1100	1670	0.59	1	77	2.08		
Zn ₂ (BDC) ₂ (dabco)	1264			1	77	1.92		
	1165	1488		83.2	77	3.17		
	313	424	0.15	4	77	1.1		
Zn ₂ (bpytc)	1370 ^d			1	77	2.2		8.1
Zn ₂ (btatb)	796 ^d			1	77	1.2		7.4
Zn ₂ (btatb)(DMF) ₂	709 ^d			1	77	1.24		
Zn ₂ (btatb)(Py)	370 ^d			1	77	0.59		
Zn ₂ (btatb)(MePy)	309 ^d			1	77	0.57		
Zn ₂ (btatb)(EIPy)	473 ^d			1	77	1.04		
Zn ₂ (btatb)(ViPy)	388 ^d			1	77	0.57		
Zn ₂ (btatb)(CF ₃ Py)				1	77	1.28		7.85
Zn ₂ (cnc) ₂ (dtp)	342		0.19	1	77	1.75		8.3
Zn ₂ (dtp)	783		0.39	1	77	2.21		
	950	1072		26.1	77	2.8	27.6	8.8
MOF-74, CPO-27-Zn	870			30	77	2.8		
	1000	1450	0.52	1	77	1.7		
Zn ₂ (NDC) ₂ (dabco)	252 ^d			1	77	0.2		
Zn ₂ (NDC) ₂ (dIPyNI)	252 ^d			1	77	0.2		
Zn ₂ (cpedp)	1070	1610	0.57	1	77	1.78		
Zn ₂ (tbdcb) ₂ (dabco)				1	77			

Compound ^a	Surface area/m ² g ⁻¹		Pore vol./cm ³	Conditions		Hydrogen storage ^b		Q _{st} /kJ mol ⁻¹
	BET	Langmuir		P/bar	T/K	Excess/wt%	Vol./g L ⁻¹	
Zn ₃ (tmbdc) ₂ (bpy)	1120	1740	0.62	1	77	1.68		
Zn ₃ (tmbdc) ₂ (diabco)	920	1400	0.5	1	77	1.85		12.3
Zn ₃ (BDC) ₃ (Cu(pyen))			0.26 ^c	1	77	0.66		8.7
Zn ₃ (BDT) ₃	640			1.17	77	1.46		7.1
Zn ₃ (bpdca) ₃ (bpy)	792		0.33	1	77	1.74		7
Zn ₃ (OH)(cdcd) _{2,5}	152	1100		1	77	2.1		
Zn ₃ (tattb) ₂ (HCO ₂) ₂	1927	2079		1	77	1.3		9.6
Zn ₃ [(Zn ₆ (Mn ₃ (Cl) ₃ (BTT)) ₃] ₂ ·2ZnCl ₂	362			1.2	77	2.10		
Zn ₄ (trz) ₄ (1,4-ndc) ₂	584	150		1	77	0.84		
Zn ₄ (trz) ₄ (NDC) ₂		3840	0.1	1	77	1.11		
Zn ₄ O(adc) ₃	2296			1	77	0.41		
Zn ₄ O(BDC) ₃				50	298	4.7		3.8
				65	200	0.28		
				60	200	0.9		
				48	298	1.65	9.9	
				1	77	1.32		
				45.4	77	4.95	30.8	4.1
				30	77	4.3		
				60	298	0.45		
				67	298	0.2	1.19	
				10	77	1.6	9.49	
				10	77	1.15		
			1.18	1	77	7.1	42.1	
				40	77	10.0	66	
				100	77	10.0		
				100	298	0.57		4.8
				1	77	1.32		
				30	77	4.3	25.5	
				1	77	4.5		
				1	77	2.0		
				1	77	2.1		
				1	77	1.15		5.3
IRMOF-9	1904	2613	0.9	1	77	1.15		
IRMOF-2	1722	2544	0.88	1	77	1.5		
MOF-177	4526			1	77	1.23	32.1	
	4746	5640		68.5	77	7.0	32	
	4750	5640	1.69	66	77	7.1	49	
Zn ₄ O(D ₂ -teppda) _{1,5}		2095		1	77	0.8		
Zn ₄ O(dbc) ₂	2476	3263	1.14	1	77	1.46		
IRMOF-6	2804	3305		45	77	4.63	31.7	
Zn ₄ O(dcbBn) ₃	396		0.13	48	298	0.98		
Zn ₄ O(dcdEt) ₃	502		0.2	48	298	1.12		
Zn ₄ O(H ₂ Nbdc) ₂	2446	3062	1.07	1	77	1.42		
Zn ₄ O(tpdc) ₃	1911	1911		1	77	1.59		
Zn ₄ O(NDC) ₃	1984	2337	0.45	33.7	77	3.4	26.7	9.1
	890			1	77	1.45		
	1466	1818		1	77	1.48		
				15	77	3.6	20.9	6.1
				30	298	0.4	2.32	
Zn ₄ O(mtB) ₂	1121		0.51	3	77	1.9		
Zn ₄ O(pyrdc) ₂	2100		0.73	1	77	1.73		

Tab.2.5 (continued)

Compound ^a	Surface area/m ² g ⁻¹		Pore vol./cm ³	Conditions		Hydrogen storage ^b		Q _{st} /kJ mol ⁻¹
	BET	Langmuir		P ₂ /bar	T/K	Excess/wt%	Vol./g L ⁻¹	
Zn ₄ O(umbdo) ₃	1501			1	77	0.88		
Zn ₄ O(ttdcd) ₂	3409	4346	1.53	1	77	1.32		
	4024	4593		77.6	77	6.25	34.1	
Zn ₇ O ₄ (pda) ₈ (H ₂ O) ₂			0.17	71.43	298	1.01		
Y(BTC)				1	77	1.57		7.3
Y ₂ (pdc) ₃	655			1	77	1.32		
Mo ₃ (BTC) ₂	1280	2010	0.67	1	77	1.75		
Pd(2-pymo) ₂	600			1.2	77	1.3	18	8-9
Pd(F-pymo) ₂	600			1.2	77	1.15	18	
Ag ₃ (Ag ₄ (trz) ₆)	810		0.324	64	77	2.33	41	
Cd(pyime) ₂		1168	0.47	1	77	1.16		8.7
				10	77	2.1	28.8	
Cd ₃ (bpcd) ₃		880	0.19	40	77	2.8	20.0	
In ₃ O(abc) _{1,3} (NO ₃)		1417	0.5	1.2	77	2.61	50	
[In(pmde) ₂ Na _{0.56} K _{1.23} (NO ₃) _{0.64} Sm ₂ Zn ₃ (oxde) ₆		616	0.25	1	77	0.9		8.4
			0.31	34	77	1.19	18.6	
Dy(BTC)	655			35	298	0.54	8.4	
Er ₃ (3,5-pdc) ₃	427			1	77	1.32		
Yb ₄ (tatb) ₈ (SO ₄) ₂	820 ^d		0.34	1	77	0.68		
				1	77	0.94		
Metal-cyanide frameworks								
Mn ₂ [Fe(CN) ₆]				1	77	0.0		
Mn ₃ [Co(CN) ₆] ₂	870			1.19	77	1.6	19	
Mn ₃ [Co(CN) ₆] ₂				1	77	1.71		
Fe ₃ [Co(CN) ₆] ₂	770			1.19	77	1.4	17	
Fe ₄ [Fe(CN) ₆] ₃	550			1	77	1.2		6.3-7.6
Co(pyzz)[Ni(CN) ₆]				1	77			7.2
Co(pyzz)[Pd(CN) ₆]				1	77			7.8
Co(pyzz)[Pt(CN) ₆]				1	77			7.6
Co[Fe(CN) ₅ (NO)]				1	77	1.61		7.5
Co ₂ [Fe(CN) ₆]	523			1	77	0.7		
Co ₃ [Co(CN) ₆] ₂	370			1	77	1.4		5.7-7.0
Co ₄ [Co(CN) ₆] ₃	730			1.19	77	1.5	19	
Co ₄ [Co(CN) ₆] ₃	800			1	77	1.84		
Ni(bpy)[Ni(CN) ₆]	234			1	77			7.5
Ni(bpy)[Pd(CN) ₆]	220			1	77	2.24		6
Ni(dpac)[Ni(CN) ₆]	398			1	77	1.76		7.2
Ni(pyzz)[Ni(CN) ₆]	124			1	77	1.68		6.5
Ni[Fe(CN) ₆ (NO)]	634			1	77	0.9		
Ni ₂ [Fe(CN) ₆]	460			1	77	1.4	18	6.0-6.6
Ni ₃ [Co(CN) ₆] ₂	560			1	77	1.6		5.6
Cu ₂ [Fe(CN) ₆]	730			1	77	2.22		6.3
				1	75	2.33		6.5
Cu _{1.6} Mn _{1.4} [Co(CN) ₆] ₂				1	77	1.4		
Cu _{2.3} Mn _{0.7} [Co(CN) ₆] ₂				1	75	2.6		
Cu ₃ [Co(CN) ₆] ₂	730			1.19	77	1.8	25	

Tab.2.5 (continued)

Compound ^a	Surface area/m ² g ⁻¹		Pore vol./cm ³	Conditions		Hydrogen storage ^b		Q _{st} /kJ mol ⁻¹
	BET	Langmuir		P/bar	T/K	Excess/wt%	Vol./g L ⁻¹	
Cu ₃ Co(CN) ₆ Δ ₂	750			1	77	1.8		6.6-6.8
Cu ₃ [Fe(CN) ₆] _{Δ₂}				1	75	2.61		6.9
Cu ₃ [Ir(CN) ₆] _{Δ₂}				1	75	1.79		7.0
Zn ₃ Co(CN) ₆ Δ ₂	720			1	75	2.39	18	7.15
H ₂ Zn ₃ [Fe(CN) ₆] _{Δ₂} ·2H ₂ O				1.19	77	1.1		7.8-8.2
Li ₂ Zn ₃ [Fe(CN) ₆] _{Δ₂} ·2H ₂ O	250			1.19	77	1.1	16	6.1-7.9
Na ₂ Zn ₃ [Fe(CN) ₆] _{Δ₂}	570			1.19	77	1.2	18	7.7
Rb ₂ Zn ₃ [Fe(CN) ₆] _{Δ₂}	430			1.19	77	1.1	19	7.3-7.9
K ₂ Zn ₃ [Fe(CN) ₆] _{Δ₂}	470			1.19	77	1.2	19	7.9-9.0
K ₂ Zn ₃ [Ru(CN) ₆] _{Δ₂}				1	75	1.66		8.3
K ₂ Zn ₃ [Os(CN) ₆] _{Δ₂}				1	75	1.5		8.4
Rb ₂ Zn ₃ [Fe(CN) ₆] _{Δ₂}				1	75	1.7		8.6
Rb ₂ Zn ₃ [Ru(CN) ₆] _{Δ₂}				1	75	1.19		6.8
Rb ₂ Zn ₃ [Os(CN) ₆] _{Δ₂}				1	75	1.3		7.2
C ₅₂ Zn ₃ [Fe(CN) ₆] _{Δ₂}				1	75	1.4		7.4
C ₅₂ Zn ₃ [Ru(CN) ₆] _{Δ₂}				1	75	0.95		6.2
C ₅₂ Zn ₃ [Os(CN) ₆] _{Δ₂}				1	75	1.11		6.9
Gal[Co(CN) ₆] _{Δ₂}	570			1	75	1.1		7.1
				1	75	1.1		6.3-6.9

Tab.2.5 (continued)

7. Methane Storage

Methane, unlike hydrogen, can be easily adsorbed to an appreciable extent at room temperature. To be effective in energy applications, the methane adsorbed in nanoporous materials (adsorbed natural gas, ANG) needs to compete with compressed natural gas (CNG), which will require a storage target for methane of approximately 35 wt% [234] or 180 v/v [235].

In the late 1990s, Menon and Komarneni [236] reviewed the methane storage results and prospects of several different types of porous materials, such as carbons, zeolites, silica gels, and mesoporous solids.

The heats of physisorption of methane generally range from 10 to 20 kJ mol⁻¹ and, as in the case of hydrogen, the startling feature of the results was the direct correlation of surface area with adsorption capacity, irrespective of the chemistry of the adsorbent material.

At the end of the 1990s, carbon materials had established themselves as the materials with the highest capacity for methane storage, although, because of the low packing densities of carbon, there was no real advantage of these materials over CNG storage [236].

In more recent times, however, there have been several more studies on carbonaceous materials that point to improved methane storage capabilities, including comparative reviews of the effect on adsorption capacity of changing the form of carbonaceous materials (e.g. powdered or fibrous, wet or dry) [237-242].

A particularly interesting piece of work involves the combination of adsorption in porous carbon materials with different potential gas

storage materials—natural gas hydrates (NGH) [243]. NGH materials consist of methane stored inside water cages as a clathrate. Adsorption of methane into wet carbon materials leads to formation of clathrates inside the pores of the material, which overcomes some of the disadvantages of NGH themselves.

The requirement of high surface areas for high adsorption capacity that is clear from the work on carbon materials points directly to the high porosity MOFs that have made such an impact in hydrogen storage. As long ago as in the late 1990s, Mori and Kitagawa proved that MOFs can adsorb large amounts of methane [244], and there have been some remarkable demonstrations of high methane adsorption by various research teams [245], in particular Yaghi's one, which demonstrated an exceptionally high uptake of methane in IRMOF-6 [246].

Even Düren et al.[235] used computational methods to calculate methane adsorption capacities, heats of adsorption, and surface areas of various different MOFs, zeolites, and carbon materials. Their conclusions indicated that the most important feature of materials that control methane adsorption is the surface area, followed by the free volume, the framework density, and the heats of adsorption. Other computational approaches have also been completed in recent years, with contributions towards understanding the adsorption mechanism and density of methane in carbon materials [247, 248] and MOFs [249-251].

Another intriguing development of this topic is the adsorption of mixed hydrogen/methane (“hythane”), particularly aimed at on-board

vehicle storage of fuel. At this regard, Kowalczyk and co-workers used Monte Carlo simulations to predict the properties of different carbon materials, and concluded that bundles of single-walled nanotubes in the 1–2 nm diameter range would be the best choice for this type of storage [252].

The challenges for synthesis chemists designing methane storage materials are similar to those posed for hydrogen storage materials, in particular the need for higher surface areas. The main difference between the two problems is that the interaction energy between methane and the surface of the materials is already enough to give reasonable adsorption at room temperature, and that the volumetric targets for methane adsorption are well within sight for both carbon materials and MOF-type solids. However, the engineering (and economic) challenges facing these materials before application have yet to be overcome, and this is particularly true in the case of MOFs, for which such studies are only now beginning.

8. Metal Organic Frameworks for Carbon Dioxide capture

Removal of CO₂ from the flue exhaust of power plants, currently a major source of emissions, is commonly accomplished by chilling and pressurizing the exhaust or by passing the fumes through a fluidized bed of aqueous amine solutions, both of which are costly and inefficient [253a].

Other methods based on chemisorption of CO₂ on oxide surfaces or adsorption within porous silicates, carbons, and membranes have been

pursued as means for CO₂ uptake [253b]. However, in order to obtain an effective adsorption medium with long term viability in CO₂ removal, two combined features are required:

- (i) a periodic structure for which CO₂ uptake and release is fully reversible;
- (ii) a flexibility by which chemical functionalization and molecular-level fine-tuning can be achieved for optimized uptake capacities.

Metal-organic frameworks (MOFs) represent a class of porous materials that offer these advantages for CO₂ storage: ordered structures, high thermal stability [254a], adjustable chemical functionality [254b], extra-high porosity [254c], and availability of hundreds of crystalline, well-characterized porous structures yet to be tested [254d-k].

Andrew R. Millward and Omar M. Yaghi [255] embarked on a program to assess the viability of MOFs in CO₂ storage. They selected nine compounds in order to examine a range of structural and porous attributes (Figure 2.1).

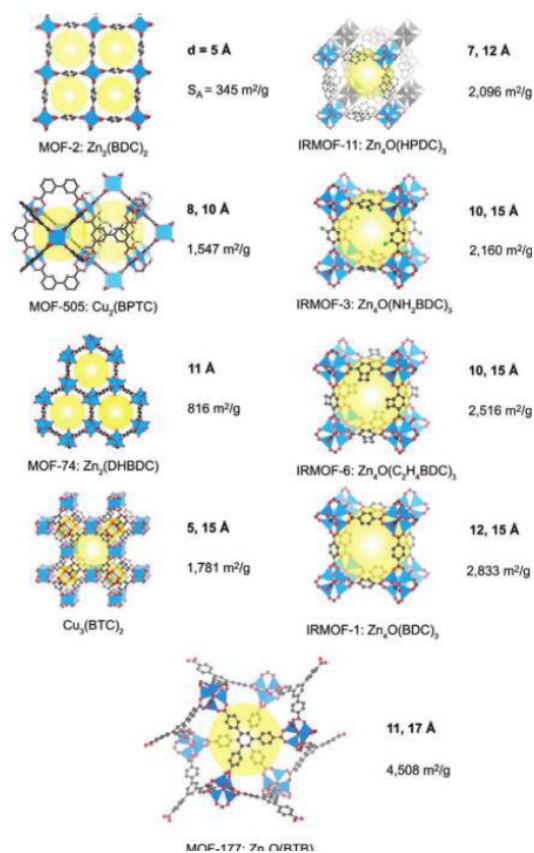


Fig. 2.1 Crystal structures of MOFs examined for CO₂ storage capacity at room temperature. For each MOF, the framework formula, pore size, and surface area are given [255].

This list represents a sort of overview of different framework characteristics: structures exhibiting square channels (MOF-2) [256a], pores decorated with open metal sites (MOF-5 and Cu₃(BTC)₂) [256b,c] hexagonally packed cylindrical channels (MOF-74) [256d], interpenetration (IRMOF-11) [255 b], amino- and alkyl-functionalized pores (IRMOFs-3 and -6)[255b], and extra-high porosity (IRMOF-1 and MOF-177) [255a,c] are all taken into account.

Silica- and carbon-based physisorptive materials such as zeolites and activated carbons are often referenced as benchmark materials for CO₂

sequestration. In particular, zeolites have enjoyed high utility in industrial applications based on their well-defined pore shapes and narrow pore-size distributions, but the highest reported gravimetric CO₂ capacity for these materials at ambient temperature is limited to 7.4 mmol/g (at 32 bar) for zeolite 13X [257].

On the other hand, several carbons have been reported to have quite high CO₂ adsorption capacities despite their amorphous nature, with the sample of MAXSORB showing an uptake of 25 mmol/g (at 35 bar) [258].

In the aforementioned comparison work, Andrew R. Millward and Omar M. Yaghi [255] have shown that the CO₂ adsorption capacity of MOF-177 at ambient temperature (33.5 mmol/g) fairly exceeds those of standard materials by 150%.

Chapter III:

Purpose of this Defense

1. Introduction

The Kyoto's protocol, which oblige the Countries that signed it to reduce the emissions of CO₂ to control the greenhouse effect, made more pressing the necessity to use poor carbon fuel.

Farther, in the cities, the high concentration of toxic gasses in air, produced by traffic and by domestic use of fuels, obliges the industrialized country to study always stricter parameters and control norms about fuels and motors.

As we have amply illustrated in Chapter II, the MOF are materials that are widely used in various sectors of industry.

In particular, in this defense, we focused our attention on the possibility of application of MOF (Metal-Organic Framework) in hydrogen storage, the capture of CO₂ and water vapor adsorption.

2. Hydrogen: The resource of the future

Hydrogen is the lightest and most abundant element in the universe.

However, it is very rare on Earth in the free state, because of its extreme volatility.

To be able to provide industrially useful quantities should therefore remove compounds which contain it in abundance (e.g. water, fossil fuels, from minerals and plant organisms) using an external energy source.

For this reason, hydrogen, like electricity, must be considered an energy carrier, rather than a primary energy source.

The interest for its use as a fuel for both industrial applications as for the fuel for vehicles, is that the pollution produced by hydrogen is almost zero.

When it is used in combustion systems has, in fact, only water vapor and traces of nitrogen oxides, while producing only water vapor when it is used with electrochemical systems (fuel cells).

Technologies for hydrogen production from fossil fuels (especially coal) are mature and widely used, although it should be optimized from the point of view energy and environmental impact.

Of the approximately 500 billion m³ of hydrogen are produced annually worldwide, about 190 billion are product by the chemical industry, with the vast quantity comes from fossil fuels (natural gas, heavy oil and coal) through processes of reforming, partial oxidation, pyrolysis and gasification.

The production of hydrogen from fossil fuels have the disadvantage of giving rise to emissions, such as waste products, large amounts of CO₂, greenhouse gas known.

However, just the production of hydrogen from coal and hydrogen generated as a product by the chemical industry now seems the only feasible way to start a production chain of a size to achieve the necessary economies of scale.

The direct extraction of hydrogen from water has, at the moment, a single process established industrial: electrolysis.

In this case gives rise to a process of environmentally sustainable production and consumption, but requires a corresponding amount of clean electricity that can power the electrolysis process.

The problem is therefore that of the cost: with the electrolysis of water, in fact, one can obtain virtually pure hydrogen, but at a price which may be economically acceptable in a more distant perspective, when technological innovations will allow the use for the making electricity from renewable (or nuclear) at very low costs.

Other points to consider carefully are also those related to the difficulty of transportation and storage, both for the low energy density, and because hydrogen is explosive, flammable and extremely volatile.

The development of hydrogen as an energy option is therefore of great interest to help solve the energy problems of the planet, but requires substantial improvements in existing technology and research of innovative technologies to make economic use and reliable in various stages of technology chain (production, transportation, storage, end use).

This is a challenge not simple, you are now facing with a number of technologies to the study.

In this scenario, Italy may have a leading role, as the scientific knowledge and technological capabilities are held at top international level.

2.1 The U.S. Department of Energy's "Grand Challenge"

Hydrogen storage is widely recognized as a critical enabling technology for the successful commercialization and market acceptance of hydrogen powered vehicles.

Storing sufficient hydrogen on-board a wide range of vehicle platforms, while meeting all consumer requirements (driving range, cost, safety, performance, etc.), without compromising passenger or cargo space, is a tremendous technical challenge.

The U.S. Department Of Energy (DOE), in collaboration with automotive industry partners, established specific technical targets for on-board hydrogen storage systems to focus R&D and to stimulate research on hydrogen storage.

In order to achieve these long-term targets, DOE launched a "Grand Challenge" to the scientific community in 2003.

Based on a competitively selected portfolio, DOE established a "National Hydrogen Storage Project" in the U.S. for R&D in the areas of advanced metal hydrides, chemical hydrogen storage, carbon-

based and high surface area sorbent materials, as well as new materials and concepts.

There are three primary barriers that must be overcome to enable industry commercialization of hydrogen fuel cell vehicles:

- (1) on-board hydrogen storage systems are needed that allow a vehicle driving range of greater than 500 km while meeting vehicle packaging, cost and performance requirements;*
- (2) fuel cell system cost must be lowered to \$ 30 per kilowatt by 2015 while meeting performance and durability requirements;*
- (3) the cost of safe and efficient hydrogen production and delivery must be lowered to be competitive with gasoline (a target of \$ 2.00 to \$ 3.00 per gallon gasoline equivalent, delivered, untaxed, by 2015) independent of production pathway and without adverse environmental impact [259]*

2.2 Hydrogen for automotive applications

Hydrogen has the highest energy content per unit of weight of any known element. It is also the lightest element.

As a result, it is characterized by low volume energy density, meaning that a given volume of hydrogen contains a small amount of energy.

This presents significant challenges to storing the large quantities of hydrogen that will be necessary in the hydrogen energy economy.

A critical challenge for transportation applications is balancing the need for a conventional driving range (> 480 km) with the vehicular constraints of weight, volume, efficiency, safety, and the cost of on-board hydrogen storage systems.

A second set of challenges for transportation applications relate to durability over the performance lifetime of on board storage systems.

The principal challenges to improving hydrogen storage technologies relate to increasing their efficiency, size, weight, capacity and, ultimately, their cost.

Durability remains an issue, as does the development of unified international codes and safety standards to facilitate safe deployment of commercial technologies.

1. **Cost.** The cost of on-board hydrogen storage systems is currently too high, particularly in comparison with conventional storage systems for petroleum fuels. Low-cost materials and components for hydrogen storage systems are needed, as well as low-cost, high-volume manufacturing methods.
2. **Weight and volume.** The weight and volume of hydrogen storage systems are presently too high, resulting in inadequate vehicle range compared to conventional petroleum fuelled vehicles. Materials and components are needed to allow compact, lightweight hydrogen storage systems that allow driving ranges similar to those available today for light-duty vehicle platforms.

3. **Efficiency.** Energy efficiency is a challenge for all hydrogen storage approaches. The energy required to get hydrogen in and out of storage is an issue for reversible solid-state materials storage systems. In addition, the energy associated with compression and liquefaction must be factored in when considering compressed and liquid hydrogen storage technologies.
4. **Durability.** The durability of some hydrogen storage systems is inadequate. Materials and components are needed that allow hydrogen storage systems with a lifetime in excess of 1,500 refuelling cycles.
5. **Refuelling time.** Refuelling times are currently too long. There is a need to develop hydrogen storage systems with refuelling times of less than three minutes, over the lifetime of the system.
6. **Codes and Standards.** Applicable codes and standards for hydrogen storage systems and interface technologies, which will facilitate implementation, commercialization and assure safety and public acceptance, have not yet been established. Standardized hardware and operating procedures are required [260].

3. MOF in the field of CO₂ capture

In the area of separation processes, plays a role important to remove carbon dioxide from flue gases.

Just to think, for example, the need to reduce emissions of this chemical species in the atmosphere in order to control the greenhouse effect, or as needed to obtain current of hydrogen (from steam reforming plants) pure enough to feed cells the fuel.

The process of separation of CO₂ from gas streams more commonly used is based on the use of cryogenic technology.

The energy demand of these processes is rate absolutely not negligible compared to the energy needs the world.

Therefore, they are advantageously carried out only when CO₂ is present in high concentrations in the gas process, with the added convenience of producing liquid CO₂, immediately ready for transport by pipeline.

Other techniques are widely used for removing of carbon dioxide are represented physical and chemical absorption.

The physical absorption takes place in a liquid medium which acts simply as a solvent, usually water, while the chemical is follows when CO₂ reacts chemically with the liquid absorbent or with appropriate reagents present within it, as in the case of aqueous solutions of monoethanolamine (MEA).

A process that still requires further development before they can be used on a large scale for the removal of CO₂, is based use of membranes, one interesting feature is certainly the low energy demand.

In last ten years, the gas separation technology based on adsorption has become an interesting object of study and found a large spread mainly due to higher efficiency compared to the cryogenic separation [261].

A key aspect of these processes is certainly the identification of the best adsorbent material.

It should have a good ability to adsorption (weight of carbon dioxide adsorbed per unit mass of adsorbent), a satisfactory selectivity (ratio of carbon carbon dioxide and other gaseous species adsorbed), a favorable kinetic (Ratio between the rate of adsorption of carbon dioxide and of other gaseous species), and a remarkable ease of regeneration.

To this end were examined traditional adsorbent materials to high surface area, such as silica gel, activated alumina and carbon active.

In addition, zeolite materials have been studied, whose particular crystal structure means that the size of the micropores are homogeneous, making them much more selective than conventional amorphous adsorbent [262].

Over the last fifteen years has finally gained considerable interest in several industrial fields, the class of materials consisting of the silica meso-structures: these solids, following appropriate processes functionalization can be used in different types of processes, including adsorption.

4. Solar cooling

The solar cooling is to combine between solar panels and a refrigerating machine. In other words, the solar cooling technology allows the production of cold, in the form of chilled water or air-conditioning, starting from a heat source.

The panels are commonly used in solar cooling systems are:

- Panels tears glazed selective
- Vacuum Panels
- Panels air (only for DEC systems)

Considering the high cost and sizes that characterize the cooling machines (a few under 20 kW), to date, the solar cooling is feasible only for systems of air conditioning / refrigeration-type central. The air / cold water is brought in individual parts of the building through a system of pipes or a distribution network.

The simplified diagram of the solar cooling technology works is as follows:

- solar panels absorb the sun's radiation and convert it into water or hot air
- water or hot air produced by the panels is fed through the chiller, which turns it into water or cold air
- water or cold air is used to cool environments or for industrial refrigeration.

4.1 Because the solar cooling

The solar cooling exploits the fact that the hours of the day (summer) in which there is greater demand for air conditioning cooling of buildings, coincide with the maximum availability of solar radiation.

And it's known as peak demand electricity occurs during the summer (and until a few years ago were typical of the winter season), due to the simultaneous operation of millions of small air conditioners.

The solar cooling is beneficial on two fronts. From the standpoint of the national electricity system, the widespread use of this technology can help to ease the pressure on the electricity grid, avoiding the dangerous summer peaks. From the point of view of those who choose to install a solar cooling, there are significant benefits in terms of energy and cost savings. Without considering the reduction of polluting emissions and CO₂ in the atmosphere.

Another factor in favor of solar cooling is the fact that you use all the hot water produced by solar medium and large size, even during the summer season.

The application of solar cooling is usually recommended in combination with solar systems "combined", is designed to heat the hot water for space heating. To perform this double duty, the combined plants are made up of large areas of panels. In the absence of a use of heat in the summer (for example to heat water in a pool), there is a real danger that much of the hot water produced by the plant is wasted.

The chilled water through a pipe system, is distributed to the end of cooling situated in the premises to be air conditioned. The advantage of closed loop systems is the ability to build the facility with any type of distribution network, both air and water.

Open-loop systems

We produce systems with DEC (Desiccant & Evaporative Cooling Systems), which combine dehumidification and evaporative cooling. These innovative treatment systems direct air, alternative to traditional compression. The most common technology (see Figure 3.2) involves the use of rotary dehumidifiers solid absorbents such as zeolites or another porous material such as Metal-Organic Framework.

The first air taken from outside is dehumidified and cooled through the use of water as a coolant. The heat produced by solar panels instead serves to regenerate the dehumidifier. They can be also used solar panels to air. It is a technology applicable to buildings of a certain size equipped with ventilation system, where the need to cool it also adds the need to control the humidity of the air.

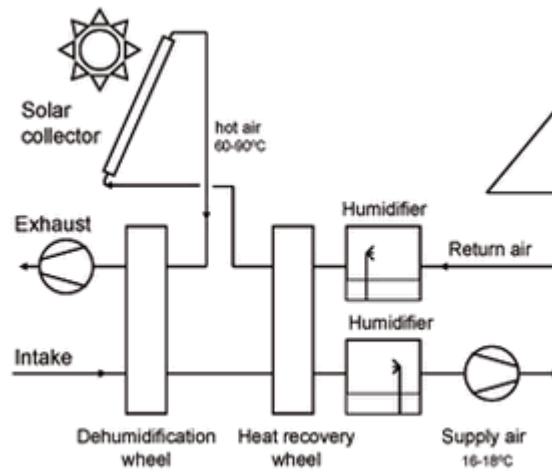


Fig.3.2 Open-loop systems

5. Purpose of the Defense

In this PhD defense we have focused our attention on the choice of some MOF terms to destine to hydrogen storage, carbon dioxide capture and water vapor adsorption.

After a careful analysis of the literature we have choice three terms that, in our opinion, are to the purpose.

Our choice was driven by some criteria, we decided to focus our energy to study materials with these characteristics:

- Simple hydrothermal treatment to synthesize them;
- No toxic reagents to obtain the final product;
- No too expensive reagents or treatments to adopt for them.

So our choices were for:

- Cu-BTC to test for hydrogen storage and carbon dioxide capture;
- Cu-TRZ to test for water vapor adsorption for solar cooling application.
- MIL-101 to test in the field of hydrogen storage

Chapter IV

Experimental Activity

1 Experimental details regarding Cu-BTC MOF

1.1 Synthesis

Cu-BTC samples were obtained as powders using a procedure described by Wang and co-workers [263]: 2.46 g (11.7 mmol) of benzene-1,3,5-tricarboxylic acid (Aldrich) were dissolved in 13 mL of ethanol (Baker), and 5.43 g (23.3 mmol) of copper nitrate hydrate (Baker) were dissolved in 13 mL of double distilled water. The two solutions were then mixed at ambient temperature and aged for 30 min, after which the resulting mixture was heated at 383 K under solvothermal conditions for 18 h. The reaction vessel was allowed to reach ambient temperature, and the resulting blue crystals were isolated by filtration and washed with double distilled water. The final product was then dried at 383 K overnight.

1.2 Characterization of synthesis products

Powder X-ray diffraction (XRD) patterns of Cu-BTC samples were collected using a Philips PW1710 apparatus (CuK α radiation). The

scanning step size was 0.020° in 2θ , and the time for each step was 1 s. In light of the well-known sensitivity to moisture that characterizes Cu-BTC [263], the XRD patterns were obtained while taking special care to minimize water adsorption by the samples to be analyzed, and with this aim, the dried samples were exposed to ambient air for a minimal amount of time. Unit cell constants were calculated using the McMaille 4.00 software package starting from the 20 most significant diffraction peaks.

Scanning electron microscopy (SEM) micrographs were collected with a Cambridge S440 instrument, while thermogravimetric (TG) analysis was carried out with a Netzsch STA 409 Luxx device using samples with masses of about 0.020 g that were heated in an air flow from ambient temperature up to 673 K at a rate of 10 K min^{-1} and using α -alumina as reference.

Microporosimetric characterization was carried out by N_2 adsorption/desorption cycles at 77 K, and the specific surface area was evaluated by means of the Brunauer-Emmett-Teller (BET) method. A Micromeritics ASAP 2020 volumetric instrument was used for this purpose, and synthesized samples were degassed at 423 K for 3 h prior to characterization.

CO₂ adsorption isotherms on Cu-BTC and 13X zeolite (that was used as a benchmark) were obtained using the ASAP 2020 instrument mentioned above. However, since ASAP-series devices were mainly designed to work at the boiling temperatures of noble/inert gases, the Dewar flask in which the sample tube is usually immersed was substituted by an “ad hoc” container whose shell was filled with flowing thermostated water. 13X zeolite samples used for adsorption experiments were supplied by Carlo Erba (Italy) and used as purchased. Prior to each adsorption experiment, Cu-BTC samples were degassed under high vacuum at 423 K for 3 h, while for 13X samples, because of their greater thermal stability, a degassing temperature of 573 K was chosen. Since no preliminary data about the CO₂ adsorption kinetics on the adsorbent samples synthesized in this work were available, each adsorption step was allowed to approach equilibrium over a period of (1 to 2) h in order to collect isotherm points that could be reliably considered as depictive of an equilibrium state. Adsorption isotherms were obtained at four different temperatures, namely, T = (283, 293, 318, and 343) K.

N₂ adsorption isotherms for both Cu-BTC and 13X were also obtained at T = 293 K.

In the end, hydrogen adsorption isotherms at 77 and 296 K on Cu-BTC were obtained using an HPVA (static-volumetric) analyzer. The adsorption data were obtained for pressures up to 200 bar.

2. Experimental details regarding Cu-TRZ MOF

2.1 Synthesis

Samples of $[\text{Cu}^{\text{II}}_3(\text{triazolate})_3(\text{OH})_3(\text{H}_2\text{O})_4]\cdot 4.5\text{H}_2\text{O}$ (Cu-TRZ) were obtained as powders starting from the procedure described by Ouellette and coworkers [264]: 0.652 g (2.512 mmol) of copper sulfate pentahydrate (Aldrich) and 0.192 g (2.776 mmol) of 1,2,4-triazole (Aldrich) were dissolved in 40 g of double distilled water. Several solutions with this composition were then aged at ambient temperature for 10 minutes, after which the resulting mixtures were heated at 473 K under hydrothermal conditions for different time intervals, ranging from 1 to 168 h. The resulting blue crystals were isolated by filtration and washed with double distilled water. The final products were then dried at 333 K overnight.

2.2 Characterization of synthesis products

X-ray diffraction (XRD) was performed on Cu-TRZ samples using a Panalytical X'pert Pro device (CuK α radiation, 40 kV, 40 mA, RTMS

X'celerator detector). Scanning electron microscopy (SEM) micrographs were collected with a Cambridge S440 instrument, while particle size distributions were determined with a Malvern Mastersizer 2000 equipment. Data for single crystal structure determination were measured on a Bruker-Nonius KappaCCD diffractometer using graphite monochromated MoK α radiation (0.71073 Å) at 295 K. Reduction of data and semiempirical absorption correction were performed using the SADABS program. The structure was solved by direct methods and refined by the full matrix least-squares method on F² using the SHELXL-97 program. Non-hydrogen atoms were refined anisotropically; H atoms were stereochemically positioned.

Thermogravimetric (TG) analysis was conducted with a Netzsch STA 409 Luxx device using samples weighing approximately 0.020 g, heated in nitrogen flow from ambient temperature up to 1023 K at a rate of 10 K/min using α -alumina as a reference.

Microporosimetric characterization was performed with CO₂ adsorption at 273 K, and the specific surface area was evaluated with the Langmuir method. A Micromeritics ASAP 2020 volumetric instrument was used to determine the specific surface area, and, prior

to characterization, the synthesized samples were degassed at 348 K for 3 h.

Water vapor adsorption isotherms on Cu-TRZ were obtained using a gravimetric technique based on a McBain-type balance [265]. Prior to each adsorption run, Cu-TRZ samples were degassed under high vacuum at 348 K for 3 h. The degas temperature for all adsorption runs was chosen to compare the results with those reported elsewhere [264]. For every adsorption equilibrium point, the weight change of the sample was registered every 15 min. When no weight change was observed between two consecutive measures, the final one was performed after one more hour to ensure that equilibrium conditions were reached. Adsorption isotherms were obtained at four different temperatures, $T = 293, 303, 323, \text{ and } 343 \text{ K}$ [266].

3. Experimental details regarding MIL-101 MOF

3.1 Synthesis

Samples of MIL-101 were synthesized by the method reported by Feréy et al [267]. The synthesis of MIL-101 consists in the hydrothermal reaction of 0.166 g (1 mmol) of H₂BDC (terephthalic

acid) with 0.400 g (1 mmol) of chromium nitrate hydrate, 0.2 ml (1 mmol) of hydrofluoric acid and 4.8 ml (265 mmol) of H₂O for 8 h at 493 K. The final product was then dried at 333 K overnight.

3.2 Characterization of synthesis products

Powder X-ray diffraction (XRD) patterns of MIL-101 samples were collected using a Philips PW1710 apparatus (CuK α radiation). The scanning step size was 0.020° in 2 θ , and the time for each step was 10 s.

Microporosimetric characterization was carried out by N₂ adsorption/desorption cycles at 77 K, and the specific surface area was evaluated by means of the Brunauer-Emmett-Teller (BET) method. A Micromeritics ASAP 2020 volumetric instrument was used for this purpose, and , prior to characterization, the synthesized samples were degassed at 370 K for 30 h.

Hydrogen adsorption isotherms at 77 and 296 K on MIL-101 were obtained using an HPVA (static-volumetric) analyzer. The adsorption data were obtained for pressures up to 200 bar.

The hydrogen adsorption properties of MIL-101 were also assessed at 77 K and at 1 and 2 bar of H₂ under dynamic conditions. The

experiments were carried out by using a fixed bed reactor made of pyrex glass and equipped with a manometer for pressure control. The sample (2 g) was loaded in powder form (100- 200 μm), dried at 373 K in nitrogen flow (1 NL/min) and cooled down to room temperature. Then a stream of pure hydrogen (0.7 NL/min) was fed at the selected pressure and room temperature, and after 10 minutes the reactor was inserted into a Dewar flask filled with liquid nitrogen. After 30 minutes a nitrogen flow rate of 0.7 NL/min was sent through the sample at ambient pressure as carrier gas for the hydrogen release phase. The hydrogen concentration at the reactor outlet was measured by a Caldos 17 ABB on line analyzer equipped with TCD detector, while for gas flow rate measurement two mass flow controllers were adopted. Hydrogen concentration at the reactor outlet was continuously acquired by a National Instrument acquisition board managed by LabView software. A preliminary test with an empty reactor (no adsorbent) was effected with the same procedure above described, to evaluate the hydrogen concentration profile at the reactor outlet in the absence of adsorption process.

Chapter V

Results and Discussion

1. Materials characterization

1.1 Cu-BTC

The XRD pattern of synthesized Cu-BTC, which is shown in Figure 5.1, is consistent with those reported in the literature [263]. The noticeably strong intensity of peaks in the pattern can usually be related to the formation of large crystals, but in this case it might also be related to the low water content inside the pore structure of the sample itself [268]. This in turn depends on the fact that, as mentioned in the previous chapter, the analyzed sample was introduced into the analysis chamber immediately after the drying process at 383 K. The refinement of the diffraction pattern indicated that synthesized Cu-BTC crystals have cubic symmetry with a unit cell constant of 26.313 Å. Such results are fairly comparable with those reported by Chui and co-workers [269], who registered the same symmetry and a unit cell constant of 26.343 Å.

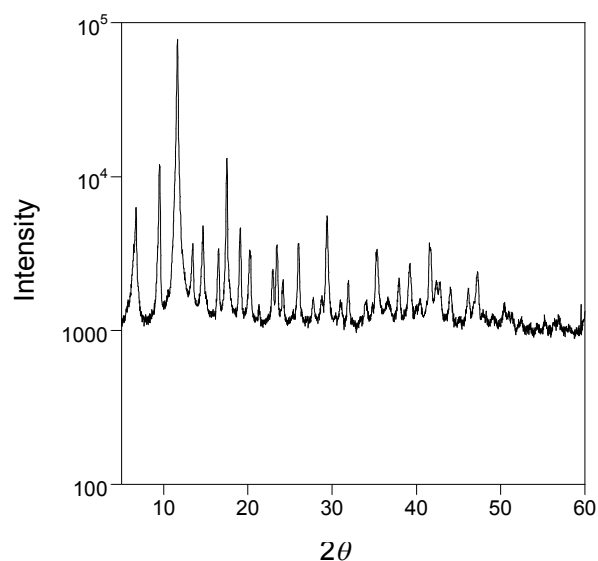


Fig.5.1 Powder XRD pattern of synthesized Cu-BTC.

Figure 5.2 shows a SEM micrograph of synthesized Cu-BTC: although the large particle shown in the figure is clearly polycrystalline, the reported image is consistent with the indications deriving from inspection of Figure 5.1 regarding the strong crystallization process that occurs during MOF phase synthesis. The morphology of the cubic-shaped particle is also consistent with other SEM investigations performed on Cu-BTC [263, 270].

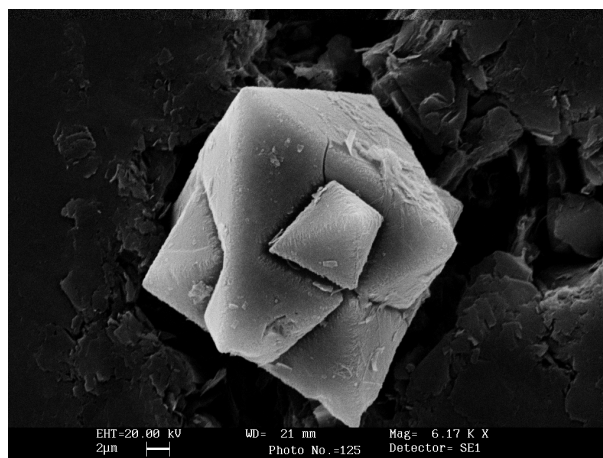


Fig.5.2 SEM micrograph of synthesized Cu-BTC crystals.

Figure 5.3 shows the results of TG analysis of synthesized Cu-BTC and highlights two main weight losses. The first loss registered in Figure 5.3 occurs at a temperature of about 370 K and is ascribable to water desorption phenomena. The second weight loss, which occurs between 570 and 630 K with a more pronounced extent than the first one, is due to the decomposition of the framework, which probably proceeds by partial combustion of benzenetricarboxylate moieties and formation of copper oxides [268].

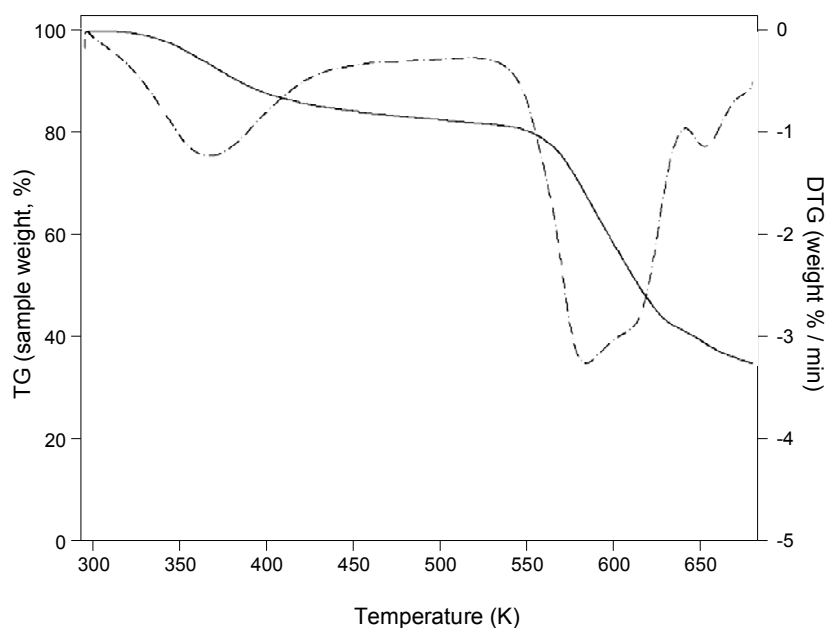


Fig.5.3 Thermogravimetric (TG) analysis curve (solid) and differential thermogravimetric (DTG) analysis curve (dot-dashed) of synthesized Cu-BTC.

Figure 5.4 shows N_2 adsorption/desorption isotherms on synthesized Cu-BTC measured using the ASAP 2020 apparatus at 77 K. Quite apparently, the curve reported in Figure 5.4 is a type I isotherm, which is typical of microporous materials [271]. The absence of hysteresis phenomena confirmed that the synthesized product possessed no other pore system apart from that of the micropores. At saturation, the adsorbed amount of N_2 was $19.8 \text{ mol}\cdot\text{kg}^{-1}$ under the assumption that the adsorbate density is that of the liquid phase (the so-called

“Gurvitch rule”) [272], multiplying by the molar volume of liquid nitrogen at 77 K ($34.7 \text{ cm}^3 \cdot \text{mol}^{-1}$, as reported by Wang and co-workers [263]) leads to an estimated intracrystalline porosity of $0.57 \text{ cm}^3 \cdot \text{g}^{-1}$ for Cu-BTC. This is comparable to, if not higher than, other values previously reported in the literature. For example, Wang and co-workers [263] reported an intracrystalline porosity of about $0.66 \text{ cm}^3 \cdot \text{g}^{-1}$, while Schlichte and co-workers [268] reported a value of $0.41 \text{ cm}^3 \cdot \text{g}^{-1}$. It must be noted that Cu-BTC samples with very high intracrystalline porosity seem to be producible only from synthesis routes that involve the use of significantly hazardous reagents such as N,N-dimethylformamide [273] or require very slow heating and cooling ramps [274]. Moreover, it is important to remark that the aforementioned value of the pore volume for Cu-BTC is more than 60% higher than that of 13X zeolite ($0.35 \text{ cm}^3 \cdot \text{g}^{-1}$) [275]. In regard to the specific surface area for synthesized samples, calculations based on the BET model led to a value of $1400 \text{ m}^2 \cdot \text{g}^{-1}$, which is more than 2 times the result reported for commercial 13X ($616 \text{ m}^2 \cdot \text{g}^{-1}$) [276].

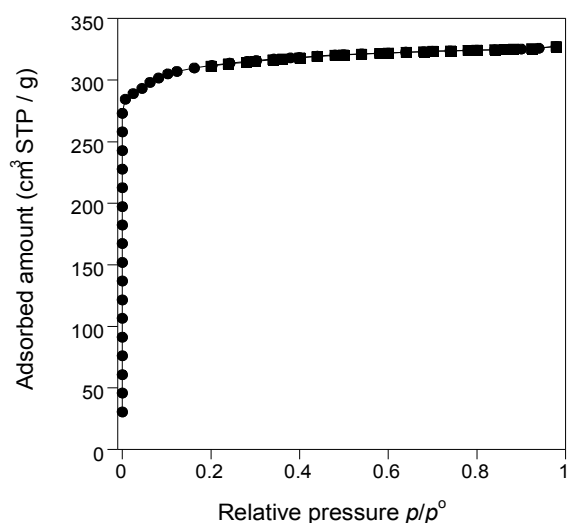


Fig.5.4 N₂ adsorption (●) and desorption (■) isotherms on synthesized Cu-BTC, measured using an ASAP 2020 apparatus at 77 K.

1.2 Cu-TRZ

Fig. 5.5 shows the XRD pattern of the Cu-TRZ sample synthesized after 1 h of hydrothermal treatment (Cu-TRZ-1): although the synthesis time is much lower than that reported by Ouellette and coworkers [264], the pattern is consistent with the simulated one, which was obtained from the Crystallographic Information File submitted by those authors to The Cambridge Crystallographic Data Centre under the code CCDC-289564. XRD was also performed on

Cu-TRZ samples synthesized for longer times, and the results were not substantially different from those reported.

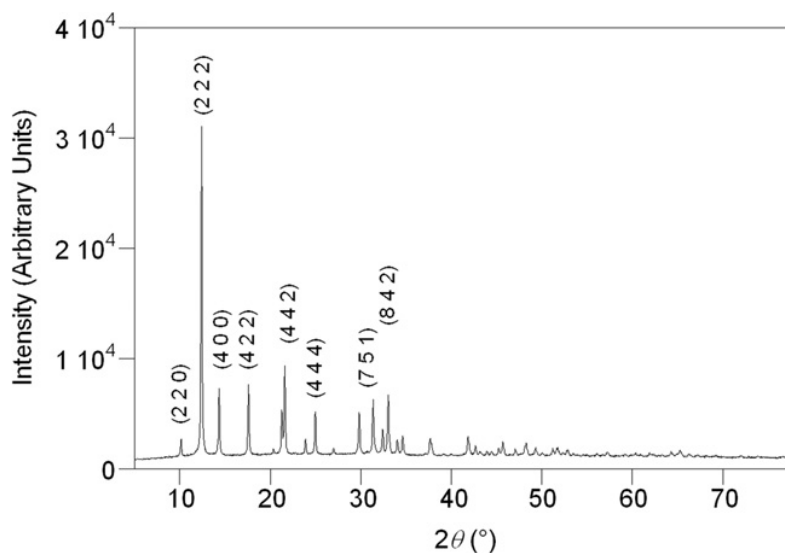


Fig.5.5 X-ray diffraction (XRD) pattern of Cu-TRZ synthesized in 1 h (Cu-TRZ-1).

Fig. 5.6 shows an SEM micrograph of Cu-TRZ-1: the solid is produced in the form of crystallites with an average size of less than $1 \mu\text{m}$ and a poorly defined morphology. For these reasons, Cu-TRZ-1 was not chosen for water vapor adsorption runs, and the synthesis products obtained after longer process times were examined.

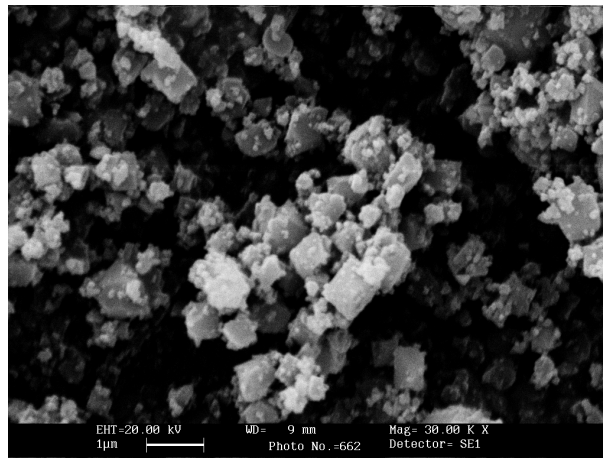


Fig.5.6 SEM micrograph of Cu-TRZ-1

Fig. 5.7 shows an SEM micrograph of a Cu-TRZ sample synthesized after 48 h of hydrothermal treatment (Cu-TRZ-48) and reveals the coexistence of crystallites greater than 10 µm in size together with the much smaller ones already observed in Cu-TRZ-1.

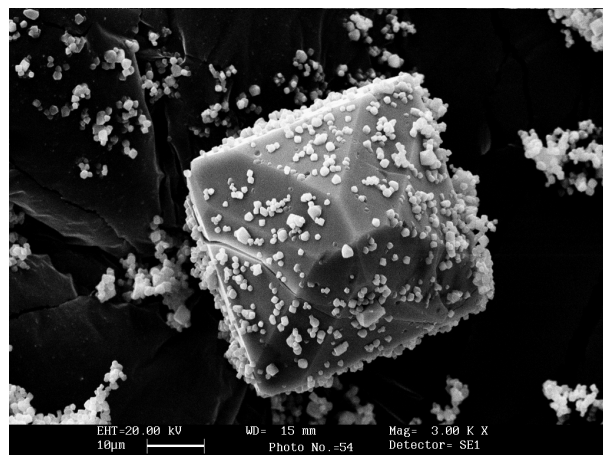


Fig.5.7 SEM micrograph of Cu-TRZ-48

Moreover, some of the smaller crystallites seem to be partially integrated with the surface of the larger ones, as illustrated in Fig. 5.8.

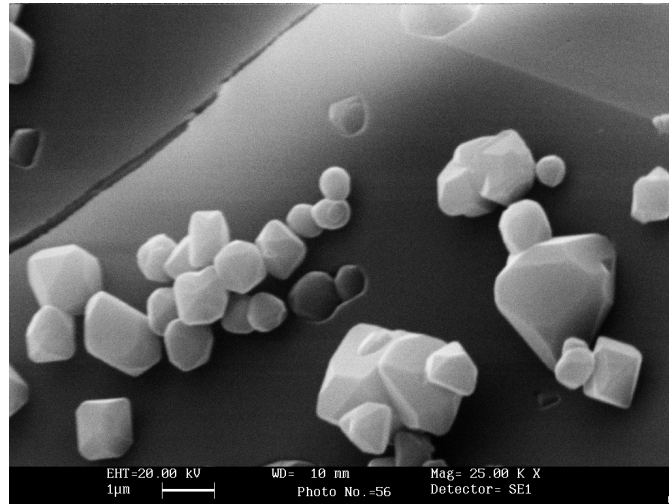


Fig.5.8 SEM micrograph of the smaller crystallites (Cu-TRZ-48).

Fig. 5.9 shows an SEM micrograph of a Cu-TRZ sample synthesized after 168 h of hydrothermal treatment (Cu-TRZ-168) and suggests the absence of the sub-micron-sized crystallites registered in the Cu-TRZ-1 and Cu-TRZ-48 samples.

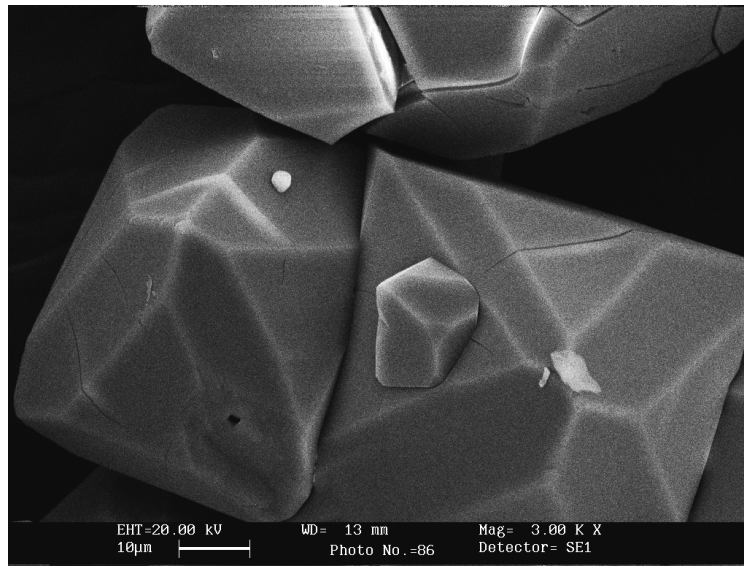


Fig. 5.9 SEM micrograph of a Cu-TRZ-168

To confirm the latter observation, the particle size distributions of Cu-TRZ-1, Cu-TRZ-48 and Cu-TRZ-168 were measured, and the corresponding results are reported in Fig. 5.10.

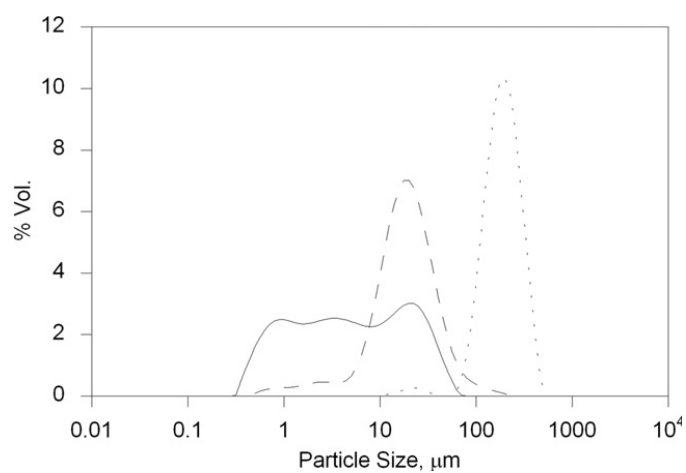


Fig.5.10 Particle size distributions of Cu-TRZ-1 (continuous curve), Cu-TRZ-48 (dashed curve) and Cu-TRZ-168 (dotted curve).

It can be noted that Cu-TRZ-1 actually shows a widely spread particle size distribution, in which three peaks are barely recognizable at about 1, 3.5 and 20 μm . In contrast, Cu-TRZ-48 shows a main peak centered at around 20 μm and a shoulder consisting of smaller particles. In addition, the particle size distribution of Cu-TRZ-168 is sharply centered around 200 μm , with the exception of a very small fraction of particles spread around 20 μm , which demonstrates that the average particle size of Cu-TRZ constantly grows as the synthesis time increases and that no Cu-TRZ-168 particle is smaller than 10 μm .

Moreover, Cu-TRZ-168 was submitted to single crystal XRD analysis, and the corresponding structural refinement resulted in a cubic cell with space group $Fd\bar{3}c$ and $a = 24.693 \text{ \AA}$, in very good agreement with the data reported by Ouellette and coworkers. These results undoubtedly confirm that, during the synthesis process, Cu-TRZ evolves towards large single crystals that grow at expense of the smaller ones. For this reason, Cu-TRZ-168 was chosen as the adsorbent for the water vapor adsorption runs.

Fig. 5.11 shows the results of the TG analysis of Cu-TRZ-168 and highlights three main weight losses, as already reported by Ouellette and coworkers [264]. The first loss registered in Fig. 5.11 occurs

between room temperature and 473 K and can be ascribed to the loss of the H₂O molecules of crystallization. The coordinated H₂O and the organic components are lost in two steps between 573 and 623 K and between 673 and 953 K.

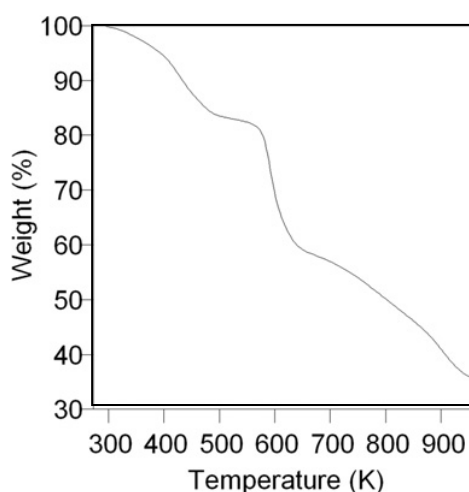


Fig.5.11 Thermogravimetric (TG) analysis of Cu-TRZ-168.

Fig.5.12 shows the CO₂ adsorption isotherm at 273 K of Cu-TRZ-168. Prior to performing CO₂ adsorption, a study of the N₂ adsorption at 77 K was also attempted but registered no significant adsorption phenomena.

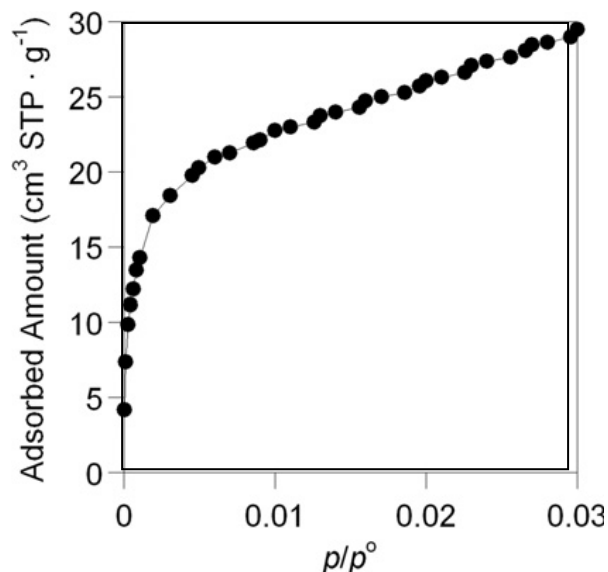


Fig.5.12 CO₂ adsorption isotherm on Cu-TRZ-168, measured by an ASAP 2020 apparatus at 273 K.

Though the dehydrated form of Cu-TRZ is declared to contain cavities of considerable volume (corresponding to 41.4% of the unit-cell volume) [264], the degas temperature chosen here removed the adsorbed water vapor molecules but not the H₂O molecules of crystallization. Thus, the pore system of Cu-TRZ was inaccessible to N₂ molecules at 77 K. An alternative method for the surface area analysis of solids whose pores are not accessible by N₂ molecules at 77 K is provided by CO₂ adsorption at 273 K [277], as confirmed by the fact that experimental data reported in Fig. 5.12 could be successfully processed by means of the Langmuir model to yield a specific surface area of approximately 160 m²/g.

1.3 MIL-101

The XRD pattern of synthesized MIL-101, which is shown in Figure 5.13, is consistent with those reported in the literature [87].

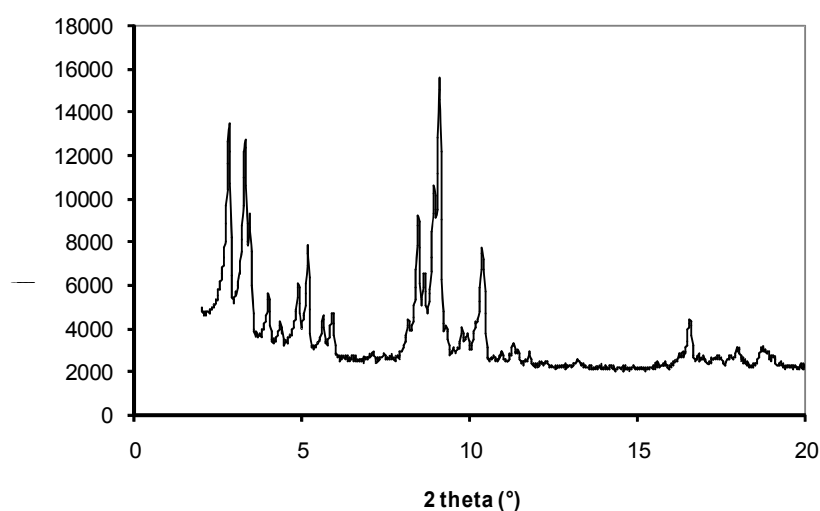


Fig.5.13 Powder XRD pattern of synthesized MIL-101.

The XRD pattern is characterized by significant peaks at low 2θ values (between 3 and 10°).

To obtain information about the porosity, synthesized MIL-101 powders were subjected to microporosimetric analysis by nitrogen adsorption at 77 K using a Micromeritics ASAP 2020 equipment. The results are shown in Figure 5.14.

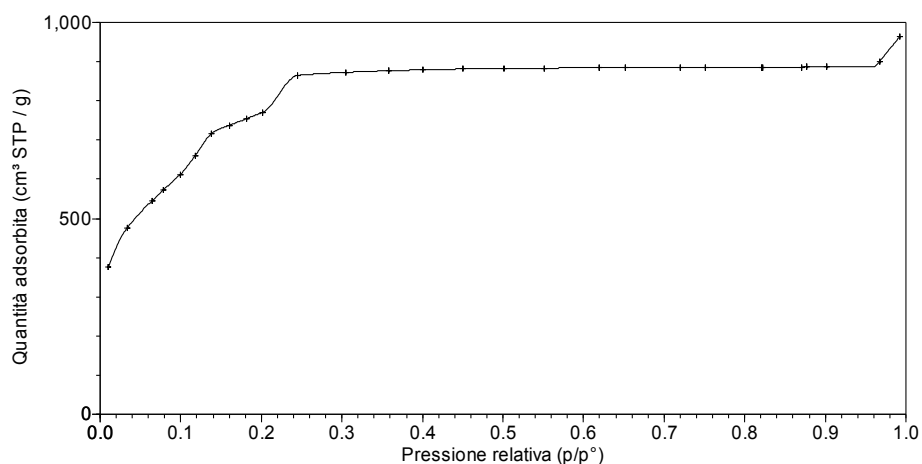


Fig.5.14 Nitrogen adsorption isotherm at 77 K on powders of MIL-101

From obtained experimental data it was possible to determine the specific surface area (equal to about 3000 m²/g, according to the BET model), and the intracrystalline pore volume (equal to 1.37 cm³/g).

2. Adsorption measurement

2.1 Carbon dioxide adsorption on Cu-BTC

Figure 5.15 reports CO₂ adsorption isotherms on Cu-BTC MOF at 283, 293, 318, and 343 K for CO₂ pressures ranging from 0 to 1 bar together with fits to the Sips equation (which will be subsequently analyzed). Figure 5.15 shows that over the pressure range considered, the isotherms are significantly far from their asymptotic maximum

levels and show a strong pressure dependence of the amount of adsorbed CO₂. In regard to the dependence on temperature, it clearly appears that the amount of adsorbed CO₂ decreases as temperature increases, indicating that the adsorption process is exothermic. In particular, at $p = 1$ bar, the adsorbed amount q turned out to be about $7.0 \text{ mol}\cdot\text{kg}^{-1}$ at $T = 283 \text{ K}$ and about $1.5 \text{ mol}\cdot\text{kg}^{-1}$ at $T = 343 \text{ K}$, with a ratio of about 5. It is interesting to note that over the pressure range considered in this work, the amounts of adsorbed CO₂ at 293 K are slightly higher than, for example, those at 298 K reported by Liang and co-workers [278]. Apart from the sensitivity of CO₂ adsorption capacity to temperature, this could be due to the fact that those authors used significantly lower adsorption times for each experimental point (15 to 30 min rather than 1 to 2 h).

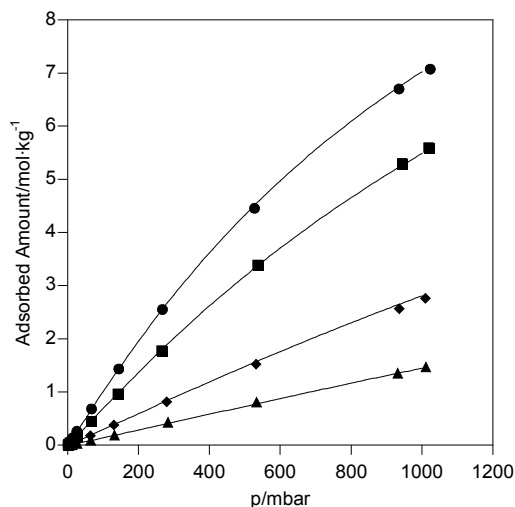


Fig.5.15 CO₂ adsorption isotherms on synthesized Cu-BTC, measured using an ASAP 2020 apparatus: ●, 283 K; ■, 293 K; ◆, 318 K; ▲, 343 K. Continuous lines are best-fit Sips theoretical isotherms.

In order to compare the behavior of Cu-BTC with that of a more traditional microporous adsorbent, CO₂ adsorption isotherms were also determined on 13X zeolite over the same temperature and pressure ranges. The experimental results for 13X zeolite are reported in Figure 5.16 along with fits to the Sips equation. The isotherms reported in Figure 5.16 have a markedly different shape from those reported in Figure 5.15, with a strongly convex behavior. Also for 13X, saturation was not achieved over the pressure range explored, even though inspection of the isotherms reported in Figure 5.16 appears to indicate that saturation should be reached at a pressure much lower than that for Cu-BTC.

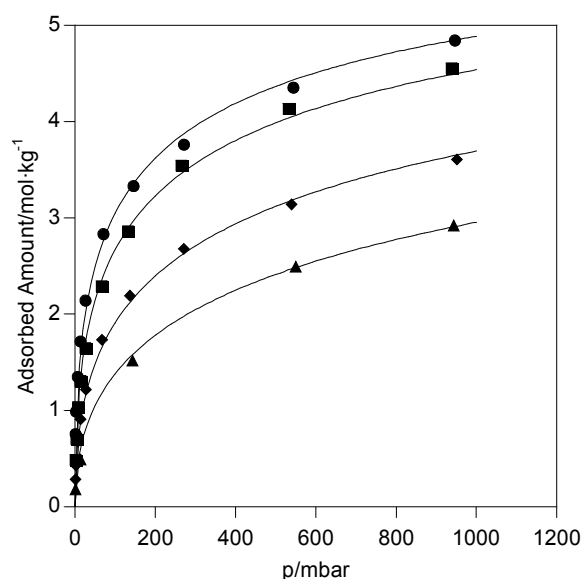


Fig.5.16 CO₂ adsorption isotherms on purchased 13X zeolite, measured using an ASAP 2020 apparatus: ●, 283 K; ■, 293 K; ◆, 318 K; ▲, 343 K. Continuous lines are best-fit Sips theoretical isotherms.

Figure 5.16 shows that the amount of CO₂ adsorbed on 13X zeolite also decreases as the temperature increases, but in a less pronounced way than for Cu-BTC. Indeed, at $p = 1$ bar, the adsorbed amount decreased from about $4.8 \text{ mol}\cdot\text{kg}^{-1}$ at $T = 283 \text{ K}$ to about $2.9 \text{ mol}\cdot\text{kg}^{-1}$ at $T = 343 \text{ K}$, with a ratio of about 1.6. The noticeable difference in the shapes of the CO₂ adsorption isotherms of 13X and Cu-BTC could be due to the different nature of the interactions between CO₂ molecules and the inner micropore walls of such substrates. In fact, in

13X zeolite, adsorption occurs mainly because of the slight acidity of CO₂ molecules, which enables them to interact with the slightly basic inner micropore surfaces of zeolites with a low Si/Al ratio (for 13X zeolite, the ratio is equal to 1.24). On the other hand, the nature of the interaction between CO₂ molecules and the Cu-BTC framework is completely different. In fact, the bonds between metal coordination centers and organic linkers in MOFs usually show a relevant electrostatic factor, with inorganic moieties characterized by partial positive charges. If such positively charged metal coordination centers are exposed at the inner surface of the micropores (in many cases, such as that of Cu-BTC, this can be achieved by water removal from the substrate), they can specifically interact with gas molecules having quadrupole moment different from zero, as in the case of gaseous CO₂ [278, 279]. In order to verify the capability of Cu-BTC samples produced in this work with regard to CO₂ separation from other components of a gas mixture, N₂ adsorption isotherms on both Cu-BTC and 13X at 293 K were obtained. Such isotherms are reported in Figure 5.17, together with the isotherms for CO₂ adsorption on Cu-BTC and 13X at the same temperature. Figure 5.17 shows that both Cu-BTC and 13X have a very low affinity for N₂, with an adsorption

capacity that, at pressures of about 1 bar, is on the order of $0.15 \text{ mol}\cdot\text{kg}^{-1}$, corresponding to a ratio with the similar quantity for CO_2 adsorption of close to 1/30. These results are consistent with what has already been reported by Wang and co-workers [263], who, for example, proposed the usage of Cu-BTC for PSA processes aimed at efficient removal of CO_2 from air prior to its cryogenic distillation.

In order to have a clearer understanding of the adsorption phenomena examined, a modeling effort was undertaken using the semiempirical three-parameter Sips isotherm [280]. The Sips isotherm (sometimes called the Langmuir-Freundlich isotherm) is a semiempirical model that contains mathematical aspects of both the Langmuir and Freundlich isotherms; even though its thermodynamic consistency shows limits in the very low pressure region (it does not reduce to Henry's law), its simple form does not require the definition of the saturation pressure for the adsorbate, thus making it suitable for modeling either subcritical or supercritical isotherms. According to this equation, the pressure dependence of the adsorbed amount takes the following form:

$$1) \quad q = q_{max} \frac{(bp)^{\frac{1}{n}}}{1+(bp)^{\frac{1}{n}}}$$

where q_{max} , n , and b are model parameters: q_{max} represents the maximum adsorption capacity, b is the affinity constant, and n is the heterogeneity coefficient (in particular, for $n = 1$, the Sips isotherm reduces to the Langmuir isotherm, which applies to homogeneous adsorbent-adsorbate systems). Sips parameters are in general dependent on temperature, as reported by Do [281], but considering q_{max} and n to be independent of temperature wherever possible is strongly advisable in order to keep the model describing the system as simple as possible.

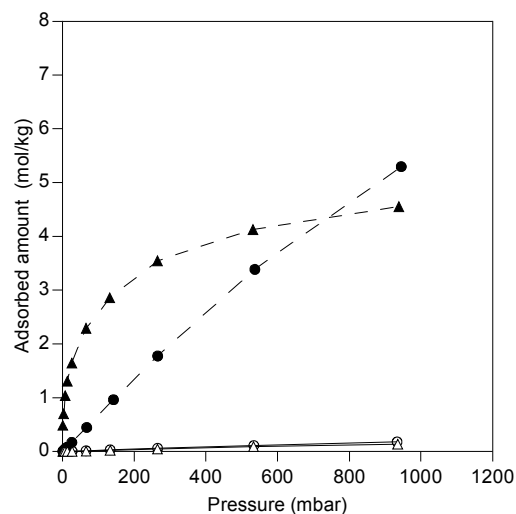


Fig.5.17 Adsorption isotherms of CO₂ (solid symbols, dashed lines) and N₂ (open symbols, continuous lines) on synthesized Cu-BTC (circles) and purchased 13X zeolite (triangles), measured using an ASAP 2020 apparatus at 293 K.

For this reason, an attempt to describe CO₂ adsorption on both Cu-BTC MOF and 13X zeolite was performed by coupling eq 1 with the following expression for the description of the dependence of the affinity coefficient b on temperature [281]:

$$2) \quad b = b_{\infty} \exp \left(\frac{Q}{RT} \right)$$

where b_{∞} is the value of b at infinite temperature and Q is the value of the isosteric heat of adsorption when the adsorbent fractional coverage is equal to 0.5. The experimental data concerning CO₂ adsorption on Cu-BTC and on 13X were submitted to nonlinear regression (using ad hoc scripts developed in the Matlab environment) in order to calculate simultaneously the optimal values of the parameters of eqs 1 and 2 (i.e., q_{max} , b_{∞} , Q , and n) for the isotherms reported in Figures 5.15 and 5.16. The calculated values of the parameters are reported in Tables

5.1 and 5.2, and the comparison between the model and the experimental results has been shown in Figures 5.15 and 5.16, in which symbols refer to experimental data and continuous curves refer to the best-fit Sips theoretical isotherms .

parameter	95% confidence interval		best-fit value	95% confidence interval	
	lower limit			upper limit	
$q_{\max}/\text{mol}\cdot\text{kg}^{-1}$	15.3		16.5		17.7
$b_{\infty}/\text{mbar}^{-1}$	$9.83\cdot 10^{-5}$		$1.25\cdot 10^{-4}$		$1.51\cdot 10^{-4}$
n	0.92		0.94		0.97
$Q/\text{kJ}\cdot\text{mol}^{-1}$	25.5		25.9		26.3

coefficient of determination: $R^2 = 0.999$

Tab.5.1 Sips Parameters for CO₂ Adsorption on Synthesized Cu-BTC

parameter	95% confidence interval		best-fit value	95% confidence interval	
	lower limit			upper limit	
$q_{\max}/\text{mol}\cdot\text{kg}^{-1}$	6.26		7.06		7.85
$b_{\infty}/\text{mbar}^{-1}$	$8.81\cdot 10^{-6}$		$5.59\cdot 10^{-5}$		$1.03\cdot 10^{-4}$
n	1.90		2.12		2.40
$Q/\text{kJ}\cdot\text{mol}^{-1}$	30.8		32.5		34.2

coefficient of determination: $R^2 = 0.971$

Tab.5.2 Sips Parameters for CO₂ Adsorption on Purchased 13X Zeolite.

Inspection of Figures 5.15 and 5.16 clearly indicates a very good correlation between the model curves and the experimental points for both Cu-BTC MOF and 13X zeolite.

This is also confirmed by values of the regression coefficient R^2 reported in Tables 5.1 and 5.2. Furthermore, from the analysis of the data reported in Tables 5.1 and 5.2, it can be noted that the maximum adsorption capacity q_{max} for Cu-BTC is significantly higher than that calculated for 13X zeolite (i.e., $16.5 \text{ mol}\cdot\text{kg}^{-1}$ vs $7.06 \text{ mol}\cdot\text{kg}^{-1}$). It is interesting to observe that the calculated value of q_{max} for Cu-BTC finds a kind of validation from a comparison with the experimental results of Liang and co-workers [278], who, commenting on the circumstance that Cu-BTC adsorbs $12.7 \text{ mol}\cdot\text{kg}^{-1}$ of CO_2 at 298 K and 15 bar, stated that even at such a high pressure, none of the CO_2 adsorption isotherms produced by their experimental runs appeared to have reached saturation.

In regard to the affinity coefficient b , the values of this parameter for both Cu-BTC and 13X can be calculated, for example, at $T = 293 \text{ K}$ by using eq 2 and the values of b_∞ and Q reported in Tables 5.1 and 5.2, respectively. Such values of b turned out to be $5.18\cdot 10^{-4} \text{ mbar}^{-1}$ for Cu-BTC and $3.48\cdot 10^{-3} \text{ mbar}^{-1}$ for 13X, thus indicating that, at ambient temperature, Cu-BTC shows a lower affinity for CO_2 than 13X does. As suggested by Siriwardane and co-workers [282], an empirical assessment of the affinity of an adsorbent for CO_2 can be achieved by

plotting adsorption isotherms as adsorbed amounts per unit area of adsorbent versus gas pressure. Figure 5.18 shows the CO₂ adsorption isotherms on Cu-BTC and 13X zeolite at T = 293 K that were already reported in Figures 5.15 and 5.16, respectively, but this time plotted in terms of adsorbed amounts per unit area.

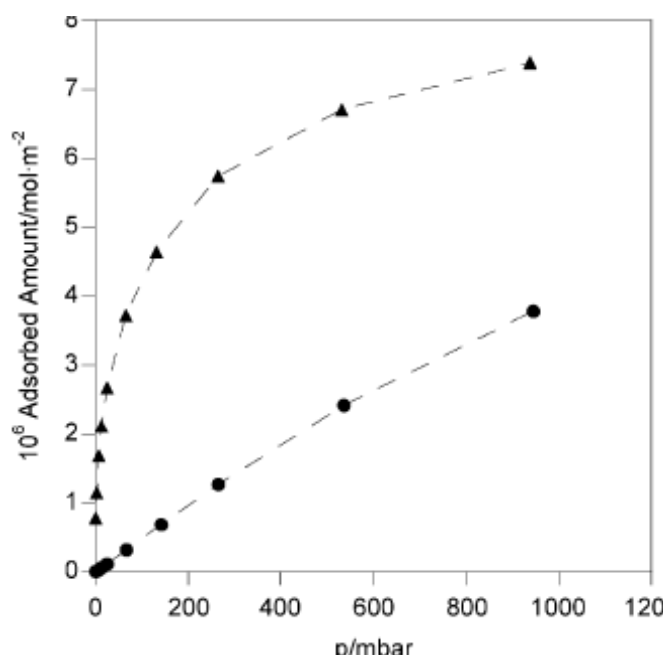


Fig.5.18 Adsorption isotherms of CO₂ at 293 K on synthesized Cu-BTC (●) and purchased 13X zeolite (▲) based on the surface areas of the adsorbents.

Inspection of Figure 5.18 clearly indicates that the number of moles of CO₂ adsorbed per unit area of 13X zeolite is higher than that of Cu-BTC over the considered pressure range.

In turn, this indicates that the surface of 13X zeolite has a better affinity for CO₂ than that of Cu-BTC, thus confirming the results of the modeling process and suggesting that the aforementioned higher CO₂ adsorption capacity per unit mass of Cu-BTC primarily depends not on the interaction between the framework and gas molecules but rather on the higher specific surface area and pore volume that Cu-BTC shows in comparison with 13X zeolite.

In regard to the heterogeneity parameter n , it is practically equal to unity for Cu-BTC, which indicates a homogeneous adsorption system and suggests that for this material the Langmuir model could fit the experimental data quite well; on the other hand, the value of n for 13X is greater than 2, indicating a more pronounced heterogeneity in the adsorption process. As already mentioned in the comments on the experimental results, this difference presumably depends on the different nature of the interactions between CO₂ molecules and the inner micropore walls of the considered substrates. For CO₂ adsorption on 13X zeolite, it is interesting to note that this process partially develops through a chemical reaction that produces carbonate-like species starting from basic framework oxygen atoms and CO₂ molecules polarized by neighboring Na⁺ ions [283].

The value of the isosteric heat of CO₂ adsorption on Cu-BTC (25.9 kJ•mol⁻¹, as reported in Table 5.1) is about 20 % lower than that for CO₂ adsorption on 13X (about 32.5 kJ•mol⁻¹, as reported in Table 5.2). Such results are independent of the adsorbent fractional coverage because the expression for isosteric heat of adsorption derived from the Sips model reduces to the constant Q when the hypothesis of the temperature independence of the heterogeneity parameter n is taken into account [281]. Comparison of the calculated values of Q with the average values of the isosteric heat of adsorption for CO₂ that were experimentally determined and reported in the literature [263, 284] (*i.e.*, about 28 kJ•mol⁻¹ for Cu-BTC and 36 kJ•mol⁻¹ for 13X) shows a satisfactory agreement. Since fixed-bed adsorption is an essentially adiabatic operation, the isosteric heat of adsorption is responsible for the temperature rise during the process. Once the working pressure range is fixed, adsorbent materials used in fixed-bed adsorption processes usually tend to lose part of their adsorption capacity as the working temperature increases. For this reason, a lower isosteric heat of adsorption is preferable when selecting the adsorbents, and because the CO₂ isosteric heat of adsorption for Cu-BTC MOF is clearly lower

than that for 13X zeolite, Cu-BTC should be a more efficient adsorbent than 13X zeolite in fixed-bed adsorption processes.

2.2 Water Vapor Adsorption on Cu-TRZ

Fig. 5.19 reports water vapor adsorption isotherms on the Cu-TRZ-168 sample at 293, 303, 323 and 343 K for water vapor pressures ranging between 0 and 3 kPa, together with fits to the Sips equation. The curves reported in Fig. 5.19 are “type V” isotherms [277], which are typical of water vapor adsorption on both zeolites and activated carbons. The figure shows that, in the pressure range considered, isotherms already reached their maximum adsorption capacity. Surprisingly, the maximum adsorption capacity shown in Fig. 5.19 at 293 K is comparable, if not higher, than the corresponding value derivable from the water vapor adsorption isotherm performed at 273 K by Ouellette and coworkers [264], which can be explained by the difference between the crystallization time of the Cu-TRZ sample used for water vapor adsorption in this work and that of the sample used by the aforementioned authors, who did not prolong the synthesis time of Cu-TRZ over 48 h [264]. The small and morphologically poorly defined crystallites, observed in Fig. 5.7 for a Cu-TRZ sample synthesized during 48 h of hydrothermal treatment, probably lower the

water vapor adsorption capacity with respect to a Cu-TRZ sample composed only of large single crystals and obtained after synthesis times much longer than 48 h. As regards the dependence of the water vapor adsorption capacity of Cu-TRZ-168 on temperature, it clearly appears that the adsorbed amount of water vapor decreases as the temperature increases, indicating exothermic behavior for the adsorption process. In particular, when the maximum adsorption capacity is reached, the adsorbed amount q was approximately 10 mol/kg at $T = 293$ K and approximately 8 mol/kg at $T = 343$ K, with a ratio of roughly 1.25.

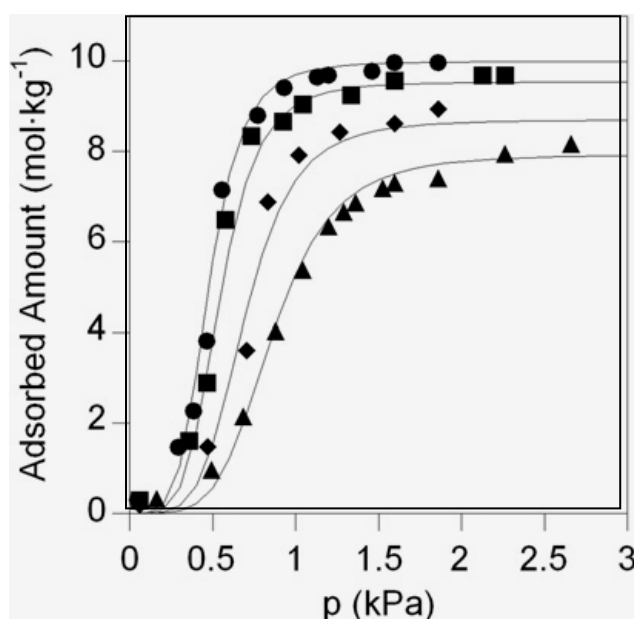


Fig.5.19 Water vapor adsorption isotherms on Cu-TRZ-168, measured by a gravimetric technique based on a McBain-type balance at 293 K (circles), 303 K

(squares), 323 K (diamonds) and 343 K (triangles). Continuous lines: best fitting Sips theoretical isotherms.

For this reason, an attempt to describe the water vapor adsorption on Cu-TRZ-168 was performed by coupling Eq. (1) with the following expressions for the dependence of the affinity coefficient b and the maximum adsorption capacity q_{max} on temperature [281]:

$$3) \quad b = b_0 \exp \left[\frac{Q}{RT} \left(\frac{T_0}{T} - 1 \right) \right]$$

$$4) \quad q_{max} = q_{max,0} \exp \left[\chi \left(1 - \frac{T}{T_0} \right) \right]$$

where b_0 is the value of b at a reference temperature T_0 , Q is a measure of the adsorption heat, $q_{max,0}$ is the maximum adsorption capacity at T_0 , and χ is a constant parameter.

The experimental data regarding water vapor adsorption on Cu-TRZ-168 were submitted to non-linear regression using the MATLAB Surface Fitting Toolbox to simultaneously calculate the

optimal values of the parameters that appear in Eqs. (1), (3) and (4), *i.e.*, $q_{max,0}$, χ , b_0 , Q and n for the isotherms reported in Fig. 5.19.

The calculated values of the parameters, obtained using $T_0 = 293$ K as the reference temperature, are reported in Table 5.3, and the comparison between model and experimental results is reported in Fig. 5.19, in which the symbols refer to experimental data and the continuous curves refer to the best fitting Sips theoretical isotherms. Fig. 5.19 indicates a good correlation between the model curves and experimental points, which is also confirmed by the value of the regression coefficient R^2 reported in Table 5.3.

Parameter	95% confidence interval lower limit	Best fitting value	95% confidence interval upper limit
$q_{max,0}$ (mol kg ⁻¹)	9.698	9.992	10.290
χ	1.028	1.357	1.687
b_0 (kPa ⁻¹)	2.025	2.110	2.195
n	0.186	0.214	0.242
Q (kJ mol ⁻¹)	8.737	10.000	11.260
Regression coefficient $R^2 = 0.986$			

Tab.5.3 Sips parameters for water vapor adsorption on Cu-TRZ-

168.

Using the best fitting values of the Sips parameters reported in Table 5.3, an expression for describing the isosteric heat of adsorption as a

function of the fractional coverage of the adsorbent $\theta = q/q_{max}$ was developed. The isosteric heat of adsorption is the ratio of the infinitesimal change in the adsorbate enthalpy to the infinitesimal change in the amount adsorbed [281]. It is calculated from the following thermodynamic van't Hoff equation:

$$\frac{\Delta H}{RT^2} = - \left(\frac{\partial \ln(p)}{\partial T} \right)_q$$

5)

After rewriting Eq. (1) in terms of p versus q , substituting Eqs. (3), (4) into it and then taking the derivative with respect to T , the following expression for the isosteric heat of adsorption is obtained:

$$-\Delta H = Q + \frac{n\chi RT^2}{T_0} \frac{q_{max}}{q_{max} - q}$$

6)

Writing Eq. (6) in terms of the fractional coverage $\theta = q/q_{\max}$ leads to

$$-\Delta H = Q + \frac{n\chi RT^2}{T_0} \frac{1}{1-\theta}$$

7)

Fig. 5.20 shows the plot of Eq. (7) for $T = 293$ and 343 K using the best fitting values of the parameters χ , Q and n reported in Table 5.3. The plots for $T = 303$ and 323 K, which are between those reported in Fig. 5.20, are omitted for better clarity. The curves in Fig. 5.20 are almost super-imposable, especially in the low fractional coverage range, and are clearly monotonically increasing, suggesting that a higher level of the fractional coverage of the adsorbent leads to a higher development of heat during the adsorption process.

Such behavior is very similar, as example, to that reported for the isosteric heat of CO_2 adsorption on faujasite-type zeolites [285].

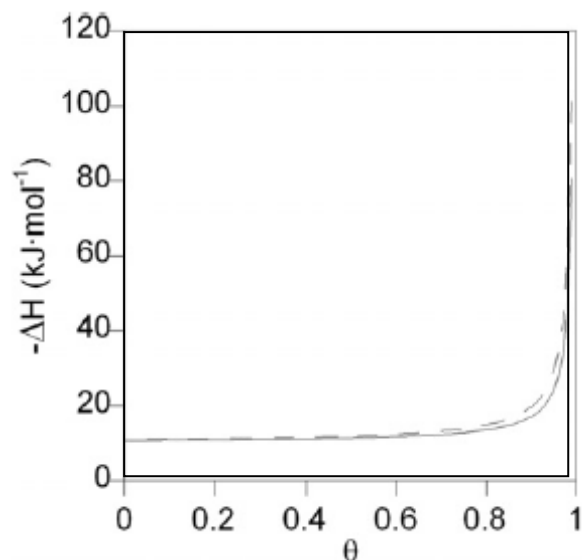


Fig. 5.20 Isosteric heat of water vapor adsorption on Cu-TRZ-168 as a function of the fractional coverage of the adsorbent. Continuous curve: 293 K. Dashed curve: 343 K.

Further inspection of Fig. 5.20 shows that, in the low fractional coverage range, the isosteric heat of adsorption is approximately four times lower than the latent heat of liquefaction of water vapor (as calculated using the data provided by Perry and Green [286]). As stated by Yang [287], for low values of the fractional coverage, the isosteric heat of adsorption at ambient temperature is almost equal to the adsorbate–adsorbent potential, which can be defined as the sum of five main contributions:

$$\varphi = \varphi_D + \varphi_R + \varphi_{Ind} + \varphi_{F\mu} + \varphi_{GQ}$$

8)

In Eq. (8), φ is the adsorbate–adsorbent potential, φ_D is the dispersion energy, φ_R is the close range repulsion energy, φ_{Ind} is the induction energy (the interaction between the electric field of an ion and an induced dipole), φ_{Fl} is the interaction between the electric field of an ion (F) and a permanent dipole (μ), and φ_{GQ} is the interaction between the gradient G of the field F and a quadrupole (with quadrupole moment Q).

In the case of water vapor adsorption on Cu-TRZ, the last three contributions that appear on the right-hand side of Eq. (8) may be considered negligible: in fact, contrary to the case of adsorbents such as zeolites, in the structure of the aforementioned MOF, there are no extrareticular ions that can generate a significant electric field.

Moreover, the contribution φ_{GQ} may be considered negligible for every adsorption system in which water vapor is the selected adsorbate because of the negligible quadrupole moment of its molecules [287].

For these reasons, the adsorbate–adsorbent potential relative to water

vapor adsorption on Cu-TRZ may be reduced to the sum of the two contributions φ_D and φ_R , which have opposite signs and are usually considered “nonspecific” [287]. Applying the aforementioned equivalence between isosteric heat and adsorbate–adsorbent potential to typical water vapor adsorbents such as zeolitic materials [288], it can be noted that, in this case, φ is several times higher than in the case of Cu-TRZ, which consequently develops only weak interactions with adsorbate molecules.

2.3 Hydrogen adsorption on Cu-BTC and MIL-101

2.3.1 Hydrogen Adsorption in Static Volumetric Conditions

Figure 5.21 shows the hydrogen adsorption isotherm at 296 K on Cu-BTC obtained using an HPVA analyzer (static-volumetric technique). It can be seen that the pressure dependence of the amount of adsorbed hydrogen is almost linear. Furthermore, the fact that the curve of Figure 5.21 shows no signs of moving towards an asymptotic value of the amount of adsorbed hydrogen suggests the possibility of further increasing the hydrogen stored by further increases in pressure or, alternatively, by decreases in temperature.

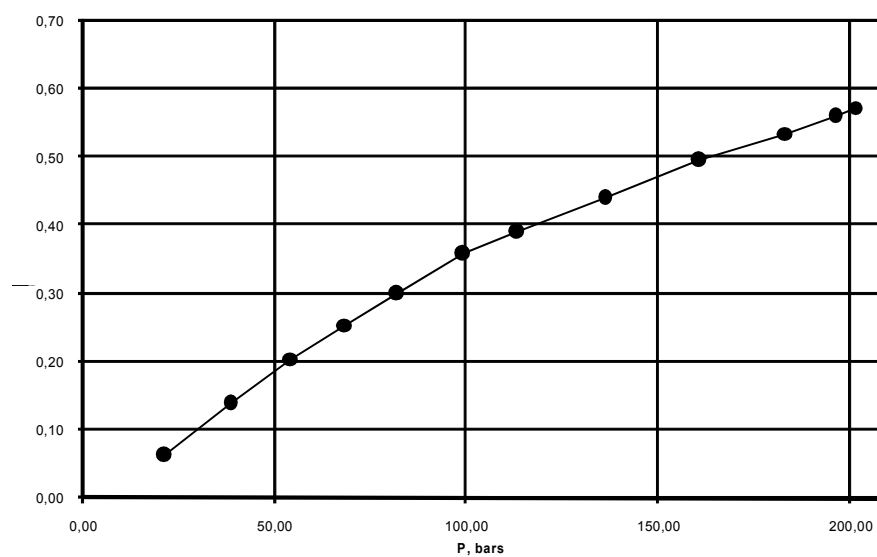


Fig.5.21 Hydrogen adsorption isotherm at 296 K on Cu-BTC.

Since the instrumentation does not permit to determine the experimental points of the isotherm for pressures greater than 200 bar, the determination of the maximum hydrogen adsorption capacity for Cu-BTC was performed measuring the adsorption isotherm at 77 K, as shown in Figure 5.22.

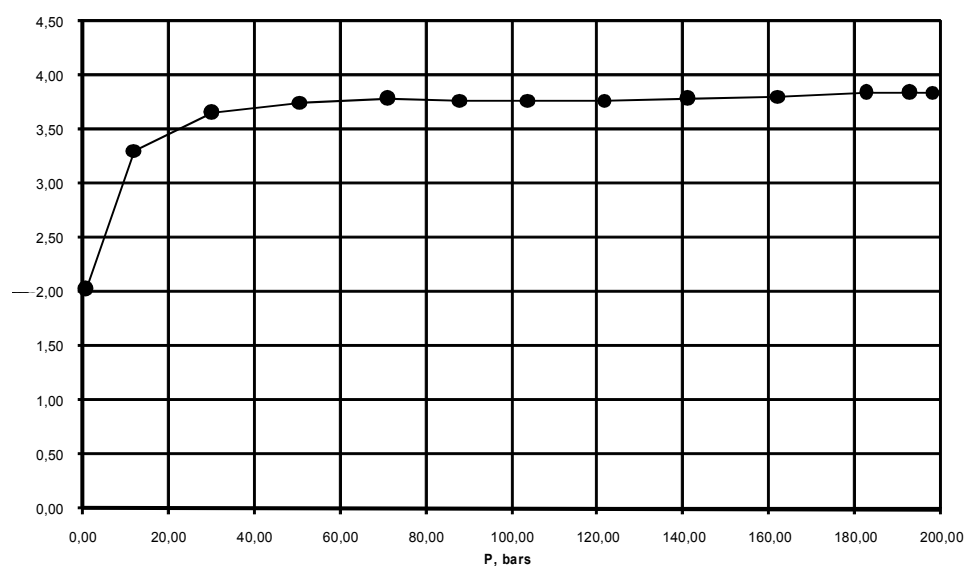


Fig.5.22 Hydrogen adsorption isotherm at 77 K on Cu-BTC.

In this case, it is clear that Cu-BTC has reached its maximum hydrogen adsorption capacity, estimated at approximately 3.5% by weight. Operating at a temperature of 77 K, this value is already reached for pressures below 80 bar. The experimental data shown in Figures 5.21 and 5.22 are remarkably consistent with those found in the literature [289].

Figure 5.23 shows the hydrogen adsorption isotherm at 77 K on MIL-101, obtained using an HPVA analyzer (static-volumetric technique).

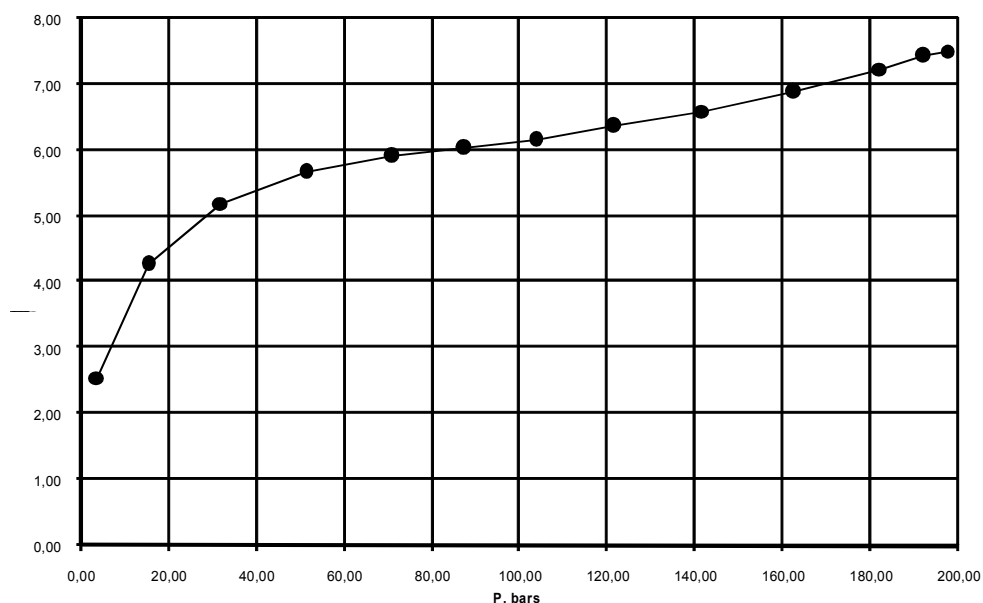


Fig.5.23 Hydrogen adsorption isotherm at 77 K on MIL-101.

As in the case of Cu-BTC, there was also an attempt to detect the adsorption isotherm of hydrogen at room temperature: in this case, there has been no significant adsorption phenomena in the whole pressure range considered (0-200 bar). Compared to what, however, reported in the literature regarding the adsorption of hydrogen at 77 K [290], extending the range of considered pressures over 80 bar has allowed to detect previously unregistered hydrogen adsorption phenomena on MIL-101. In fact, below 80 bar, the isothermal curve seems to approach an asymptotic value of the hydrogen adsorbed amount at about 6% by weight, but, actually, it shows an inflection

point at about 90 bar, beyond which the amount of hydrogen adsorbed starts to vary in an almost linear way with respect to pressure. It is not then possible to experimentally estimate the maximum hydrogen adsorption capacity of MIL-101 if pressure values significantly in excess of 200 bar are not considered. The adsorption capacity estimated at the last pressure value reported in Figure 5.24 turns out to be approximately 7.5% by weight. By limiting the examination of figure 5.23 to pressures below 80 bar, there has been significant consistence with the literature data [290]. These data, however, refer to MIL-101 samples that were obtained by a synthesis process more complex than that reported in this defense, the results of which might help to deepen the knowledge concerning the possible use of MIL-101 as an adsorbent for hydrogen storage.

2.3.2 Hydrogen Adsorption in Dynamic Conditions

Figure 5.24 shows the time profiles of hydrogen concentration at the exit of the reactor described in Chapter IV for the reactor without sorbent, and for the MIL-101-loaded-system at two different values of the hydrogen pressure used during the charging step. The effect of pressure on the hydrogen release capacity of MIL-101 is clearly

evidenced; in particular, during the run at 2 bar, the decrease in H₂ concentration due to dilution with the carrier gas was much slower, showing the effect of the presence of H₂ in the desorbed gas stream.

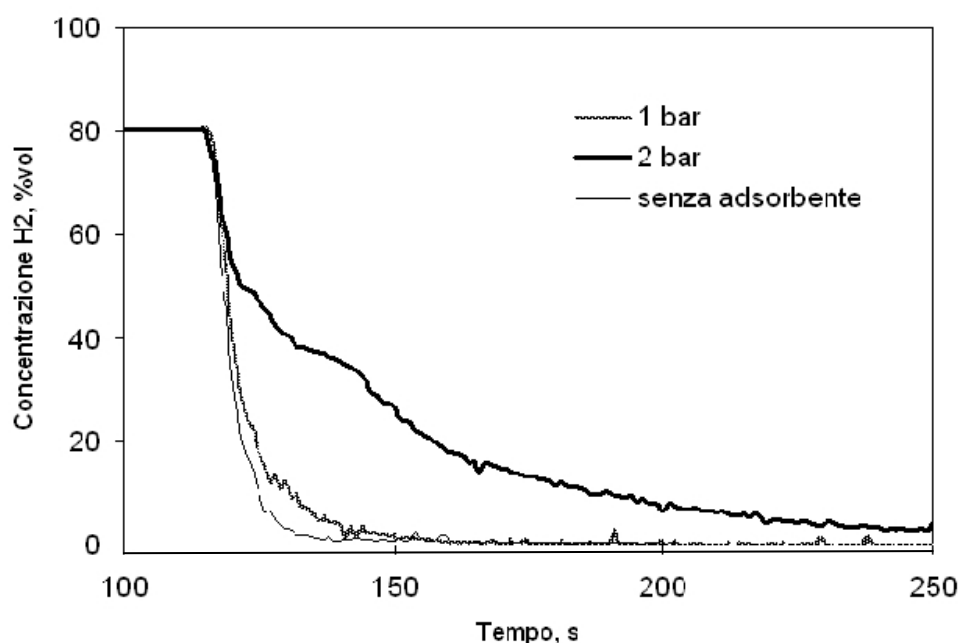


Fig.5.24 Time profiles of hydrogen concentration at the exit of the reactor for the reactor without sorbent, and for the MIL-101-loaded-system at two different values of the hydrogen pressure used during the charging step.

Figure 5.25 shows the flow of hydrogen desorbed from MIL-101 as a function of time for the two working pressures investigated. The areas under the two curves represent the adsorption capacity of the sample at 77 K (0.2% by weight at 1 bar, and 1.4% by weight at 2 bar of H₂). The significant increase in the adsorption capacity at 2 bar, together with the detection of a release kinetics that might be considered

favorable for application on vehicles, suggests to explore the effect of higher pressure values, but still compatible with the declared requirements of the application (5-50 bar).

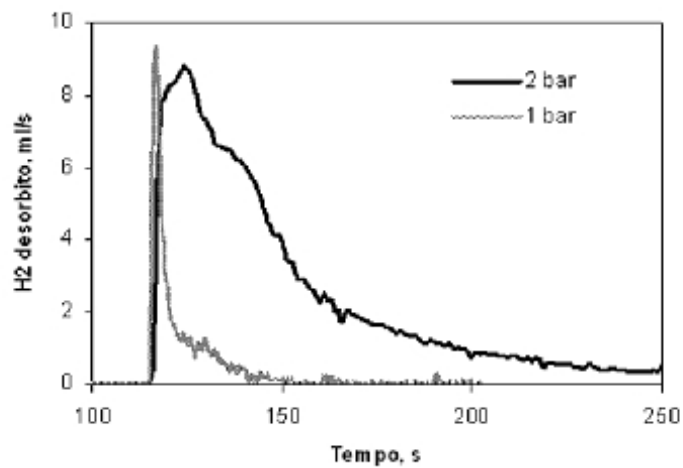


Fig.5.25 Flow of hydrogen desorbed from MIL-101 as a function of time for 1 and 2 bar of H₂ pressure.

Chapter VI

Summary and final evaluations

1. Introduction

The experimental activity carried-out for the realization of this defense has been finalized to the synthesis and characterization of metal-organic framework materials of last generation for a possible use in the field of renewable energy.

In particular, after a careful analysis of scientific literature on the topic, the following three MOF terms has been identified:

- Cu-BTC;
- Cu-TRZ;
- MIL-101;

to be tested in hydrogen storage, the capture of CO₂ and water vapor adsorption (for solar cooling).

Samples of these materials have been synthesized by hydrothermal treatment and subsequently characterized by means of X-ray diffraction, thermogravimetry, and microporosimetric analysis.

A comparison with more traditional zeolite-type materials has also been made.

2. Carbon Dioxide adsorption

CO₂ adsorption on the Cu-BTC metal-organic framework was modeled with the aim of comparing the performance of this material with that of 13X zeolite, which is often used for this application.

Laboratory-synthesized Cu-BTC samples were characterized by means of X-ray diffraction, thermogravimetry, and microporosimetric analysis, which indicated that the samples possess high crystallinity and high specific surface area and pore volume and that they are thermally stable up to 550 K.

CO₂ adsorption isotherms on Cu-BTC were evaluated at T= (283, 293, 318, and 343) K for p ≤ 1 bar.

For comparison, CO₂ adsorption isotherms on samples of commercial 13X zeolite were also determined under the same experimental conditions.

Additionally, the N₂ adsorption isotherms both on Cu-BTC and on 13X zeolite were determined at T=293 K, again for p ≤ 1 bar.

The experimental data showed that both adsorbents possess a high selectivity toward CO₂; moreover, Cu-BTC was found to have a higher CO₂ adsorption capacity than 13X in the range of near-ambient temperatures.

The semiempirical Sips model was used to describe the data obtained for both sorbents, and a good agreement between the model and the experimental results was obtained. The model and the experimental results indicated that Cu-BTC has a noticeably higher adsorption

capacity toward CO₂ than 13X zeolite and that its isosteric heat of adsorption is lower, suggesting that Cu-BTC could be more suitable for fixed-bed adsorption applications than 13X.

3. Water Vapor Adsorption

A deep investigation of the synthesis process and water vapor adsorption behavior of a microporous MOF with the formula [Cu^{II}₃(triazolate)₃(OH)₃(H₂O)₄] \cdot 4.5H₂O (Cu-TRZ) was successfully performed.

Combined XRD, SEM and particle size investigations showed that the products obtained using synthesis times up to the value reported in the literature (48 h) are characterized by the coexistence of significantly inhomogeneous crystallites in terms of size and morphology.

Moreover, prolonging the synthesis time to 168 h revealed a peculiar phenomenon in which very large Cu-TRZ single crystals grow at expense of the smaller ones.

In addition, water vapor adsorption isotherms on large single crystals of Cu-TRZ at four different temperatures were successfully modeled using the semiempirical Sips equation. The modeling could determine the isosteric heat of adsorption as a function of the fractional coverage of the adsorbent.

The very low values that were found for the isosteric heat of adsorption could be related to the absence of strong interactions between water molecules and the framework of Cu-TRZ.

4. Hydrogen storage

In general the results of research conducted within the project greatly helped to deepen the knowledge on the use of nanostructured adsorbent materials of last generation for the development of H₂ storage systems onboard fuel cell vehicles, knowledge that can be developed further in the coming years.

The adsorbent materials with metal-organic framework structures have provided valuable capacity values of adsorption of H₂ at low temperatures (77 K) both in static conditions (3.7% by weight to 50 bar on Cu-BTC and 6% and 7.5% by weight, respectively at 90 and 200 bar, on MIL-101) and under dynamic conditions (about 2% weight of MIL-101 at 2 bar), with favorable release kinetics for the application in the field of hydrogen storage for automotive application.

5. Conclusions and perspectives

The great quantity of studies about Metal Organic Frameworks demonstrates that the properties of MOFs can be exploited in an incredible range of important applications, with potential implications for fields ranging from analytical chemistry to drug delivery, gas storage and applications in the green energy industry.

Nevertheless, these developments are still in their early stages.

Nowadays, MOF science is largely the domain of synthetic chemists. While their work is producing an ever-increasing number of new terms, it is also important that scientists outside the field of synthetic chemistry apply their tools and expertise to build the fundamental and

practical knowledge base required to bring these versatile materials from the laboratory into the realm of actual use.

For example, aspects such as the fundamental origins of energy transfer within MOFs, their long-term stability, defects, and electrical and mechanical properties have received almost no attention.

Practical large-scale synthetic methods must also be developed: in particular, efforts must be focused on the possibility to obtain MOFs with higher and higher specific surface areas, through chemical treatments that require lower temperatures and synthesis times, but, above all, cheaper and non-toxic reactants. In fact, one of the biggest limit for the industrial application of MOFs relies in their high production costs: if thought to be used in the green energy field, for examples, these materials will represent an absurd until the use of expensive toxic reactants and high energy-demanding treatments is needed for their production.

For some years, MOFs were supposed to represent the best answer to the challenge issued by the US DoE on hydrogen storage. At the present time, the hydrogen adsorption capacity of some MOFs at 77 K is quite good, but the constraints that low operating temperatures impose to the overall system requirements are almost unsustainable, especially for automotive applications. Moreover, the suggested heat of adsorption required for ambient temperature adsorption is 15 kJ·mol⁻¹: certain MOFs are capable to develop 5-10 kJ·mol⁻¹ [291], but, at the best of our knowledge, not more.

Changing the chemical composition of the solid to include sites that interact strongly with hydrogen (or other gas molecules) must be more accurately investigated, in order to impact the adsorption capacity at moderate pressures.

Another issue is speeding up and controlling the adsorption/desorption kinetics, which is a critical aspect also for other applications, *e.g.* in biomedicine.

It is therefore clear that, although more than fifteen years have passed since the first MOF was described, there are still many opportunities to conduct influential science and engineering with respect to this fast-growing category of unique materials.

References

- [1] G. Férey, in: R. Xu, J. Chen, Z. Gao, W. Yan (Eds.), *From Zeolites to Porous MOF Materials. The 40th Anniversary of International Zeolite Conference*, Stud. Surf. Sci. Catal. 170, 2007, 66–84.
- [2] U. Mueller, M. Schubert, *J. Mater. Chem.* 16, 2006, 626–636.
- [3] J. Rowsell, O. Yaghi, *Micropor Mesopor Mat.* 73, 2004, 3–14.
- [4] (a) D. Farrusseng, S. Aguado and C. Pinel, *Angew. Chem., Int. Ed.*, 2009, 48, 7502; (b) J. Y. Lee, O. K. Farha, J. Roberts, K. A. Scheidt, S. B. T. Nguyen and J. T. Hupp, *Chem. Soc. Rev.*, 2009, 38, 1450; (c) L. Ma, C. Abney and W. Lin, *Chem. Soc. Rev.*, 2009, 38, 1248; (d) L. Ma and W. Lin, *Top. Curr. Chem.*, 2010, 293, 175; (e) K. Kim, M. Banerjee, M. Yoon and S. Das, *Top. Curr. Chem.*, 2010, 293, 115.
- [5] (a) X. Lin, N. R. Champness and M. Schröder, *Top. Curr. Chem.*, 2010, 293, 35; (b) L. J. Murray, M. Dinca and J. Long, *Chem. Soc. Rev.*, 2009, 38, 1294; (c) A. U. Czaja, N. Trukhan and U. Müller, *Chem. Soc. Rev.*, 2009, 38, 1284; (d) T. Düren, Y. S. Bae and R. Q. Snurr, *Chem. Soc. Rev.*, 2009, 38, 1237.
- [6] (a) F. Schröder and R. A. Fischer, *Top. Curr. Chem.*, 2010, 293, 77; (b) M. Meilikhov, K. Yushenko, A. Torrisi, B. Jee, C. Mellot-Draznieks, A. Pöppel and R. A. Fischer, *Angew. Chem., Int. Ed.*, 2010, 49, 6212; (c) F. Schröder, D. Esken, M. Cokoja, M. W. E. van den Berg, O. I. Lebedev, G. Van Tendeloo, B. Walaszek, G. Buntkowsky, H.-H. Limbach, B. Chaudret and R. A. Fischer, *J. Am. Chem. Soc.*, 2008, 130, 6119; (d) S. Hermes, M. Schröder, R.

Schmid, L. Khodeir, M. Muhler, A. Tissler, R. W. Fischer and R. A. Fischer, *Angew. Chem., Int. Ed.*, 2005, 44, 6237.

[7] (a) D. Zacher, O. Shekhah, C. Wöll and R. A. Fischer, *Chem. Soc. Rev.*, 2009, 38, 1418; (b) O. Shekhah, H. Wang, D. Zacher, R. A. Fischer and C. Wöll, *Angew. Chem., Int. Ed.*, 2009, 48, 5038; (c) O. Shekhah, H. Wang, M. Paradinas, C. Ocal, B. Schüpbach, A. Terfort, D. Zacher, R. A. Fischer and C. Wöll, *Nat. Mater.*, 2009, 8, 481.

[8] See the issue N° 5 of the 38th volume of the Chemical Society Reviews (2009).

[9] F. A. Cotton, C. A. Murillo, R. A. Walton, *Multiple Bonds Between Metal Atoms*, 3rd ed., Springer Science and Business Media, Inc., New York, 2005.

[10] DM Brink, E Boeker, *Nuclear Physics A*, 1967, 91, 1.

[11] Z. Wang, V. C. Kravtsov, R. B. Walsh and M. J. Zaworotko, *Cryst. Growth Des.*, 2007, 7, 1154.

[12] S. S.-Y. Chui, S. M.-F. Lo, J. P. H. Charmant, A. G. Orpen and I. D. Williams, *Science*, 1999, 283, 1148.

[13] H. Li, M. Eddaoudi, T. L. Groy and O. M. Yaghi, *J. Am. Chem. Soc.*, 1998, 120, 8571.

[14] (a) F. A. Cotton, J. P. Donahue, C. Lin and C. A. Murillo, *Inorg. Chem.*, 2001, 40, 1234; (b) M. H. Chisholm and A. M. Macintosh, *Chem. Rev.*, 2005, 105, 2949.

- [15] F. A. Cotton, C. Lin and C. A. Murillo, *Inorg. Chem.*, 2001, 40, 472.
- [16] F. A. Cotton, Y. Kim, D. L. Shulz, *Inorg. Chim. Acta*, 1995, 236, 43.
- [17] J. S. Miller, (Ed.), *Extended Linear Chain Compounds*, Vol. 1, 1982.
- [18] J. S. Valentine, A. J. Silverstein, Z. G. Soos, *J. Am. Chem. Soc.*, 1974, 96, 97.
- [19] B. Morosin, R. C. Hughes, Z. G. Soos, *Acta Crystallogr., Sect. B: Struct. Crystallogr. Cryst. Chem.*, 1975, B31, 762.
- [20] F. A. Cotton and T. R. Felthouse, *Inorg. Chem.*, 1980, 19, 328.
- [21] M. C. Kerby, B.W. Eichhorn, J. A. Creighton and K. P. C. Vollhardt, *Inorg. Chem.*, 1990, 29, 1319.
- [22] S. P. Perlepes, E. Libby, W. E. Streib, K. Folting and G. Christou, *Polyhedron*, 1992, 11, 923.
- [23] E. F. Day, J. C. Huffman, K. Folting and G. Christou, *J. Chem. Soc., Dalton Trans.*, 1997, 2837.
- [24] W. Frank, V. Reilandand and G. J. R., *Angew. Chem., Int. Ed.*, 1998, 37, 2983.
- [25] W.-M. Xue, F. E. Kühn, E. Herdtweck and Q. Li, *Eur. J. Inorg. Chem.*, 2001, 213.
- [26] W.-M. Xue, F. E. Kühn and E. Herdtweck, *Polyhedron*, 2001, 20, 791.

- [27] J. Pansanel, A. Jouaiti, S. Ferlay, M. W. Hosseini, J.-M. Planeix and N. Kyritsakas, *New J. Chem.*, 2006, 30, 683.
- [28] P. D. C. Dietzel, R. Blom and H. Fjellvag, *Dalton Trans.*, 2006, 586.
- [29] J. Moncol, M. Mudra, P. Lönnecke, M. Hewitt, M. Valko, H. Morris, J. Svorec, M. Melnik, M. Maz'ur and M. Koman, *Inorg. Chim. Acta*, 2007, 360, 3213.
- [30] S. Youngme, A. Cheansirisomboon, C. Danvirutai, C. Pakawatchai and N. Chaichit, *Inorg. Chem. Commun.*, 2008, 11, 57
- [31] L. K. Knight, V. N. Vukotic, E. Viljoen, C. B. Caputo and S. J. Loeb, *Chem. Commun.*, 2009, 5585.
- [32] J. Moncol, Z. Vasková, P. Stachov'a, J. Svorec, R. Sillanpää, M. Maz'ur and D. Valigura, *J. Chem. Crystallogr.*, 2010, 40, 179; J. Moncol, M. Mudra, P. Lönnecke, M. Hewitt, M. Valko, H. Morris, J. Svorec, M. Melnik, M. Maz'ur and M. Koman, *Inorg. Chim. Acta*, 2007, 360, 3213.
- [33] L.-Q. Yu, R.-D. Huang, Y.-Q. Xu, T.-F. Liu, W. Chu and C.-W. Hu, *Inorg. Chim. Acta*, 2008, 361, 2115.
- [34] X. Zhu, J. Lü, X. Li, S. Gao, G. Li, F. Xiao and R. Cao, *Cryst. Growth Des.*, 2008, 8, 1897.
- [35] Q. Shi, Y. Sun, L. Sheng, K. Ma, X. Cai and D. Liu, *Inorg. Chim. Acta*, 2009, 362, 4167.

- [36] E. Whelan, M. Devereux, M. McCann and V. McKee, *Chem. Commun.*, 1997, 427.
- [37] F. A. Cotton, C. Lin and C. A. Murillo, *Inorg. Chem.*, 2001, 40, 575.
- [38] F. A. Cotton, C. Lin and C. A. Murillo, *Acc. Chem. Res.*, 2001, 34, 759.
- [39] M. Köberl, M. Cokoja, W. A. Herrmannb, F. E. Kühn, *Dalton Trans.*, 2011, 40, 6834.
- [40] F. A. Cotton, L. M. Daniels, C. Lin and Carlos A. Murillo, *J. Am. Chem. Soc.*, 1999, 121, 4538.
- [41] F. A. Cotton, C. Lin and C. A. Murillo, *Inorg. Chem.*, 2001, 40, 478.
- [42] R. P. Bonar-Law, T.D. McGrath, N. Singh, J.F. Bickley, A. Steiner, *Chem. Commun.*, 1999, 2457.
- [43] J. F. Bickley, R. P. Bonar-Law, C. Femoni, E. J. MacLean, A. Steiner and S. J. Teat, *J. Chem. Soc., Dalton Trans.*, 2000, 4025.
- [44] M. Eddaoudi, J. Kim, D. Vodak, A. Sudik, J. Wachter, M. O’Keeffe and O. M. Yaghi, *Proc. Natl. Acad. Sci. U. S. A.*, 2002, 99, 4900.
- [45] T. A. Stephenson, E. Bannister and G. Wilkinson, *J. Chem. Soc. A*, 1964, 2538.
- [46] W. Mori and S. Takamizawa, *J. Solid State Chem.*, 2000, 152, 120.

- [47] S. A. Bourne, J. Lu, A. Mondal, B. Moulton and M. J. Zaworotko, *Angew. Chem., Int. Ed.*, 2001, 40, 211; H. Abourahma, G. J. Bodwell, J. Lu, B. Moulton, I. R. Pottie, R. B. Walsh and M. J. Zaworotko, *Cryst. Growth Des.*, 2003, 3, 513; Z. Wang, V. C. Kravtsov, R. B. Walsh and M. J. Zaworotko, *Cryst. Growth Des.*, 2007, 7, 1154.
- [48] K. O. Kongshaug and H. J. Fjellvåg, *J. Solid State Chem.*, 2002, 166, 213.
- [49] J. Tao, X. Yin, R. Huang, L. Zheng and S. N. Weng, *Inorg. Chem. Commun.*, 2002, 5, 975.
- [50] R. Wang, M. Hong, D. Yuan, Y. Sun, L. Xu, J. Luo, R. Cao, A. S. C. Chan, *Eur. J. Inorg. Chem.*, 2004, 37; R. Wang, L. Han, F. Jiang, Y. Zhou, D. Yuan and M. Hong, *Cryst. Growth Des.*, 2005, 5, 129.
- [51] D. J. Xu, L. Pan, T. J. Emge, X. Y. Huang and J. Li, *Acta Crystallogr., Sect. C: Cryst. Struct. Commun.*, 2006, C62, m150.
- [52] D. X. Xue, Y. Y. Lin, X.N. Chen and X.M. Chen, *Cryst. Growth Des.*, 2007, 7, 1332.
- [53] X. F. Wang, Y. B. Zhang, H. Huang, J. P. Zhang and X. M. Chen, *Cryst. Growth Des.*, 2008, 8, 4559.
- [54] C. C. Tsai, T. T. Luo, J. F. Yin, H. C. Lin and K. L. Lu, *Inorg. Chem.*, 2009, 48, 8650.
- [55] L. Han, Y. Zhou, W. N. Zhao, X. Li and Y. X. Liang, *Cryst. Growth Des.*, 2009, 9, 660.

- [56] W. Yang, X. Lin, A. J. Blake, C. Wilson, P. Hubberstey, N. R. Champness and M. Schröder, *Inorg. Chem.*, 2009, 48, 11067.
- [57] L. F. Ma, B. Liu, L. Y. Wang, C. P. Li and M. Du, *Dalton Trans.*, 2010, 39, 2301.
- [58] (a) P. Kanoo, K. L. Gurunatha and T. K. Maji, *J. Mater. Chem.*, 2010, 20, 1322; (b) P. Kanoo, R. Matsuda, M. Higuchi, S. Kitagawa, T. K. Maji, *Chem. Mater.*, 2009, 21, 5860.
- [59] X. Z. Wang, D. R. Zhu, Y. Xu, J. Yang, X. Shen, J. Zhou, N. Fei, X. K. Ke and L. M. Peng, *Cryst. Growth Des.*, 2010, 10, 887.
- [60] W. Mori, S. Takamizawa, *J. Solid State Chem.*, 2000, 152, 120.
- [61] W. Mori, S. Takamizawa, C. N. Kato, T. Ohmura, T. Sato, *Microporous Mesoporous Mater.*, 2004, 73, 31.
- [62] E. Y. Choe, P. M. Barron, R. W. Novotny, H. T. Son, C. Hu and W. Choe, *Inorg. Chem.*, 2009, 48, 426.
- [63] P. M. Barron, H. T. Son, C. Hu and W. Choe, *Cryst. Growth Des.*, 2009, 9, 1960.
- [64] H. Chung, P. M. Barron, R. W. Novotny, H. T. Son, C. Hu and W. Choe, *Cryst. Growth Des.*, 2009, 9, 3327.
- [65] S. R. Batten, B. F. Hoskins, B. Moubaraki, K. S. Murray and R. Robson, *Chem. Commun.*, 2000, 1095.
- [66] T. Ohmura, A. Usuki, K. Fukumori, T. Ohta, M. Ito and K. Tatsumi, *Inorg. Chem.*, 2006, 45, 7988.

- [67] L. F. Xu, X. L. Chen, H. M. Hu and B. C. Wang, *J. Mol. Struct.*, 2008, 892, 163.
- [68] H. Miyasaka, N. Motokawa, S. Matsunga, M. Yamashita, K. Sugimoto, T. Mori, N. Toyota and K. R. Dunbar, *J. Am. Chem. Soc.*, 2010, 132, 1532.
- [69] C. Z. Zhang, H. Y. Mao, Y. L. Wang, H. Y. Zhang and J. C. Tao, *J. Phys. Chem. Solids*, 2007, 68, 236.
- [70] E. Y. Choi, P. M. Barron, R. W. Novotny, C. Hu, Y. U. Kwon and W. Choe, *CrystEngComm*, 2008, 10, 824.
- [71] D. J. Tranchemontagne, Z. Ni, M. O’Keeffe and O.M. Yaghi, *Angew. Chem., Int. Ed.*, 2008, 47, 5136.
- [72] M. Jaya Prakash, M. Oh, X. Liu, K. N. Han, G. H. Seong and M. S. Lah, *Chem. Commun.*, 2010, 46, 2049.
- [73] J.-R. Li, A. A. Yakovenko, W. Lu, D. J. Timmons, W. Zhuang, D. Yuan and H.-C. Zhou, *J. Am. Chem. Soc.*, 2010, 132, 17599, DOI: 10.1021/ja1080794.
- [74] X. Song, X. Liu, M. Oh and M. S. Lah, *Dalton Trans.*, 2010, 39, 6178.
- [75] F. A. Cotton, L. M. Daniels, C. Lin and C. A. Murillo, *Chem. Commun.*, 1999, 841.
- [76] F. A. Cotton, C. Lin and C. A. Murillo, *Inorg. Chem.*, 2001, 40, 6413.

- [77] F. A. Cotton, P. Lei, C. Lin, C. A. Murillo, X. Wang, S.-Y. Yu and Z.-X. Zhang, *J. Am. Chem. Soc.*, 2004, 126, 1518.
- [78] H.-F. Zhu, J. Fan, T. Okamura, Z.-H. Zhang, G.-X. Liu, K.-B. Yu, W.-Y. Sun and N. Ueyama, *Inorg. Chem.*, 2006, 45, 3941.
- [79] Z. Ni, A. Yassar, T. Antoun and O. M. Yaghi, *J. Am. Chem. Soc.*, 2005, 127, 12752.
- [80] M. Jaya Prakash, Y. Zou, S. Hong, M. Park, M.-P. Ngoc Bui, G. H. Seong and M. S. Lah, *Inorg. Chem.*, 2009, 48, 1281.
- [81] M. Jaya Prakash and M. S. Lah, *Chem. Commun.*, 2009, 3326.
- [82] M. Eddaoudi, J. Kim, J. B. Wachter, H. K. Chae, M. O'Keeffe and O. M. Yaghi, *J. Am. Chem. Soc.*, 2001, 123, 4368.
- [83] D. Zhao, D. Yuan, R. Krishna, J. M. van Baten and H.-C. Zhou, *Chem. Commun.*, 2010, 46, 7352
- [84] J.-R. Li and H.-C. Zhou, *Nat. Chem.*, 2010, 2, 893.
- [85] H. Furukawa, J. Kim, K. E. Plass and O. M. Yaghi, *J. Am. Chem. Soc.*, 2006, 128, 8398.
- [86] J. J. Perry, J. A. Perman and M. J. Zaworotko, *Chem. Soc. Rev.*, 2009, 38, 1400.
- [87] G. Férey, C. Mellot-Draznieks, C. Serre, F. Millange, J. Dutour, S. Surblé and I. Margiolaki, *Science*, 2005, 309, 2040.
- [88] B. Moulton, J. Lu, A. Mondal and M. J. Zaworotko, *Chem. Commun.*, 2001, 863.

[89] (a) D. J. Tranchemontagne, J. L. Mendoza-Cortés, M. O’Keeffe and O. M. Yaghi, *Chem. Soc. Rev.*, 2009, 38, 1257; (b) O. M. Yaghi, M. O’Keeffe, N. W. Ockwig, H. K. Chae, M. Eddaoudi and J. Kim, *Nature*, 2003, 403, 705; (c) M. Eddaoudi, D. B. Moler, H. Li, B. Chen, T. M. Reineke, M. O’Keeffe and O.M. Yaghi, *Acc. Chem. Res.*, 2001, 34, 319; (d) G. Férey, *Chem. Soc. Rev.*, 2008, 37, 191; (e) S. Kitagawa, R. Kitaura and S. Noro, *Angew. Chem., Int. Ed.*, 2004, 43, 2334; (f) C. N. R. Rao, S. Natarajan and R. Vaidhyanathan, *Angew. Chem., Int. Ed.*, 2004, 43, 1466; (g) S. I. Vagin, A.K. Ott and B. Rieger, *Chem. Ing. Tech.*, 2007, 79, 767.

[90] F. A. Cotton and K. J. Wiesinger, *Inorg. Chem.*, 1991, 30, 871.

[91] (a) K. Seki, S. Takamizawa and W. Mori, *Chem. Lett.*, 2001, 2, 122; (b) K. Seki, S. Takamizawa and W. Mori, *Chem. Lett.*, 2001, 4, 332.

[92] K. Seki and W. Mori, *J. Phys. Chem. B*, 2002, 106, 1380.

[93] W. Mori, T. Sato, T. Ohmura, C. N. Kato and T. Takei, *J. Solid State Chem.*, 2005, 178, 2555.

[94] W. Mori, S. Takamizawa, C. N. Kato, T. Ohmura and T. Sato, *Microporous Mesoporous Mater.*, 2004, 73, 31.

[95] A. Pichon, C. M. Fierro, M. Nieuwenhuyzen and S. L. James, *CrystEngComm*, 2007, 9, 449.

[96] (a) S. C. Manna, E. Zangrando, J. Ribas and N. R. Chaudhuri, *Inorg. Chim. Acta*, 2008, 361, 411; (b) P. S. Mukherjee, S. Konar, E. Zangrando, T. Mallah, J. Ribas and N. R. Chaudhuri, *Inorg. Chem.*,

2003, 42, 2695; (c) S. Konar, P. S. Mukherjee, M. G. B. Drew, J. Ribas and N. R. Chaudhuri, *Inorg. Chem.*, 2003, 42, 2545.

[97] Z. Fu, J. Yi, Y. Chen, S. Liao, N. Guo, J. Dai, G. Yang, Y. Lian and X. Wu, *Eur. J. Inorg. Chem.*, 2008, 628.

[98] L. Ma and W. Lin, *J. Am. Chem. Soc.*, 2008, 130, 13834.

[99] L. Ma, D. J. Mihalcik and W. Lin, *J. Am. Chem. Soc.*, 2009, 131, 4610

[100] H. J. Park and M. P. Suh, *Chem.–Eur. J.*, 2008, 14, 8812–8821.

[101] T. Yuen, D. Danilovic, K. Li and J. Li, *J. Appl. Phys.*, 2008, 103, 07B725.

[102] Z. Wang, K. K. Tanabe and S. M. Cohen, *Inorg. Chem.*, 2009, 48, 296.

[103] D. N. Dybtsev, H. Chun and K. Kim, *Angew. Chem. Int. Ed.*, 2004, 43, 5143.

[104] H. Chun, D. N. Dybtsev, H. Kim and K. Kim, *Chem.–Eur. J.*, 2005, 11, 3521.

[105] X. Song, X. Liu, M. Oh and M. S. Lah, *Cryst. Growth Des.*, 2010, 10, 3222.

[106] D. N. Dybtsev, M. P. Yutkin, E. V. Peresyphkina, A. V. Virovets, C. Serre, G. Férey and V. P. Fedin, *Inorg. Chem.*, 2007, 46, 6843.

[107] H. Wang, J. Getzschmann, I. Senkovska and S. Kaskel, *Microporous Mesoporous Mater.*, 2008, 116, 653

- [108] B. Chen, F. R. Fronczek, B. H. Courtney and F. Zapata, *Cryst. Growth Des.*, 2006, 6, 825.
- [109] B. Chen, S. Ma, F. Zapata, E. B. Lobkovsky and J. Yang, *Inorg. Chem.*, 2006, 45, 5718.
- [110] B. Chen, S. Ma, E. J. Hurtado, E. B. Lobkovsky, C. Liang, H. Zhu and S. Dai, *Inorg. Chem.*, 2007, 46, 8705.
- [111] B. Chen, S. Ma, E. J. Hurtado, E. B. Lobkovsky and H.-C. Zhou, *Inorg. Chem.*, 2007, 46, 8490.
- [112] B. Chen, S. Ma, F. Zapata, F. R. Fronczek, E. B. Lobkovsky and H.-C. Zhou, *Inorg. Chem.*, 2007, 46, 1233.
- [113] B. Chen, Y. Ji, M. Xue, F. R. Fronczek, E. J. Hurtado, J. U. Mondal, C. Liang and S. Dai, *Inorg. Chem.*, 2008, 47, 5543.
- [114] M. Xue, S. Ma, Z. Jin, R. M. Schaffino, G.-S. Zhu, E. B. Lobkovsky, S.-L. Qiu and B. Chen, *Inorg. Chem.*, 2008, 47, 6825
- [115] B. Chen, C. Liang, J. Yang, D. S. Contreras, Y. L. Clancy, E. B. Lobkovsky, O. M. Yaghi and S. Dai, *Angew. Chem., Int. Ed.*, 2006, 45, 1390.
- [116] R. Kitaura, F. Iwahori, R. Matsuda, S. Kitagawa, Y. Kubota, M. Takata and T. C. Kobayashi, *Inorg. Chem.*, 2004, 43, 6522.
- [117] D. Tanaka, S. Horike, S. Kitagawa, M. Ohba, M. Hasegawa, Y. Ozawa and K. Toriumi, *Chem. Commun.*, 2007, 3142.
- [118] B.-Q. Ma, K. L. Mulfort and J. T. Hupp, *Inorg. Chem.*, 2005, 44, 4912.

- [119] S. H. Cho, B. Ma, S. T. Nguyen, J. T. Huppand and T. E. Albrecht-Schmitt, *Chem. Commun.*, 2006, 2563.
- [120] See for example:(a) A. Pöppel, S. Kunz, D. Himsl and M. Hartmann, *J. Phys. Chem. C*, 2008, 112, 2678; (b) H.Wu, J. M. Simmons, Y. Liu, C. M. Brown, X.-S.Wang, S. Ma, V. K. Peterson, P. D. Southon, C. J. Kepert, H.-C. Zhou, T. Yildirim and W. Zhou, *Chem.–Eur. J.*, 2010, 16, 5205.
- [121] M. Kramer, U. Schwarz and S. Kaskel, *J. Mater. Chem.*, 2006, 16, 2245.
- [122] R. Gruenker, I. Senkovska, R. Biedermann, N. Klein, A. Klausch, I. A. Baburin, U. Müller and S. Kaskel, *Eur. J. Inorg. Chem.*, 2010, 3835.
- [123] B. Chen, M. Eddaoudi, T.M. Reineke, J.W. Kampf, M. O’Keeffe and O. M. Yaghi, *J. Am. Chem. Soc.*, 2000, 122, 11559.
- [124] F. A. Cotton, C. A. Murillo and R.A.Walton, *Multiple Bonds Between Metal Atoms*, 3rd ed., Springer Science and Business Media, Inc., New York, 2005.
- [125] T. M. Reineke, M. Eddaoudi, M. Fehr, D. Kelley and O. M. Yaghi, *J. Am. Chem. Soc.*, 1999, 121, 1651.
- [126] B. Chen, M. Eddaoudi, S. T. Hyde, M. O’Keeffe and O. M. Yaghi, *Science*, 2001, 291, 1021.
- [127] J. Kim, B. Chen, T. M. Reineke, H. Li, M. Eddaoudi, D. B. Moler, M. O’Keeffe and O. M. Yaghi, *J. Am. Chem. Soc.*, 2001, 123, 8239.

- [128] M. Eddaoudi, J. Kim, M. O’Keeffe and O. M. Yaghi, *J. Am. Chem. Soc.*, 2002, 124, 376.
- [129] H. Zhao, Z.-R. Qu, Q. Ye, X.-S. Wang, J. Zhang, R.-G. Xiong and X.-Z. You, *Inorg. Chem.*, 2004, 43, 1813.
- [130] (a) D. Sun, S. Ma, Y. Ke, D. J. Collins and H.-C. Zhou, *J. Am. Chem. Soc.*, 2006, 128, 3896; (b) S. Ma, D. Sun, M. Ambrogio, J. A. Fillinger, S. Parkin and H.-C. Zhou, *J. Am. Chem. Soc.*, 2007, 129, 1858.
- [131] S. Horike, S. Hasegawa, D. Tanaka, M. Higuchi and S. Kitagawa, *Chem. Commun.*, 2008, 4436.
- [132] S. E. Wenzel, M. Fischer, F. Hoffmann and M. Fröba, *Inorg. Chem.*, 2009, 48, 6559.
- [133] J. R. Li , R. J. Kuppler, H. C. Zhou, *Chem. Soc. Rev.* 2009,38 , 1477 .
- [134] A. U. Czaja , N. Trukhan , U. Muller , *Chem. Soc. Rev.* 2009 , 38 ,1284 .
- [135] L. Hamon , C. Serre , T. Devic , T. Loiseau , F. Millange , G. Ferey , G. De Weireld , *J. Am. Chem. Soc.* 2009 , 131 , 8775 .
- [136] K. A. Cychoz , A. G. Wong-Foy , A. J. Matzger , *J. Am. Chem. Soc.* 2008 , 130 , 6938 .
- [137] K. A. Cychoz , A. G. Wong-Foy , A. J. Matzger , *J. Am. Chem. Soc.* 2009 , 131 , 14538 .
- [138] R. W. Baker , *Ind. Eng. Chem. Res.* 2002 , 41 , 1393 .

- [139] E. E. McLeary , J. C. Jansen , F. Kapteijn , *Microporous Mesoporous Mater.* 2006 , 90 , 198 .
- [140] Rowsell, J. L. C.; Yaghi, O. M. *Metal-organic Frameworks: A New Class of Porous Materials.* *Microporous Mesoporous Mater.* 2004, 73, 3.
- [141] J. G. Won , J. S. Seo , J. H. Kim , H. S. Kim , Y. S. Kang , S. J. Kim , Y. M. Kim , J. G. Jegal , *Adv. Mater.* 2005 , 17 , 80 .
- [142] E. V. Perez , K. J. Balkus , J. P. Ferraris , I. H. Musselman , J. *Membr. Sci.* 2009 , 328 , 165 .
- [143] Y. Y. Liu , Z. F. Ng , E. A. Khan , H. K. Jeong , C. B. Ching , Z. P. Lai , *Microporous Mesoporous Mater.* 118 , 296 .
- [144] Y. Yoo , Z. P. Lai , H. K. Jeong , *Microporous Mesoporous Mater.* 2009 , 123 , 100 .
- [145] H. L. Guo , G. S. Zhu , I. J. Hewitt , S. L. Qiu , *J. Am. Chem. Soc.* 2009 , 131 , 1646 .
- [146] J. Lee , O. K. Farha , J. Roberts , K. A. Scheidt , S. T. Nguyen , J. T. Hupp , *Chem. Soc. Rev.* 2009 , 38 , 1450 .
- [147] L. Q. Ma , C. Abney , W. B. Lin , *Chem. Soc. Rev.* 2009 , 38 , 1248 .
- [148] S. Hermes , M. K. Schroter , R. Schmid , L. Khodeir , M. Muhler , A. Tissler , R. W. Fischer , R. A. Fischer , *Angew. Chem. Int. Ed.* 2005 , 44 , 6237 .

- [149] F. Schroeder, D. Esken, M. Cokoja, M. W. E. Van Den Berg, O. I. Lebedev, G. van Tendeloo, B. Walaszek, G. Buntkowsky, H. H. Limbach, B. Chaudret, R. A. Fischer, *J. Am. Chem. Soc.* 2008, 130, 6119 .
- [150] M. Muller , S. Hermes , K. Kaehler , M. W. E. Van Den Berg , M. Muhler , R. A. Fischer , *Chem. Mater.* 2008 , 20 , 4576 .
- [151] T. Ishida , M. Nagaoka , T. Akita , M. Haruta , *Chem-Eur. J.* 2008 , 14 , 8456 .
- [152] S. Proch , J. Herrmannsdorfer , R. Kempe , C. Kern , A. Jess , L. Seyfarth , J. Senker , *Chem. Eur. J.* 2008 , 14 , 8204 .
- [153] H. L. Jiang , B. Liu , T. Akita , M. Haruta , H. Sakurai , Q. Xu , *J. Am. Chem. Soc.* 2009 , 131 , 11302 .
- [154] Y. K. Park , S. B. Choi , H. J. Nam , D. Y. Jung , H. C. Ahn , K. Choi , H. Furukawa , J. Kim , *Chem. Commun.* 2010 , 46 , 3086 .
- [155] N. V. Maksimchuk , M. N. Timofeeva , M. S. Melgunov , A. N. Shmakov , Y. A. Chesalov , D. N. Dybtsev , V. P. Fedin , O. A. Kholdeeva , *J. Catal.* 2008 , 257 , 315 .
- [156] G. Kwak , M. Fujiki , *Macromolecules* 2004 , 37 , 2021 .
- [157] J. Juan-Alcaniz, E. V. Ramos-Fernandez, U. Lafont, J. Gascon, F. Kapteijn , *J. Catal.* 2010 , 269 , 229 .
- [158] P. Horcajada , C. Serre , M. Vallet-Regi , M. Sebban , F. Taulelle , G. Ferey , *Angew. Chem. Int. Ed.* 2006 , 45 , 5974 .

- [159] A. C. McKinlay , B. Xiao , D. S. Wragg , P. S. Wheatley , I. L. Megson , R. E. Morris , J. Am. Chem. Soc. 2008 , 130 , 10440 .
- [160] J. Y. An, S. J. Geib, N. L. Rosi, J. Am. Chem. Soc. 2009, 131, 8376.
- [161] M. D. Rowe , D. H. Thamm , S. L. Kraft , S. G. Boyes , Biomacromolecules 2009 , 10 , 983 .
- [162] K. M. L. Taylor-Pashow , J. Della Rocca , Z. G. Xie , S. Tran , W. B. Lin , J. Am. Chem. Soc. 2009 , 131 , 14261 .
- [163] P. Horcajada , C. Serre , G. Maurin , N. A. Ramsahye , F. Balas , M. Vallet-Regi , M. Sebban , F. Taulelle , G. Ferey , J. Am. Chem. Soc. 2008 , 130 , 6774 .
- [164] P. Horcajada, T. Chalati, C. Serre, B. Gillet, C. Sebrie, T. Baati, J. F. Eubank , D. Heurtaux , P. Clayette , C. Kreuz , J. S. Chang , Y. K. Hwang , V. Marsaud , P. N. Bories , L. Cynober , S. Gil , G. Ferey, P. Couvreur , R. Gref , Nat. Mater. 2010 , 9 , 172 .
- [165] M. Sadakiyo , T. Yamada , H. Kitagawa , J. Am. Chem. Soc. 2009 , 131 , 9906 .
- [166] S. Takaishi , M. Hosoda , T. Kajiwara , H. Miyasaka , M. Yamashita , Y. Nakanishi , Y. Kitagawa , K. Yamaguchi , A. Kobayashi , H. Kitagawa , Inorg. Chem. 2009 , 48 , 9048 .
- [167] F. Gandara, A. de Andres, B. Gomez-Lor, E. Gutierrez-Puebla, M. Iglesias, M. A. Monge, D. M. Proserpio, N. Snejko, Cryst. Growth. Des. 2008, 8, 378.

- [168] M. S. Wang, S. P. Guo, Y. Li, L. Z. Cai, J. P. Zou, G. Xu, W. W. Zhou, F. K. Zheng, G. C. Guo, *J. Am. Chem. Soc.* 2009, 131, 13572.
- [169] K. A. White , D. A. Chengelis , M. Zeller , S. J. Geib , J. Szakos, S. Petoud , N. L. Rosi , *Chem. Commun.* 2009 , 4506 .
- [170] L. J. Murray, M. Dincà, Jeffrey R. Long *Chem. Soc. Rev.*, 2009, 38, 1294–1314.
- [171] R. C. Lochan and M. Head-Gordon, *Phys. Chem. Chem. Phys.*, 2006, 8, 1357–1370.
- [172] T. Duř ren and R. Q. Snurr, *J. Phys. Chem. B*, 2004, 108, 15703–15708.
- [173] H. Frost, T. Duř ren and R. Q. Snurr, *J. Phys. Chem. B*, 2006, 110, 9565–9570.
- [174] H. Frost and R. Q. Snurr, *J. Phys. Chem. C*, 2007, 111, 18794–18803.
- [175] E. Klontzas, A. Mavrandonakis, G. E. Froudakis, Y. Carissan and W. Klopper, *J. Phys. Chem. C*, 2007, 111, 13635–13640.
- [176] E. Klontzas, A. Mavrandonakis, E. Tylianakis and G. E. Froudakis, *Nano Lett.*, 2008, 8, 1572–1576.
- [177] E. Klontzas, E. Tylianakis and G. E. Froudakis, *J. Phys. Chem. C*, 2008, 112, 9095–9098.

- [178] A. Mavrandonakis, E. Tylianakis, A. K. Stubos and G. E. Froudakis, *J. Phys. Chem. C*, 2008, 112, 7290–7294.
- [179] S. S. Han, W.-Q. Deng and W. A. Goddard III, *Angew. Chem., Int. Ed.*, 2007, 46, 6289–6292.
- [180] S. S. Han, H. Furukawa, O. M. Yaghi and I. W. A. Goddard, *J. Am. Chem. Soc.*, 2008, 130, 11580–11581.
- [181] S. S. Han and W. A. Goddard III, *J. Phys. Chem. C*, 2007, 111, 15185–15191.
- [182] S. S. Han and W. A. Goddard III, *J. Am. Chem. Soc.*, 2007, 129, 8422–8423.
- [183] J. L. Belof, A. C. Stern and B. Space, *J. Chem. Theory Comput.*, 2008, 4, 1332–1337.
- [184] S. S. Kaye, A. Dailly, O. M. Yaghi and J. R. Long, *J. Am. Chem. Soc.*, 2007, 129, 14176–14177.
- [185] R. C. Lochan, R. Z. Khaliullin and M. Head-Gordon, *Inorg. Chem.*, 2008, 47, 4032–4044.
- [186] M. Dinca, A. Dailly, Y. Liu, C. M. Brown, D. A. Neumann and J. R. Long, *J. Am. Chem. Soc.*, 2006, 128, 16876–16883.
- [187] Y. Y. Sun, Y.-H. Kim and S. B. Zhang, *J. Am. Chem. Soc.*, 2007, 129, 12606–12607.

- [188] W. Zhou and T. Yildirim, *J. Phys. Chem. C*, 2008, 112, 8132–8135.
- [189] S. K. Bhatia and A. L. Myers, *Langmuir*, 2006, 22, 1688–1700.
- [190] E. Garrone, B. Bonelli and C. Otero Area' n, *Chem. Phys. Lett.*, 2008, 456, 68–70.
- [191] M. Rzepka, P. Lamp and M. A. de la Casa-Lillo, *J. Phys. Chem. B*, 1998, 102, 10894–10898.
- [192] M. Dinca' , W. S. Han, Y. Liu, A. Dailly, C. M. Brown and J. R. Long, *Angew. Chem., Int. Ed.*, 2007, 45, 1419–1422.
- [193] M. Dinca' and J. R. Long, *J. Am. Chem. Soc.*, 2007, 129, 11172–11176.
- [194] K. S. Park, Z. Ni, A. P. Co' te' , J. Y. Choi, R. Huang, F. J. Uribe-Romo, H. K. Chae, M. O'Keeffe and O. M. Yaghi, *Proc. Natl. Acad. Sci. U. S. A.*, 2006, 103, 10186–10191.
- [195] H. Wu, W. Zhou and T. Yildirim, *J. Am. Chem. Soc.*, 2007, 129, 5314–5315.
- [196] W. Zhou, H. Wu, M. R. Hartman and T. Yildirim, *J. Phys. Chem. C*, 2007, 111, 16131–16137.
- [197] H. Park, J. F. Britten, U. Mueller, J. Y. Lee, J. Li and J. B. Parise, *Chem. Mater.*, 2007, 19, 1302–1308.
- [198] H. Park, G. Krigsfeld and J. B. Parise, *Cryst. Growth Des.*, 2007, 7, 736–740.

- [199] X.-L. Wang, C. Qin, E.-B. Wang and Z.-M. Su, *Chem.–Eur. J.*, 2006, 12, 2680–2691.
- [200] C. Yang, X. Wang and M. A. Omary, *J. Am. Chem. Soc.*, 2007, 129, 15454–15455.
- [201] Q.-G. Zhai, C.-Z. Lu, X.-Y. Wu and S. R. Batten, *Cryst. Growth Des.*, 2007, 7, 2332–2342.
- [202] H. J. Choi, M. Dinca[~] and J. R. Long, *J. Am. Chem. Soc.*, 2008, 130, 7848–7850.
- [203] G. J. Kubas, *Metal Dihydrogen and σ -Bond Complexes—Structure, Theory, and Reactivity*, Kluwer Academic, New York, Boston, Dordrecht, London, Moscow, 2001.
- [204] C. H. Wu, *J. Chem. Phys.*, 1979, 71, 783–787.
- [205] S. S. Kaye and J. R. Long, *Chem. Commun.*, 2007, 4486–4488.
- [206] M. Dinca[~] and J. R. Long, *Angew. Chem., Int. Ed.*, 2008, 47, 6766–6779.
- [207] C. Prestipino, L. Regli, J. G. Vitillo, F. Bonino, A. Damin, C. Lamberti, A. Zecchina, P. L. Solari, K. O. Kongshaug and S. Bordiga, *Chem. Mater.*, 2006, 18, 1337–1346.
- [208] S. S. Kaye and J. R. Long, *J. Am. Chem. Soc.*, 2008, 130, 806–807.
- [209] S. S. Kaye and J. R. Long, *J. Am. Chem. Soc.*, 2005, 127, 6506–6507.

- [210] J. L. Belof, A. C. Stern, M. Eddaoudi and B. Space, *J. Am. Chem. Soc.*, 2007, 129, 15202–15210.
- [211] H. Kabbour, T. F. Baumann, J. H. Satcher, A. Saulnier and C. C. Ahn, *Chem. Mater.*, 2006, 18, 6085–6087.
- [212] M. Dinca, A. Dailly, C. Tsay and J. R. Long, *Inorg. Chem.*, 2008, 47, 11–13.
- [213] G. A. Somorjai, *Surf. Sci.*, 1994, 299–300, 849–866.
- [214] K. Christmann, G. Ertl and T. Pignet, *Surf. Sci.*, 1976, 54, 365–392.
- [215] R. A. Olsen, G. J. Kroes and E. J. Baerends, *J. Chem. Phys.*, 1999, 111, 11155–11163.
- [216] A. T. Pasteur, S. J. Dixon-Warren, Q. Ge and D. A. King, *J. Chem. Phys.*, 1997, 106, 8896–8904.
- [217] A. T. Gee, B. E. Hayden, C. Mormiche and T. S. Nunney, *J. Chem. Phys.*, 2000, 112, 7660–7668.
- [218] S. Khoobiar, *J. Phys. Chem.*, 1964, 68, 411–412
- [219] L. Wang and R. T. Yang, *Energy Environ. Sci.*, 2008, 1, 268–279.
- [220] H. Cheng, L. Chen, A. C. Cooper, X. Sha and G. P. Pez, *Energy Environ. Sci.*, 2008, 1, 338–354.
- [221] N. L. Rosi, J. Eckert, M. Eddaoudi, D. T. Vodak, J. Kim, M. O’Keeffe and O. M. Yaghi, *Science*, 2003, 300, 1127–1129.

- [222] J. L. C. Rowsell, A. R. Millward, K. S. Park and O. M. Yaghi, *J. Am. Chem. Soc.*, 2004, 126, 5666–5667.
- [223] B. Panella, M. Hirscher, H. Pützer and U. Müller, *Adv. Funct. Mater.*, 2006, 16, 520–524.
- [224] L. Pan, M. B. Sander, X. Huang, J. Li, M. R. Smith, E. W. Bittner, B. C. Bockrath and J. K. Johnson, *J. Am. Chem. Soc.*, 2004, 126, 1308–1309.
- [225] A. G. Wong-Foy, A. J. Matzger and O. M. Yaghi, *J. Am. Chem. Soc.*, 2006, 128, 3494–3495.
- [226] B. Panella and M. Hirscher, *Adv. Mater.*, 2005, 17, 538–541.
- [227] M. Sabo, A. Henschel, H. Frode, E. Klemm and S. Kaskel, *J. Mater. Chem.*, 2007, 17, 3827–3832.
- [228] D. N. Dybtsev, H. Chun and K. Kim, *Angew. Chem., Int. Ed.*, 2004, 43, 5033–5036.
- [229] J. Y. Lee, D. H. Olson, L. Pan, T. J. Emge and J. Li, *Adv. Funct. Mater.*, 2007, 17, 1255–1262.
- [230] J. Liu, J. Y. Lee, L. Pan, R. T. Obermyer, S. Simizu, B. Zande, J. Li, S. G. Sankar and J. K. Johnson, *J. Phys. Chem. C*, 2008, 112, 2911–2917.
- [231] B. A. Younglove, *J. Phys. Chem. Ref. Data*, 1982, 11, 1.
- [232] A. W. C. van den Berg and C. Otero Area'n, *Chem. Commun.*, 2008, 668–681.

- [233] D. Zhao, D. Yuan and H.-C. Zhou, *Energy Environ. Sci.*, 2008, 1, 222–235.
- [234] P. K. Thallapally, K. A. Kirby, J. L. Atwood, *New J. Chem.* 2007, 31, 628 – 630.
- [235] T. Düren, L. Sarkisov, O.M. Yaghi, R. Q. Snurr, *Langmuir* 2004, 20, 2683 – 2689.
- [236] V. C. Menon, S. Komarneni, *J. Porous Mater.* 1998, 5, 43 – 58.
- [237] G. Birkett, D. D. Do, *Langmuir* 2006, 22, 7622 – 7630.
- [205] D. Lozano-Castello, J. Alcaniz-Monge, M. A. de La Casa-Lillo, D. Cazorla-Amoros, A. Linares-Solano, *Fuel* 2002, 81, 1777–1803.
- [238] A. Perrin, A. Celzard, J. F. Mareche, G. Furdin, *Carbon* 2004, 42, 1249 – 1256.
- [239] A. Perrin, A. Celzard, J. F. Mareche, G. Furdin, *Energy Fuels* 2003, 17, 1283 – 1291.
- [240] D. Lozano-Castello, D. Cazorla-Amoros, A. Linares-Solano, *Energy Fuels* 2002, 16, 1321 – 1328.
- [241] X.W. Liu, L. Zhou, J.W. Li, Y. Sun, W. Su, Y. P. Zhou, *Carbon* 2006, 44, 1386 – 1392.
- [242] J. AlcaTiz-Monge, M. A. De La Casa Lillo, D. Cazorla-AmorUs, A. Linares-Solano, *Carbon* 1997, 35, 291 – 297.
- [243] Y. Zhou, Y. Wang, H. Chen, L. Zhou, *Carbon* 2005, 43, 2007–2012.

- [244] a) W. Mori, F. Yoshida, H. Nakayama, S. Takamizawa, M. Kishita, *Chem. Lett.* 1997, 1219 – 1220; b) S. Kitagawa, M. Kondo, *Bull. Chem. Soc. Jpn.* 1998, 71, 1739 – 1753.
- [245] M. Kondo, T. Okubo, A. Asami, S. Noro, T. Yoshitomi, S. Kitagawa, T. Ishii, H. Matsuzaka, K. Seki, *Angew. Chem.* 1999, 111, 190 – 193; *Angew. Chem. Int. Ed.* 1999, 38, 140 – 143.
- [246] M. Eddaoudi, J. Kim, N. Rosi, D. Vodak, J. Wachter, M. O'Keefe, O. M. Yaghi, *Science* 2002, 295, 469 – 472.
- [247] P. Kowalczyk, H. Tanaka, K. Kaneko, A. P. Terzyk, D. D. Do, *Langmuir* 2005, 21, 5639 – 5646.
- [248] F. Rodriguez-Reinoso, C. Almansa, M. Molina-Sabio, *J. Phys. Chem. B* 2005, 109, 20227 – 20231.
- [249] S. Y. Wang, *Energy Fuels* 2007, 21, 953 – 956.
- [250] S. Y. Wang, C. L. Zhong, *Acta Chim. Sin. (Engl. Ed.)* 2006, 64, 2375 – 2378.
- [251] Q. Y. Yang, C. L. Zhong, *J. Phys. Chem. B* 2006, 110, 17776–17783.
- [252] P. Kowalczyk, L. Brualla, A. Zywockinski, S. K. Bhatia, *J. Phys. Chem. C* 2007, 111, 5250 – 5257.
- [253] (a) J. Johnson, *Chem. Eng. News* 2004, 82 (51, Dec 20), 36-42.
(b) Z.; Yong, V. Mata,; A. E. Rodrigues *Sep. Purif. Technol.* 2002, 26, 195-205.

[254] (a) Li, H.; Eddaoudi, M.; O'Keeffe, M.; Yaghi, O. M. *Nature* 1999, 402, 276-279. (b) Eddaoudi, M.; Kim, J.; Rosi, N.; Vodak, D.; Wachter, J.; O'Keeffe, M.; Yaghi, O. M. *Science* 2002, 295, 469-472. (c) Chae, H. K.; Siberio-Pe' rez, D. Y.; Kim, J.; Go, Y. B.; Eddaoudi, M.; Matzger, A. J.; O'Keeffe, M.; Yaghi, O. M. *Nature* 2004, 427, 523-527. (d) Ockwig, N. W.; Delgado-Friedrichs, O.; O'Keeffe, M.; Yaghi, O. M. *Acc. Chem. Res.* 2005, 38, 176-182. (e) Yaghi, O. M.; O'Keeffe, M.; Ockwig, N. W.; Chae, H. K.; Eddaoudi, M.; Kim, J. *Nature* 2003, 423, 705-714. (f) Kitagawa, S.; Kitaura, R.; Noro, S. *Angew. Chem., Int. Ed.* 2004, 43, 2334-2375. (g) Fletcher, A. J.; Thomas, K. M.; Rosseinsky, M. J. J. *Solid State Chem.* 2005, 8, 2491-2510. (h) Kepert, C. J.; Prior, T. J.; Rosseinsky, M. J. J. *Am. Chem. Soc.* 2000, 122, 5158-5168. (i) Co'te', A. P.; Shimizu, G. K. H. *Coord. Chem. ReV.* 2003, 245, 49-64. (j) Duren, T.; Sarkisov, L.; Yaghi, O. M.; Snurr, R. Q. *Langmuir* 2004, 20, 2683-2689. (k) Schlichte, K.; Kratzke, T.; Kaskel, S. *Microporous Mesoporous Mater.* 2004, 73, 81-88.

[255] Andrew R. Millward and O. M. Yaghi, . *J. Am. Chem. Soc.* 2005, 127, 17998-17999.

[256] (a) Li, H.; Eddaoudi, M.; Groy, T. L.; Yaghi, O. M. *J. Am. Chem. Soc.* 1998, 120, 8571-8572. (b) Chen, B. L.; Ockwig, N. W.; Millward, A. R.; Contreras, D. S.; Yaghi, O. M. *Angew. Chem., Int. Ed.* 2005, 44, 4745- 4749. (c) Chui, S. S. Y.; Lo, S. M. F.; Charmant, J. P. H.; Orpen, A. G.; Williams, I. D. *Science* 1999, 283, 1148-1150. (d) Rosi, N. L.; Kim, J.; Eddaoudi, M.; Chen, B.; O'Keeffe, M.; Yaghi, O. M. *J. Am. Chem. Soc.* 2005, 127, 1504-1518

- [257] Cavenati, S.; Grande, C. A.; Rodrigues, A. E. *J. Chem. Eng. Data* 2004, 49, 1095-1101.
- [258] Himeno, S.; Komatsu, T.; Fujita, S. *J. Chem. Eng. Data* 2005, 50, 369-376.
- [259] Satyapal, S.; Petrovic, J.; Read, C.; Thomas, G.; Ordaz, G.; *Catalysis Today* 120 (2007) 246-256].
- [260] www.iphe.net
- [261] Ruthven, 2000.
- [262] Ruthven, 1984.
- [263] Wang, Q. M.; Shen, D.; Bulow, M.; Lau, M. L.; Deng, S.; Fitch, F. R.; Lemcoff, N. O.; Semanscin, *Mesoporous Mater.* 55, (2002), 217–230.
- [264] W. Ouellette, M.H. Yu, C.J. O'Connor, D. Hagrman, J. Zubieta, *Angew. Chem.* 118, (2006), 3577–3580.
- [265] A. Macario, A. Katovic, G. Giordano, F. Iucolano, D. Caputo, *Micropor Mesopor Mat.* 81 (2005) 139–147.
- [266] N. Gargiulo, M. Imperatore, P. Aprea, D. Caputo, *Micropor Mesopor Mat.*, 145 (2011) 74–79.
- [267] Fèrey et al., *Scienze*, , 309, (2005), 2040.
- [268] Schlichte, K.; Kratzke, T.; Kaskel, S. *Microporous Mesoporous Mater.* 2004, 73, 81–88.
- [269] Chui, S. S.-Y.; Lo, S. M.-F.; Charmant, J. P. H.; Orpen, A. G.;

Williams, I. D. A, *Science* 1999, 283, 1148–1150.

[270] Mueller, U.; Schubert, M.; Teich, F.; Puetter, H.; Schierle-Arndt, K.; Pastre, J. J. *Mater. Chem.* 2006, 16, 626–636

[271] Sing, K. S. W.; Everett, D. H.; Haul, R. A. W.; Moscou, L.; Pierotti, R. A.; Rouquerol, J.; Siemieniewska, T. , *Pure Appl. Chem.* 1985, 57, 603–619.

[272] Gregg, S. J.; Sing, K. S. W., Academic Press: London, 1982.

[273] Chowdhury, P.; Bikkina, C.; Meister, D.; Dreisbach, F.; Gumma, S., *Microporous Mesoporous Mater.* 2009, 117, 406–413.

[274] Liang, Z.; Marshall, M.; Chaffee, A. L., *Energy Fuels* 2009, 23, 2785–2789.

[275] Breck, D. W. Wiley: New York, 1974.

[276] Jadhav, P. D.; Chatti, R. V.; Biniwale, R. B.; Labhsetwar, N. K.; Devotta, S.; Rayalu, S. S., *Energy Fuels* 2007, 21, 3555–3559.

[277] S. Lowell, J.E. Shields, M.A. Thomas, M. Thommes, *Characterization of Porous Solids and Powders: Surface Area, Pore size and Density*, first ed., Springer- Verlag, New York, 2004.

[278] Liang, Z.; Marshall, M.; Chaffee, A. L. , *Energy Fuels* 2009, 23, 2785–2789.

[279] Vitillo, J. G.; Regli, L.; Chavan, S.; Ricchiardi, G.; Spoto, G.; Dietzel, P. D. C.; Bordiga, S.; Zecchina, A. , *J. Am. Chem. Soc.* 2008, 130, 8386–8396.

- [280] Sips, R. On the Structure of a Catalyst Surface. *J. Chem. Phys.* 1948, 16, 490–495.
- [281] Do, D. D. *Adsorption Analysis: Equilibria and Kinetics*; Imperial College Press: London, 1998.
- [282] Siriwardane, R. V.; Shen, M. S.; Fisher, E. P.; Poston, J. A. , *Energy Fuels* 2001, 15, 279–284.
- [283] Martra, G.; Coluccia, S.; Davit, P.; Gianotti, E.; Marchese, L.; Tsuji, H.; Hattori, H., *Res. Chem. Intermed.* 1999, 25, 77–93.
- [284] Chue, K. T.; Kim, J. N.; Yoo, Y. J.; Cho, S. H.; Yang, R. T., *Ind. Eng. Chem. Res.* 1995, 34, 591–598.
- [285] W. Gao, D. Butler, D.L. Tomasko, *Langmuir* 20 (2004) 8083–8089
- [286] R.H. Perry, D.W. Green, *Perry's Chemical Engineers' Handbook*, seventh ed., McGraw-Hill, Kogakusha, Tokyo, 1997.
- [287] R.T. Yang, *Adsorbents: Fundamentals and Applications*, first ed., John Wiley & Sons, Hoboken, 2003.
- [288] D. Caputo, F. Iucolano, F. Pepe, C. Colella, *Micropor Mesopor Mat.* 105, 2007, 260–267.
- [289] B Panella, M. Hirscher, H. Putter, U. Müller, *Advanced Functional Materials* 16 , 2006, 520-524.
- [290] Latroche et al. *Angewandte Chemie, International Edition* (2006), 45, 8227-8231.

[291] R. E. Morris, P. S. Wheatley, *Angew. Chem. Int. Ed.* 47, 2008,4966-4981.